

TOBB UNIVERSITY OF ECONOMICS AND TECHNOLOGY
INSTITUTE OF NATURAL AND APPLIED SCIENCES

**MULTIMORPHOLOGICAL ZINC OXIDE: SYNTHESIS AND
INVESTIGATION OF SOLAR DRIVEN HYDROGEN GENERATION AND
OPTOELECTRICAL PROPERTIES**

PhD DISSERTATION

Nazrin ABDULLAYEVA

Department of Micro and Nanotechnology

Advisor: Prof. Nurdan DEMİRCİ SANKIR

MARCH 2022

STATEMENT OF DISSERTATION

I declare that all the information in the thesis is presented in the frame of ethical behavior and academic rules, that the cited sources are cited completely, that the references are fully specified and that this thesis is prepared in accordance with TOBB ETU Institute of Natural and Applied Sciences thesis writing rules.

Nazrin ABDULLAYEVA

ABSTRACT

PhD Dissertation

Multimorphological Zinc Oxide: Synthesis and Investigation of Solar Driven
Hydrogen Generation and Optoelectrical Properties

Nazrin ABDULLAYEVA

TOBB University of Economics and Technology
Institute of Natural and Applied Sciences
Micro and Nanotechnology Science Program

Advisor: Prof. Nurdan DEMIRCI SANKIR

Date: March 2022

This dissertation is based on a highly distinctive, diosyncratic, and multiversant metal oxide semiconductor, zinc oxide (ZnO). More specifically, the work comprises the utilization of ZnO as both a highly efficient photoanode material and a photoluminescent thin film that serves both energy-based and optoelectronic applications. The emphasis within the scope of the dissertation is made on the morphological diversity of ZnO and the ways to utilize this as an advantage in photoelectrochemical and light-emitting appliances. Essentially, the dissertation consists of three main parts details of which are elaborated as follows;

(i) In the first part, ZnO thin films are grown via hydrothermal routes in three diverse morphologies on flexible stainless steel substrates. Here, the aim was to examine the potential of implementation of ZnO-based photoelectrodes into strained, curvature systems by analyzing their photon-to-current conversion efficiencies under flexed conditions. The obtained performances have been correlated with detailed material characterizations offering an integrated vision of the system's operability.

(ii) In this part, ZnO thin films were targeted to be grown on specific patterns without engaging costly and time-consuming lithographic techniques. By developing a smart approach, selective growth of ZnO has been attained by taking advantage of its seeding-layer selective nature. To put it differently, knowing that ZnO nanostructures have nucleation and growth pathways that vary strongly depending on the seeding layer, a dual ZnO/Ti stack film has been introduced onto the system. At this stage, Ti was the growth prohibiting agent, while ZnO seeding layer beneath played the role of growth provider. Through the careful utilization of a nanosecond fiber laser system, Ti layers have been successfully removed from the predetermined regions, consequently providing the selective allocation of ZnO nanostructures. By altering the ablation power, a concurrent growth of two different structures has been provided within the same hydrothermal solution and on the same substrate. This nanostructure duality has severely boosted the photoluminescence (PL) ability of ZnO films outscoring the light-emitting performances of individual nanostructures.

(iii) In the final part of the dissertation, dual ZnO nanostructured films have been deposited with 0D and 3D inorganic halide perovskite (IHP) layers to maximize the PL performances and prolong the minority carrier lifetimes for future light-emitting device applications. With the incorporation of IHP layers a substantial improvement in emission, especially within the visible range, has been observed. Moreover, the increased carrier lifetimes have shown the promising characteristics of patterned and IHP sensitized multi-morphological ZnO films.

Keywords: Zinc oxide, Photoelectrochemical water splitting, Photon-to-current conversion efficiency, Multi-morphological ZnO, Hierarchical thin films, Chemical bath deposition, Nanosecond fiber laser, Patterning, Selective thin film growth, Photoluminescence.

ÖZET

Doktora Tezi

Çoklu Morfolojili Çinko Oksit: Sentez, Güneş Enerjili Hidrojen Üretimi ve Optoelektrik Özelliklerin İncelenmesi

Nazrin ABDULLAYEVA

TOBB Ekonomi ve Teknoloji Üniversitesi
Fen Bilimleri Enstitüsü
Mikro ve Nanoteknoloji Anabilim Dalı

Danışman: Prof. Dr. Nurdan DEMIRCI SANKIR

Tarih: Mart 2022

Bu tez, kendine özgü özelliklere sahip, çok yönlü bir metal oksit yarı iletken olan çinko oksit'in (ZnO) fotoelektrokimyasal ve optoelektronik alanlara uygulanmasına dayanmaktadır. Başka bir deyişle, çalışma, ZnO'nun hem yüksek verimli bir fotoanot materyali olarak enerji tabanlı uygulamalarda yer almasını hem de optoelektronik uygulamalara hizmet eden yüksek ışımaya performansına sahip bir ince film olarak kullanımını içermektedir. Tez kapsamında ZnO'nun morfolojik çeşitliliği ve bu çeşitliliğin farklı uygulamalarda kullanımının avantajları üzerinde durulmuştur. Temel olarak tez, detayları aşağıda belirtilen üç ana bölümden oluşmaktadır;

(i) İlk bölümde, ZnO ince filmler, esnek paslanmaz çelik altaşlar üzerinde üç farklı morfolojide hidrotermal yolla büyütülmüştür. Burada amaç, esnek koşullar altında fotonakım dönüşüm verimliliklerini analiz ederek, ZnO bazlı fotoelektrotların gergin, eğrilik sistemlerine uygulanma potansiyelini incelemektir. Elde edilen performanslar, sistemin

çalıřabilirliđine iliřkin entegre bir vizyon sunan ayrıntılı malzeme karakterizasyonları ile iliřkilendirilmiřtir.

(ii) Bu bölümde, ZnO ince filmlerin, maliyetli ve zaman alıcı litografik teknikler kullanılmadan belirli desenler üzerinde büyütülmesi hedeflenmiřtir. Akıllı bir yaklařım geliřtirerek, tohum katmanı seçici yapısından yararlanarak ZnO'nun seçici büyümesi sađlanmıřtır. Bařka bir deyiřle, ZnO nanoyapılarının tohumlama katmanına bađlı olarak büyük ölçüde deđiřen çekirdeklenme ve büyüme yollarına sahip olduđunu bilerek, sisteme bir çift ZnO/Ti yığın filmi eklenmiřtir. Bu ařamada Ti büyümeyi engelleyen ajan iken, alttaki ZnO tohum tabakası büyüme sađlayıcı rolünü oynadı. Nanosaniye fiber lazer sisteminin dikkatli kullanımı sayesinde, Ti katmanları önceden belirlenmiř bölgelerden başarıyla çıkarıldı ve sonuç olarak ZnO nanoyapılarının seçici tahsisi sađlanmıřtır. Ablasyon gücü deđiřtirilerek, aynı hidrotermal solüsyon içerisinde ve aynı substrat üzerinde iki farklı yapının aynı anda büyümesi sađlanmıřtır. Bu nanoyapı ikiliđi, ZnO filmlerinin fotoluminesans (PL) yeteneđini, bireysel nanoyapıların ıřık yayma performanslarını geride bırakarak ciddi řekilde artırdı.

(iii) Tezin son bölümünde, gelecekteki ıřık yayan cihaz uygulamaları için PL performanslarını en üst düzeye çıkarmak ve azınlık taşıyıcı ömürlerini uzatmak için 0D ve 3D inorganik halojenür perovskit (IHP) katmanları ile çift ZnO nanoyapılı filmler biriktirildi. IHP katmanlarının dahil edilmesiyle, özellikle görünür aralıkta emisyonda önemli bir geliřme gözlemlendi. Ayrıca, artan taşıyıcı ömürleri, desenli ve IHP'ye duyarlı hale getirilmiř çok morfolojik ZnO filmlerinin umut verici özelliklerini göstermiřtir.

Anahtar Kelimeler: Çinko oksit, Fotoelektrokimyasal su ayırma, Foton-akım dönüşüm verimliliđi, Çoklu morfolojik ZnO, Hiyerarřik ince filmler, Kimyasal banyo biriktirme, Nanosaniye fiber lazer, Desenleme, Seçici ince film büyümesi, Fotoluminesans.

ACKNOWLEDGMENT

I would like to begin by expressing my sincere gratitude to my advisors Prof. Nurdan Demirci Sankir and Prof. Mehmet Sankir for guiding me in this incredible journey of knowledge and enlightenment. It was the greatest pleasure for me to be a part of such a progressive, forward-thinking, broad-visioned research group that always worked and invested for the sake of planet Earth. I am grateful to them for teaching me the essence of scientific work and leading me in this way of finding my true potential. Thanks to them both for the patience, understanding, and humanity that they displayed through this period of time.

I am also indebted to the distinguished members of my advisory committee, Prof. Hamza Kurt and Prof. Mehmet Parlak for their attention, guidance, time, and suggestions that they have put forward to my knowledge, education, and dissertation.

I owe a huge thanks to the dearest and most hard-working post-doctoral researcher of our research group, Dr. Cigdem Tuc Altaf. Her arrival to our research group has been incredibly valuable and played a very substantial role in my life. Thanks to her, I have been able to motivate myself to work on the ups and downs of this bumpy journey. Another sincere appreciation goes to Alihan Kumtepe, one of the most hardworking MSc. students I have ever met. I have always appreciated his devotedness to work and incredible partnership at team works. Similarly, thanks to my valuable lab-mates, Ozlem Coskun, MSc. Tuluhan Olcayto Colak and MSc. Emine Karagoz for their constant support.

I do not know how to put into words the endless gratefulness that I feel to my dearest husband, my partner-in-life, Ibrahim Can Karaahmetoglu. Owing to his love, support, patience, and understanding this enjoyable yet challenging journey has turned out to be much more pleasant.

My other thankfulness is to my precious family members, my mother Sevinc, my father Zaur, and, my sister Gunel. I am grateful to them for raising me, supporting me, and

making me who I am. They and their aspect of life have always stimulated me and have been the best role model I could have ever asked for. Biggest thanks to my parents-in-law Ayse and Ahmet, for being as understanding as my own parents through this journey.

I would like to dedicate this dissertation to my darling son Ahmet Eren, who joined us during this period and who brought more joy and fun and put a different meaning into my life.



CONTENTS

	<u>Page</u>
ACKNOWLEDGMENT	vii
CONTENTS.....	ix
LIST OF FIGURES	xii
LIST OF TABLES	xviii
ABBREVIATIONS.....	xix
LIST OF SYMBOLS	xxii
LIST OF EQUATIONS	xxiii
CHAPTER 1	1
1. INTRODUCTION.....	1
1.1. Aim of the Study.....	1
1.2. Literature Review.....	1
1.3. Semiconductors.....	3
1.4. Zinc Oxide	4
1.5. Crystal Structure of ZnO.....	4
1.6. Electronic Properties.....	4
1.7. Synthesis Methods of ZnO.....	5
CHAPTER 2	8
2. INVESTIGATION OF STRAIN EFFECTS ON PEC PERFORMANCES OF FLEXIBLE ZnO ELECTRODES	8
2.1. Introduction.....	8
2.2. Experimental Methods	9
2.2.1 Preparation of ZnO electrodes	9
2.2.2 Characterization of ZnO electrodes	10
2.2.3 Straining tests.....	11
2.3 Results & Discussion.....	12
2.3.1 1D- 3D ZnO flat electrodes and their characterizations.....	12
2.3.2 Application of straining test on ZnO photoelectrodes and their detailed characterizations	21
2.4 Conclusions	29
CHAPTER 3	31

3. CONTROLLING PHOTOLUMINESCENCE OF MULTI MORPHOLOGICALLY GROWN ZnO NANOSTRUCTURES PATTERNED VIA NANOSECOND LASER ABLATION	31
3.1 Introduction	31
3.1.1 Photoluminescence phenomenon	32
3.1.2 Photoluminescence properties of Zinc Oxide.....	33
3.1.3 Nanoscaled patterning techniques	34
3.1.4 Nanosecond fiber laser ablation as a successful tool for patterning.....	35
3.1.5 Role of ZnO in optoelectronic applications.....	36
3.2. Experimental Methods.....	36
3.2.1 Preparation of substrates.....	36
3.2.2 ns fiber laser ablation process and parameter determination.....	37
3.2.3 Characterization techniques.....	38
3.3 Results & Discussion.....	40
3.3.1 Growth of two different ZnO nanostructures within the identical CBD solution	40
3.3.2 Laser processing of ZnO thin films	51
3.3.2.1 Examination of “In-Focus” laser ablated substrates for selective ZnO growth via optical microscopy	51
3.3.2.2. Examination of “Out-of-Focus” laser ablated substrates for selective ZnO growth via optical microscopy	53
3.3.2.3 Imaging of ZnOs grown on substrates patterned under different DF.....	53
3.3.2.4 Examination of the effect of fluence energy on ablation performance	55
3.4 Conclusions	62
CHAPTER 4	63
4. ENHANCEMENT OF PHOTOLUMINESCENCE PERFORMANCE OF MULTIMORPHOLOGICAL ZnO VIA METAL HALIDE PEROVSKITE SENSITIZATION	63
4. 1. Introduction	63
4.1.1 Metal halide perovskites.....	64
4.1.2 Photoluminescence properties of metal halide perovskites	65
4.1.3 Cs ₄ PbBr ₆ structure of perovskites and their superior luminescent properties	66
4.2 Experimental Methods.....	67
4.2.1 Preparation of Substrates	67
4.2.3 Metal halide perovskite sensitization of patterned ZnO thin films	67
4.3 Results and Discussion	68

4.3.1 Fluorescence microscopy imaging of pristine and patterned ZnO thin films	68
4.3.2 Effect of Cs ₄ PbBr ₆ on PL performances of patterned multi-morphological ZnO thin films	70
4.4 Conclusions	78
REFERENCES	79
RESUME	Error! Bookmark not defined.



LIST OF FIGURES

	<u>Page</u>
Figure 1.1: Yearly statistics of numbers of publications of ZnO.....	3
Figure 1.2: Hexagonal wurtzite crystal structure of ZnO	4
Figure 2.1: Photoelectrochemical water splitting system set-up.....	11
Figure 2.2: Mechanical deformation (straining) applied on ZnO thin films.....	12
Figure 2.3: SEM Images of ZnO nanostructures of (a) nanoflower, (b) nanosheet and (c) nanowire.....	14
Figure 2.4: Atomic percentages obtained from EDAX analysis of ZnO thin films.....	14
Figure 2.5: XRD crystalline peaks of ZnO nanostructures.....	15
Figure 2.6: XPS analysis revealing the (a) overall elemental composition of ZnO thin films and (b-d) Individual O1s peak deconvolutions for defect identification.....	18
Figure 2.7: (a) Total photoluminescence spectra and and PL peak deconvolutions of (b) NF, (c) NS, and (d) NW morphologies, respectively.....	19
Figure 2.8: Raman spectra for 1D - 3D ZnO nanostructures with identified peaks and defect examinations.....	20
Figure 2.9: Photoelectrochemical characterizations of ZnO thin films in (a) illuminated and (b) dark conditions; (c) Stability analysis at 0 V _{bias} under consecutive light ON/OFF cycles and (d) responsivities evaluated from the obtained stability values.....	21
Figure 2.10: Optical characterizations of ZnO nanostructured thin films; (a) NF, (b) NS and (c) NW via UV/Vis.....	24
Figure 2.11: Photoelectrochemical characterizations of strained ZnO thin films in (a) illuminated and (b) dark conditions; (c) Stability analysis at 0 V _{bias} under consecutive LIGHT ON/OFF cycles and (d) responsivities evaluated from the obtained stability values.....	25

Figure 2.12: %IPCE data obtained for (a) flat and (b) strained ZnO thin films and individual comparison of flat and strained (c) NF, (d) NS and (e) NW performances... ..27

Figure 2.13: Mott-Schottky plots for (a) NF, (b) NS and (c) NW structures with corresponding evaluated V_{fb} and N_d data. EIS measurements revealing Nyquist plots of (d) NF, (e) NS and (f) NW.....28

Figure 2.14: Current density performances of intact, 10 and 50-times strained thin films obtained under potential sweep for (a) NF, (b) NS and (c) NW, respectively.....29

Figure 3.1: Consecutive steps of (a) ZnO deposition, (b) rapid high-temperature annealing and (c) Ti deposition for substrate preparation.....39

Figure 3.2: Laser ablation steps of Ti/ZnO coated ITO glass substrates under (a) low (3.72 J.cm^{-2}) and (b) high (28.43 J.cm^{-2}) fluence energies with EDAX data collected from laser spots giving a hint about penetration depths of scribing energy followed by exact same CBD steps proceeding each ablation process showing the growth of (a) nanorods (NRs) for and (b) nanoflakes (NFIs).....42

Figure 3.3: Birds eye and zoomed SEM images of (a) unidirectionally oriented ZnO nanorods, demonstrating a uniform film distribution over the substrate surface; (b) nanoflakes, demonstrating a scanty oriented distribution of film on the substrate.....43

Figure 3.4: XRD responses of wurtzite (a) NR and (b) NFI with insets representing rod-like and hexagonal flake-like structures; XAS responses with their detailed (c) XAFS, (d) XANES and (e) EXAFS elaborations.....45

Figure 3.5: (a) Optical absorption data of NFI and NRs together with (b) Tauc plots evaluated by using transmittance data with derivated Urbach energy evaluation graph. (c) PL spectra of NR and NFI with a detailed investigation of NBE and DBE regions.....47

Figure 3.6: Gaussian deconvolutions of the individual (a) NR and (b) NFI luminescence spectra. (c) Schematic representation of defect distribution within both nanostructures. TrPL responses obtained from DBE emissions of (d) NR and (e)-(f) NFI.....49

Figure 3.7: Numerical simulation of the distribution of absorbed light within ZnO (a) NR and (b) NFI structures. Comparison between experimental and numerical absorbance responses of (c) NR and (d) NFI-based thin films. TPS data of (e) NR and (f) NFI formations obtained under UHV by consecutively turning UV light on and off.....52

Figure 3.8: (a) Consecutive preparation steps of photoelectrodes. (b) Laser ablation of ZnO/Ti deposited substrates under 3.72 J.cm^{-2} fluence energy with three different predetermined patterns. (c) Schematic representation of “in-focus” laser ablation with corresponding DF distance.....	54
Figure 3.9: (a) “Out-of-focus” ablation conditions with DF adjusted to 18.5 cm. (b) Optical microscopy (OM) images of ablated substrates in “out-of-focus” DF distance showing significant changes in spot distances and spot appearances.....	55
Figure 3.10: NR growth on “in-focus” patterned substrates generating distinct film homogeneities detected via OM analysis.....	56
Figure 3.11: OM images of NR grown substrates under “out-of-focus” conditions patterned with (a) 0.1 (b) 0.2 and (c) 0.4 mm alley distances.....	57
Figure 3.12: OM images of $0.1 \times 0.1 \text{ cm}^2$ laser patterned substrates with their corresponding CBD grown SEM images under (a) 25W, 5500 mm/s, 70 kHz and (b) 7W, 4500 mm/s, 100 kHz application. OM images of $0.5 \times 0.5 \text{ cm}^2$ laser patterned substrates with their corresponding CBD grown SEM images under (c) 25W, 5500 mm/s, 70 kHz and (d) 7W, 4500 mm/s, 100 kHz application. Numerical simulations representing the temperature distribution profiles from cross-section under (e) 3.7 and (f) 28.4 J.cm^{-2} fluence energies.....	59
Figure 3.13: Photoluminescence performances of intact (i.e unpatterned), $0.1 \times 0.1 \text{ cm}^2$ and $0.5 \times 0.5 \text{ cm}^2$ patterned (a) NR and (b) NFI films. Optical absorption data of patterned and unpatterned (c) NR and (d) NFI structures.....	63
Figure 4.1: Image of perovskite deposited patterned ZnO thin films under different CsBr concentrations and number of spin cycles.....	70
Figure 4.2: (a) SEM image obtained from the large impurity formed on NFI grown thin film surrounded with tiny nanoflakes scattered around. (b) FM image of the impurity containing Zn, Mg, Si, and O atoms emitting the blue light under UV excitation thus enabling the observation of (c) tinier NFI species. (d) SEM image of ZnO NRs with a randomly outgrown single rod lying on the top of the homogeneous film. (e) FM image obtained from approximately same region showing a strong luminescence from the single rod itself in addition to strong blue emission coming from the background of densely packed NR films. (f) FM image obtained from patterned NRs showing a strong blue emission from the corners of square patterns where rod formations are grown and darker emissions from the centers which a comparably bolder.....	71

- Figure 4.3:** FM images of samples patterned under (a) 3.72 and (b) 28.43 J.cm⁻² fluence energies followed by hydrothermal growth of nanostructures obtained under 365 nm source irradiation. Fluorescence emission of samples deposited with (c) 1:1 perovskite layers with the corresponding representation of (d) emission intensity distribution along the punctuated region. (e) SEM images of the same sample set with (f) magnified image obtained from the edges of the pattern.....73
- Figure 4.4:** Fluorescence emission of samples deposited with (a) 1:5 perovskite layers with the corresponding representation of (b) emission intensity distribution along the punctuated region. (c) SEM images of the same sample set with (d) magnified image obtained from the edges of the pattern.....75
- Figure 4.5:** XRD responses of (a) 1:1 and (b) 1:5 PbBr₂:CsBr ratio deposited ZnO samples. (c) Optical absorption data of perovskite-deposited patterned ZnO thin films. (d) Photoluminescence spectra of perovskite-deposited patterned ZnO thin films. (e) TrPL outcomes individually comparing carrier lifetimes at (e) ZnO-originated and (f) perovskite-originated emissions.....77
- Figure 4.6:** Utilization of XRD data for the calculation of pristine and perovskite deposited ZnO's crystal sizes.....78
- Figure 4.7:** (a) SEM image of laser patterned and CBD grown samples containing the abbreviated name of the university. (b) Fluorescence emission image captured from patterned, CBD grown and perovskite-layer deposited sample containing the university logo. OM image of the same sample obtained under (c) yellow and (d) red filters.....79



LIST OF TABLES

	<u>Page</u>
Table 1.1: Different solution-based ZnO nanostructure synthesis techniques with various reaction parameters	7
Table 2.1: Ratios of deconvoluted oxygen peak intensities	15
Table 2.2: Ratios of deconvoluted oxygen peak intensities	18
Table 2.3: Morphological comparison of strained ZnO thin film samples from SEM images.....	22
Table 2.4: Fitted equivalent circuit models and corresponding values of circuit elements for NF, NS and NW structured ZnO thin films images	27
Table 2.5: Summary of photocurrent densities of ZnO electrodes at 0 V _{bias} (vs. Ag/AgCl) after consecutive straining cycles.....	29
Table 3.1: Deep level defects in ZnO nanostructures causing different color emissions.	34
Table 3.2: Default parameters of nanosecond fiber laser ablation system.....	39
Table 3.3: Necessary equations for calculation of NS laser parameters	39
Table 3.4: TrPL decay periods at corresponding defect associated emissions	48
Table 3.5: Parameters used for COMSOL Multiphysics simulation calculations with their significances and units	59

ABBREVIATIONS

0D	Zero Dimensional
1D	One Dimension
2D	Two Dimensional
3D	Three Dimensional
ALD	Atomic Layer Deposition
Bi	Bismuth
CaTiO ₃	Calcium Titanate
CBD	Chemical Bath Deposition
CdS	Cadmium Sulfide
CPE	Constant Phase Element
Cs	Cesium
CVD	Chemical Vapor Deposition
DEG	Diethylene Glycol
DF	Distance-To-Focus
DMF	Dimethylformamide
EDAX	Energy Dispersive X-Ray
EG	Ethylene Glycol
E _g	Band Gap
E _u	Urbach Energy
EIS	Electrochemical Impedance Spectroscopy
FDTD	Finite-Difference Time-Domain
FM	Fluorescence Microscopy
H ₂	Hydrogen

HMTA	Hexamethylenetetramine
IHP	Inorganic Halide Perovskites
ITO	Tin Doped Indium Oxide
ITO/ZnO	Zno Deposited On ITO Glass
LED	Light Emitting Diode
MS	Mott-Schottky
NBE	Near Band Edge
NF	Nanoflower
NFl	Nanoflake
NIR	Near-Infrared
NR	Nanorod
NS	Nanosheet
ns	Nanosecond
NW	Nanowire
O ₂	Oxygen
O _i	Oxygen Interstitials
OM	Optical Microscopy
Pb	Lead
PEC	Photoelectrochemical
PEI	Polyethyleneimine
PL	Photoluminescence
PLQY	Photoluminescence Quantum Yield
Pt	Platinum
PVD	Physical Vapor Deposition
Rb	Rubidium
RTA	Rapid Thermal Annealing
SEM	Scanning Electron Microscopy
Si	Silicon

SILAR	Successive Ionic Layer Adsorption And Reaction
TiO ₂	Titanium Dioxide
TPS	Transient Photocurrent Spectroscopy
UHV	Ultra-High Vacuum
V _{fb}	Flat Band Potential
V _o ⁺	Mono-Charged Oxygen Gaps
V _o ⁺⁺	Double-Charged Oxygen Gaps
V _{Zn}	Zinc Vacancies
V _{Zn}	Zinc Vacancies
W	Warburg Element
XAFS	X-Ray Absorption Fine Structure Spectroscopy
XANES	X-Ray Absorption Near Edge Structure
XAS	X-Ray Absorption Spectroscopy
XPS	X-Ray Photoelectron Spectroscopy
XRD	X-Ray Diffraction
Zn _i	Zinc Interstitials
ZnO	Zinc Oxide
Zn _o	Zinc Antisites

LIST OF SYMBOLS

The symbols used in this study are presented below along with their explanations.

Symbols	Explanation
R	Responsivity
J_{ill}	Current Density Under Illuminated Conditions
J_{dark}	Current Density Under Dark Conditions
P_{light}	Power of Light Source
I_{ph}	Photocurrent Density
λ	Wavelength of The Incoming Monochromatic Irradiation
P	Power Density of The Light
k	Thermal Conductivity
ρ	Material Density
T_m	Melting Temperature
c_p	Heat Capacity at Constant P
L_m and L_v	Latent Heat of Fusion and Vaporisation
Q	Laser Pulse Energy Source
φ_0	Peak Fluence
$R(\lambda)$	Film Reflectivity
τ_p	Full Width Half Maximum of Pulse Duration
r	Radial Coordinate
ω_0	$1/e^2$ of Spot Radius
$a(\lambda)$	Material Absorption Coefficient
z	Depth Component
α	Absorption Coefficient



LIST OF EQUATIONS

	<u>Page</u>
Equation 2.1: Thin Film Responsivity Calculation.....	22
Equation 2.2: Incident Photon-to-Current Conversion Efficiency Calculation.....	25
Equation 3.1: Pulse Energy.....	41
Equation 3.2: Fluence Energy.....	41
Equation 3.3: Peak Power.....	41
Equation 3.4: Power Density.....	41
Equation 3.5: Urbach Tail Calculation.....	46
Equation 3.6: Heat Distribution over Consecutive Thin Film Layers-1.....	60
Equation 3.7: Heat Distribution over Consecutive Thin Film Layers-2.....	60
Equation 3.8: Heat Distribution over Consecutive Thin Film Layers-3.....	60

CHAPTER 1

1. INTRODUCTION

With a memorable speech “There’s Plenty of Room at the Bottom” given by Richard Feynman in 1959, nanotechnology has been expeditiously introduced into our lives [1]. The inspiration of this catchy title resulted in a severe increase in the number of discoveries and investigations conducted in this field. Nowadays, these investigations still proceed at full throttle resulting in significant developments in various areas of interest such as energy, environment, health, technology, etc. Energy and the environment are the two interrelated concerns of the contemporary world since the fossil fuels constituting a large percentage of the total energy consumption are presenting a severe threat and damage to the environment. The nanotechnological researches conducted in the last few decades mainly focus on the carbon footprint reduction challenge and cultivation of renewable and harmless sources of alternative energy.

1.1. Aim of the Study

This study aims to use morphological diversity and versatile usability of ZnO to promote the technology and progress of semiconductor-originated energy-based and optoelectronic applications. Therefore, within the scope of this study, various characteristic features of ZnO, such as growth environment selectivity, nanostructure versatility, easy producibility, are going to be focalized and approached from different aspects.

1.2. Literature Review

Sun being the largest boundless natural energy source emits light into the atmosphere in a wide wavelength range. This variety of wavelengths is commonly called the electromagnetic spectrum and radiates beam that supplies both heat and energy to earth [2]. Nanotechnological advancements lead to the development of several crucial devices such as photovoltaics, photoelectrochemical water splitting systems and so on

that extract the energy from the incoming photons and convert them into electricity [3]. The common ground of these solar energy-based systems relies on specific types of materials known as semiconductors, which efficiently capture and convert the incoming energy into electrons generating current and providing the device's operability. SiO_2 , the most abundant metal oxide spread aboveground, gave rise to the development of the revolutionary semiconductor-based silicon (Si) solar cells that turned into one of the primary potential opponents to the fossil fuel industry. A large amount of time and effort has been spent on the perfection of these systems and the fields of implementations have been increased and varied from day to day. Despite the impressive efficiency of 33.7% that has been obtained from a single junction Si solar cell, some basic limitations such as costly production, small band gap that does not capture a large amount of spectrum, the hot electron and hole generation that results in efficiency decay, etc. hindered the further improvement in device performances [4]. In 1972, Honda and Fujishima brought in a brand new approach to the incorporation of semiconductors into solar energy systems [5]. It has been proposed that n-type semiconductor materials such as titanium dioxide (TiO_2), zinc oxide (ZnO), cadmium sulfide (CdS) result in the decomposition of water into hydrogen (H_2) and oxygen (O_2) under the effect of irradiation in an aqueous electrolyte environment known as photoelectrochemical (PEC) water splitting systems. This discovery strengthened the position of solar energy as it revealed that the sun is not only the source of energy itself but can also provide the generation of another type of energy carrier, H_2 . ZnO is one of the most frequently encountered semiconductor material representatives used in both new generation thin-film solar cells and PEC systems [6]. Several attractive features of ZnO such as its cost-effectiveness, the abundance of both zinc and oxygen on earth, stability and non-toxicity resulted in an irrepressible increase in the number of studies and investigations performed on this metal oxide material (Figure 1.1).

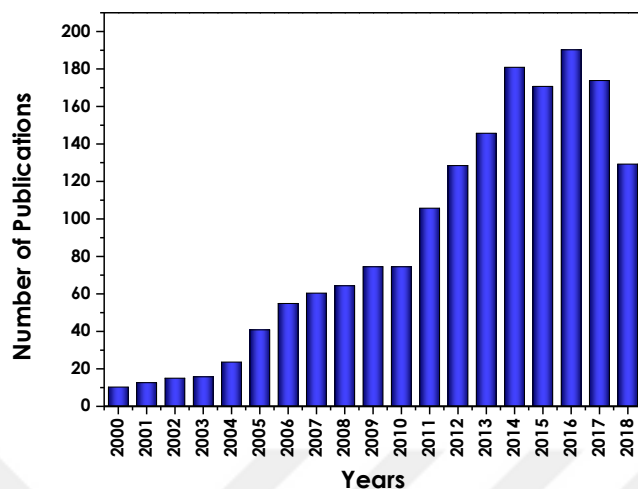


Figure 1.1: Yearly statistics of numbers of publications on ZnO [6]

The fields of implementations of ZnO are not constrained only with solar cells. Cutting-edge technologies promote the utilization of these metal oxides in optoelectronic devices, displays, diodes, sensors, and so on [7–10]. Even though the large band gap of $\sim 3.37\text{eV}$ comes across as a disadvantage, at first sight, ZnO allows the possible band gap engineering and in specific optoelectronic device applications, this large band gap even turns into an advantage culminating in a strong luminescence [11].

1.3. Semiconductors

Based on their electrical conductivities materials can be classified into three categories which are conductors, semiconductors, and insulators [12]. The electrical conductivities of semiconductors reside in-between highly conductive metals and dielectrics. Semiconductor materials are sorted into two types known as elemental and compound semiconductors. Silicon (Si) can be given as an example for an elemental semiconductor that consists of a single element only. Compound semiconductors are those containing more than one element in their structure such as ZnO, gallium arsenide, indium phosphide, etc.

1.4. Zinc Oxide

Semiconductor-based devices developed in the last few decades have shown a tremendous increase in the tendency to implicate ZnO into their structures. The reason for this growing interest in ZnO is due to its highly promising and unique material properties such as direct band-gap of 3.37eV, outstanding electron transfer efficiency, stability, electron mobility, a large variety of synthesis methods, nontoxicity, low exciton binding energy, and so on [6]. Although at first sight the wide band-gap of ZnO is considered as a disadvantage, this metal oxide possesses an excellent potential for implementation into optical devices used in the blue-UV range . The variety of synthesis techniques allows the attainment of the final ZnO product with different material properties [13,14]. Among these varying material properties, band gap and morphology tunability are the ones that directly influence the optoelectronic features of material due to their effect on the absorptivity and energy band.

1.5. Crystal Structure of ZnO

ZnO can be crystallized in four main forms which are hexagonal wurtzite, cubic zincblende, cubic rocksalt and single-crystalline ZnO. Among these listed crystalline structures, hexagonal wurtzite (Figure 1.2) is the most thermodynamically stable and therefore most frequently encountered crystal phase. Due to the hexagonal close-packed crystal structure of ZnO every single Zn atom is surrounded by four oxygen atoms.

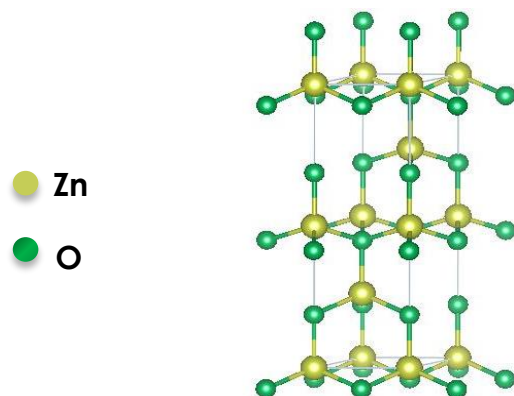


Figure 1.2: Hexagonal wurtzite crystal structure of ZnO

1.6. Electronic Properties

ZnO is a wide band-gap semiconductor (3.37eV) due to which it appears to be transparent in the visible range at room temperature. The 2p levels of oxygen result in the formation of the top region of the valence band, while the 4s level of Zn generates the bottom of the conduction energy band. The presence of a large band gap possesses certain advantages such as operability at high temperature and power outputs, larger breakdown voltages, higher and stronger luminescence ability [11].

ZnO is typically found to exist in n-type form, in addition to the fact that it is highly difficult to achieve this metal oxide semiconductor in p-form [6]. Native defects and undesirably integrated impurities like oxygen /zinc vacancies and oxygen/zinc interstitials are frequently encountered within the ZnO crystal structure [15]. The presence of such defects and impurities results in the formation of intermediate energy states that affect the electronic properties and band structure of the material.

1.7. Synthesis Methods of ZnO

Various methods of ZnO thin film and nanoparticle synthesis can be encountered in the literature. A large assortment of different one dimensional (1D), two dimensional (2D), and three dimensional (3D) nanostructures exist for ZnO ranging from rods and needles to flowers, urchins, and snowflakes. Each of the obtained ZnO nanostructures possesses different material properties and can be synthesized by a large variety of methods. These methods can be classified into 2 basic categories which are solution and non-solution-based synthesis techniques. Each synthesis process requires their own reaction conditions and has certain thermodynamic equilibrium parameters that either permits or inhibit the growth of nanostructures in certain directions.

Solution-based synthesis methods are highly preferred in the literature due to their certain advantages like facile synthesis steps, low cost, control over several parameters such as reaction medium, pH, temperature and duration of reaction, etc. Moreover, these synthesis methods do not have any necessity for expensive equipment utilization. Hydrothermal synthesis, chemical bath deposition (CBD), successive ionic layer adsorption and reaction (SILAR), and electrodeposition are among the most commonly encountered solution-based ZnO synthesis methods. The easy control that is possible to maintain over solution based methods and suitable growth environment eventuate in the formation of a large variety of

1D-3D ZnO nanostructures [6,14]. Table 1.1 briefly summarizes several solution-based techniques with changing precursor and reaction conditions that result in various morphology formations. Non-solution-based methods are also highly preferred for ZnO synthesis. Vapor deposition (Chemical (CVD) and Physical (PVD), sputtering, atomic layer deposition (ALD) and epitaxial growth techniques are among the most preferred non-solution-based methods [16–18]. The major disadvantage of these synthesis processes is the requirement for ultra-high vacuums, precise control over temperature and pressure which turns into a highly expensive device necessity. In vacuum-based techniques the control over morphology is also highly difficult to maintain since the utilization of surface directing agents is not possible in these processes [17].

Table 1.1: Different solution-based ZnO nanostructure synthesis techniques with various reaction parameters

Synthesis Method	Precursor & Reaction Conditions	Obtained Nanostructure	Ref.
CBD	Zinc nitrate hexahydrate ($\text{Zn}(\text{NO}_3)_2 \cdot 6\text{H}_2\text{O}$); Hexamethylenetetramine (HTMA) ($\text{C}_6\text{H}_{12}\text{N}_4$); Polyethyleneimine (PEI) at $T = 80 - 90^\circ\text{C}$	Nanorod	[19]
Sol-gel	Zinc acetate dehydrate ($\text{Zn}(\text{CH}_3\text{COO})_2 \cdot 2\text{H}_2\text{O}$); Ethylene glycol (EG) or diethylene glycol (DEG) at 160°C for 1 h	Nanorhombic flake & Nanosphere	[20]
Hydrothermal	$\text{Zn}(\text{CH}_3\text{COO})_2 \cdot 2\text{H}_2\text{O}$; N,N-dimethylformamide ($\text{C}_3\text{H}_7\text{NO}$) at 90°C for 4 h	Nanoflower	[21]
Microwave	$\text{Zn}(\text{CH}_3\text{COO})_2 \cdot 2\text{H}_2\text{O}$, Ammonium hydroxide (NH_4OH), 20 min at 140°C , 600 W	Cauliflower-like morphology	[22]
Emulsion	$\text{Zn}(\text{CH}_3\text{COO})_2$, NaOH and KOH, cyclohexane, nonionic surfactants reaction: ambient temperature	Nanocluster	[23]

CHAPTER 2

2. INVESTIGATION OF STRAIN EFFECTS ON PEC PERFORMANCES OF FLEXIBLE ZnO ELECTRODES

2.1. Introduction

Sun providing an unlimited amount of energy to the earth can be directly converted into electricity or can be used as an input for the generation of other energy sources. H₂ is highly valuable in contemporary energy systems as it is one of the major candidates for being utilized in energy storage devices. Photoelectrochemical (PEC) hydrogen generation systems consisting of semiconductor based-electrodes are mainly used to convert photons into chemical or electrical energy [24]. In solar water splitting systems, semiconductor material choice is done based on its electrical properties and band gap. The conduction band edge position of the selected material should bear negative potential higher than that of water reduction in order to split water into hydrogen. Consequently, the potential value of the valence band edge should exceed the oxidation potential to release oxygen gas as a product. Typically, n-type metal oxide semiconductors like ZnO and TiO₂ possess suitable band edge potentials for successful water splitting. Additionally, the utilization of metal oxides instead of their sulfide compounds is preferable due to the outstanding stability against photocorrosion of metal oxides within the electrolyte solution [6,25,26]. A large variety of 1D to 3D ZnO nanostructures can be encountered in the literature to be implemented into PEC systems as photoanode materials. As a recent trend, varying and optimizing 1D-3D ZnO nanostructures via certain steps such as etching or branching has resulted in performance increases due to increased surface area and absorption. As an example, a study conducted by Liu et al. in 2017 focuses on the transformation of ZnO nanowire formations into nanorods, tubes and disks consequently [27]. The process actualizes via chemical treatment process resulting in increased light pathway due to multi-reflections.

2.2. Experimental Methods

Stainless steel foils were purchased from Comet Metals, Inc. (Ohio, USA). ZnO (99.99% pure) targets used during RF sputtering were purchased from Plasmaterials, Inc. (California, USA). Zinc nitrate hexahydrate ($\text{Zn}(\text{NO}_3)_2 \cdot 6\text{H}_2\text{O}$), Zinc acetate dihydrate $\text{Zn}(\text{C}_4\text{H}_6\text{O}_4 \cdot 2\text{H}_2\text{O})$ as the source of the anionic species, and urea $(\text{NH}_2)_2\text{CO}$ were purchased from Sigma Aldrich (Schnelldorf, Germany). All chemicals were of analytical grade and were used without any purification.

2.2.1 Preparation of ZnO Electrodes

The stainless steel foils serving as substrate for ZnO seeding layers have been washed in acetone, alconox solution, deionized water, and 5% v/v acetic acid solution and dried with nitrogen gas before being loaded into the vacuum chamber. The zinc oxide (ZnO) seeding layers have been deposited on previously cleaned stainless steel substrates by RF magnetron sputtering (Vaksis Midas PVD-MT/2M2T, Ankara, Turkey). The thin film deposition has been carried under the pressure of 7.6×10^{-6} Torr in a 99.999% argon gas containing sputtering chamber. The flow rate of argon gas has been set to 44.4 sccm. ZnO thin film sputtering has been performed at 60W plasma discharge power for 9 minutes. Rapid Thermal Annealing (RTA) has been applied on sputtered substrates in order to increase the grain size and decrease the number of grain boundaries that bear the excess energy. The annealing process has been performed at 300 °C chamber temperature ($3^\circ\text{C}/\text{s}$) for 30 minutes.

As the proceeding step, SS/ZnO substrates have been placed into the chemical bath for 1D-3D ZnO nanostructure growth. Three different morphologies, Nanoflower (NF), Nanosheet (NS), and Nanowire (NW) have been synthesized by using different anionic species. The synthesis of NF and NS structures have been carried out in aqueous solutions containing 1.0M of urea as a precursor and 0.05M of $\text{Zn}(\text{C}_4\text{H}_6\text{O}_4 \cdot 2\text{H}_2\text{O})$ and $(\text{Zn}(\text{NO}_3)_2 \cdot 6\text{H}_2\text{O})$ as zinc sources, respectively. The acidities of both solutions have been adjusted via pH meter to exactly 4.5 by using acetic acid and nitric acid solutions, respectively. SS/ZnO substrates have been immersed into chemical bath solutions vertically and the reactions have proceeded at 80°C for 3 hours. The final ZnO thin film products have been washed with deionized water to get rid of excess unbounded film on the surface and annealed in a calcination furnace at 300 °C for 30 minutes

under atmospheric conditions in order to evaporate the remaining anionic species and obtain pure ZnO product.

The synthesis of ZnO in NW morphology has been performed via dissolving $(\text{Zn}(\text{NO}_3)_2 \cdot 6\text{H}_2\text{O})$ (0.1M) in deionized water and adding ammonium hydroxide of (2% v/v) into the solution where a noticeable change occurs as a result of white precipitate formation. The growth of NWs in CBD has been carried out at 80°C for 1 hour. The deposited samples have been further washed with DI water and ethanol for cleaning purposes and annealed at 300°C for 30 minutes.

2.2.2 Characterization of ZnO Electrodes

Scanning electron microscopy (SEM) (QUANTA 400F Field Emission SEM) has been carried out in order to analyze the morphology, feature size, homogeneity of the obtained ZnO thin films. The crystallinity of synthesized ZnO nanostructures has been determined through X-Ray Diffraction (XRD) analysis. XRD analysis has been performed via PANalytical/ Philips X'Pert MRD system. X-ray photoelectron spectroscopy (XPS) has been performed to reveal the elemental composition and defect detection purposes. The presence of defects and impurities has been further verified through photoluminescence (PL) and Raman spectroscopies. Optical characterization of materials has been analyzed via UV/Vis (Perkin Elmer, Lambda 650S) for the determination of reflectance and absorbance characteristics of thin films.

The photoelectrochemical (PEC) performances of three different ZnO films have been investigated in a standard three-electrode system with SS/ZnO thin films being used as the photoanodes and Platinum (Pt) and Ag/AgCl playing the roles of counter and reference electrodes, respectively (Figure 2.1). The PEC analyses have been conducted in an aqueous solution containing 0.25M/0.35M $\text{Na}_2\text{S}/\text{Na}_2\text{SO}_3$ at the pH value of 12. Gamry750 Potentiostat/Galvanostat/ZRA has been used as the sourcemeter for the conduction of potentiostatic and voltammetric analyses. For the evaluation of performance and efficiency data, voltammetric experiments have been conducted at light and dark conditions, subsequently by using Lot Oriel Solar simulator equipped with 150 W Xenon Lamp -. IPCE measurements based on the photoelectrochemical responses of electrodes to specific wavelength values, have been maintained via monochromatic light source Femto-RD5 (FemtoTera,).

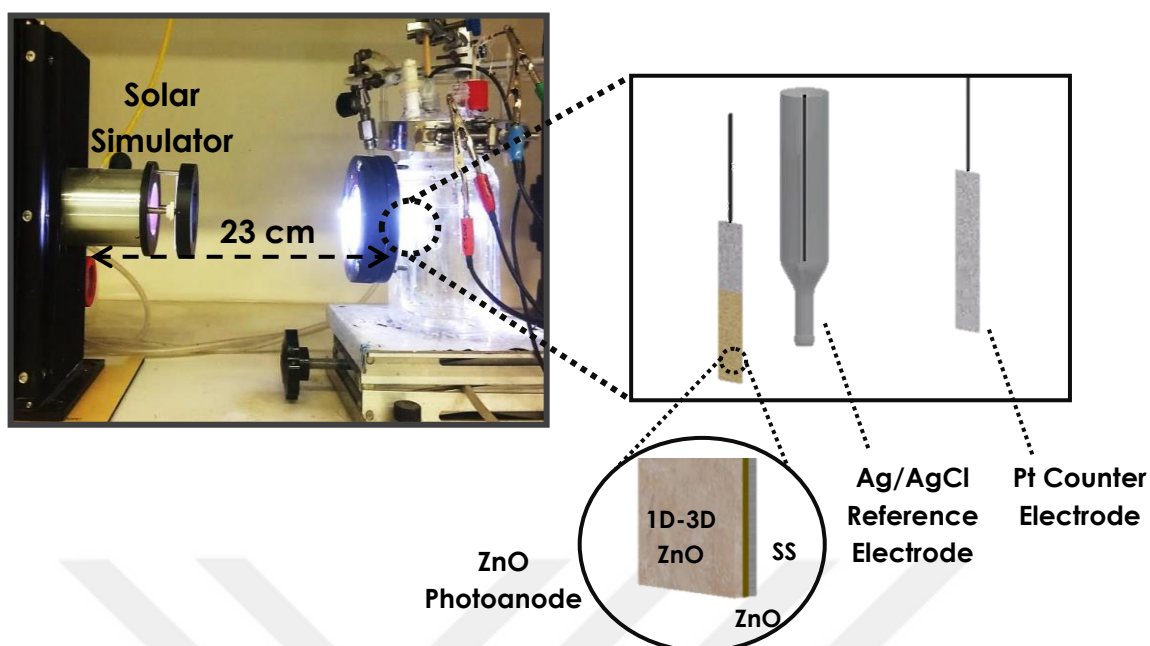


Figure 2.1: Photoelectrochemical water splitting system set-up

2.2.3 Straining Tests

ZnO thin film deposited SS foils have been exposed to mechanical straining from 40 mm of total electrode length to 31mm (Figure 2.2). Two sets of experiments have been conducted for the straining test in which; (1) electrodes have been strained and analyzed directly in their strained forms. SEM analysis and PEC characterizations have been done on these sets of samples and (2) electrodes have been strained and released in multiple number cycles ranging from 10 to 2000 to detect their durability towards continuous deformation.

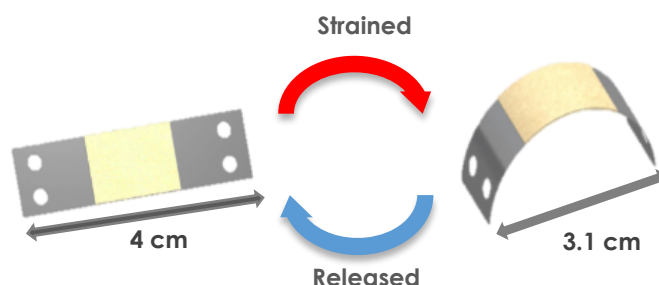


Figure 3.2: Mechanical deformation (straining) applied on ZnO thin films

2.3 Results & Discussion

2.3.1 1D- 3D ZnO Flat Electrodes and Their Characterizations

The morphological changes between synthesized ZnO thin films due to the varying anionic source have been examined via SEM analysis. Figure 2.3 (a) demonstrates the SEM images of 3D ZnO nanoflowers (NF) at different magnifications obtained from $\text{Zn}(\text{C}_4\text{H}_6\text{O}_4 \cdot 2\text{H}_2\text{O})$ anionic precursors. The obtained NFs resemble the misshapen chive flowers and have a diameter of approximately $100 \mu\text{m}$. The nested appearance of NFs from their distant SEM images shows an interconnection between flower resembling features. The second obtained morphology having a sheet resemblance is attributed to as ZnO nanosheet (NS) which is presented in Figure 2.3 (b) and is obtained from $\text{Zn}(\text{NO}_3)_2 \cdot 6\text{H}_2\text{O}$ precursor. In comparison to NF thin film structure, NS homogeneity throughout the sample surface is much poorer and the uniformity is weak. It is also noteworthy to say that, a significant diminution can be observed for NSs compared with NFs, which is directly related to completely different nucleation and sprouting mechanisms [14]. The third morphology investigated in this study is the 1D ZnO nanowire (NW) structures that form a dense and uniform thin film with the feature sizes of 50 nm radii $\times 1.4 \mu\text{m}$ length. (Figure 2.3 (c)). Scotch tape test have been applied on all of the samples at the end of the synthesis in order to assure their successful adhesion onto the substrate. For the evaluation of elemental composition, Energy Dispersive X-Ray (EDAX) analysis has been performed simultaneously with SEM of the analyzed samples. The obtained values summarized in Figure 2.4 show the presence of Zn, O, Fe, and Cr atoms in the structure. EDAX analysis reveals the elemental composition through the X-rays emitted from the sample obtained from the incident e^- beam. The pathway of e^- beam deep into material reaches up to $1\text{-}2 \mu\text{m}$ and therefore the presence of Fe and Cr from the substrate are being detected. NF structured ZnO, among all three thin films, appeared to be the most homogeneous and thick. Therefore, the atomic percentage of Fe is lower in this sample compared to NS and NW. Moreover, the Zn:O ratios in NF (1.5:1.0) structure represent the dominance of Zn-atoms. This ratio is almost 1.0:1.0 for NS and 1.0:1.5 in NW formations. The increase in the dominance of Fe and Cr atoms in the atomic percentages of NS and NW also gives a clue about their thinness in contrast with much thicker NF thin film.

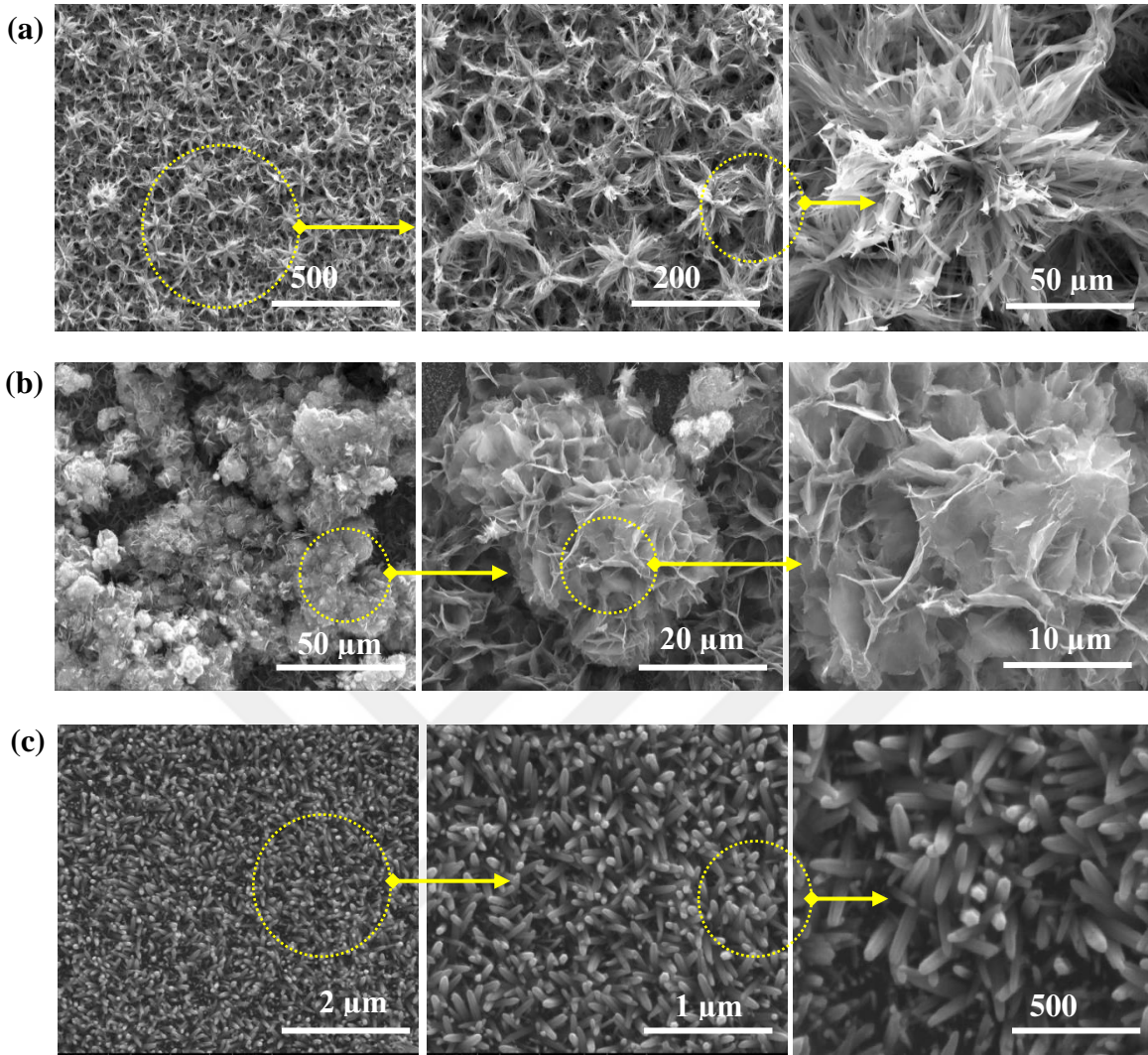


Figure 2.3: SEM Images of ZnO nanostructures of (a) nanoflower, (b) nanosheet and (c) nanowire

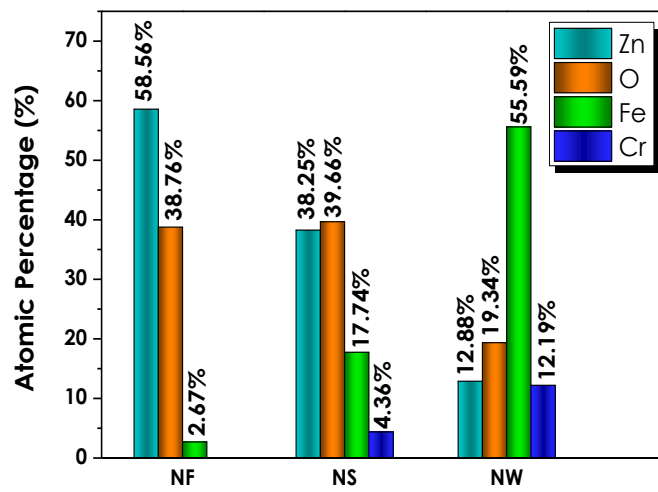


Figure 2.4: Atomic percentages obtained from EDAX analysis of ZnO thin films

The crystal phases of synthesized ZnO morphologies have been identified via XRD analysis (Figure 2.5). The obtained [100], [002], and [101] diffraction patterns at specific 2θ angles for all three nanostructures remark the presence of characteristic wurtzite hexagonal crystal structure. The intensities of diffraction peaks obtained from NF structure appear to be higher than those of NSs which is compatible with the previously discussed SEM images signifying a denser and more homogeneous film formation. Moreover, the strong peak intensities signify better crystallinity and larger crystal domains of NF morphology. Compared to 3D structures, 1D ZnO NW exposes its strongest peak at 34.2° total diffraction angle. This strong diffraction of (002) plane represents the most favored growth orientation of nanowires in the c-axis perpendicular to the substrate. It is also important to note that the indistinct diffraction peaks of (102), (110), and (112) crystal planes imply that the film orientation in other directions is extremely small showing an almost homogeneous NW formation throughout the surface.

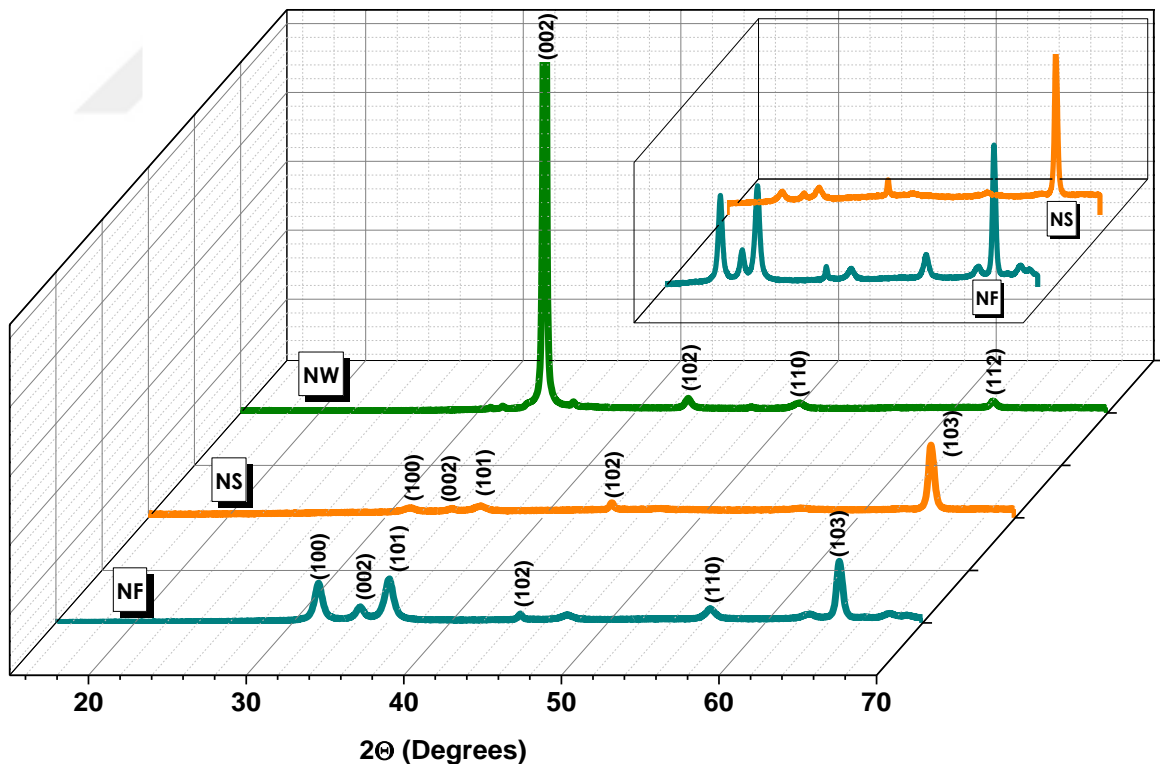


Figure 2.5: XRD crystalline peaks of ZnO Nanostructures

The elemental composition and nature of defects of ZnO nanostructures have been investigated via X-Ray Photoelectron Spectroscopy (XPS). In comparison to EDAX analyses, XPS has an analysis depth of 5 nm and therefore analyzes the top layer of the thin film. Therefore, the XPS survey obtained from all three materials reveals only Zn and O characteristic peaks (Figure 2.6 (a)). The defect analysis has been carried out on O1s spectra at 529 - 532 eV binding energy range for NF, NS, and NW morphologies individually. Gaussian deconvolution has been individually carried out on O1s peak of each ZnO nanostructure. As a matter of fact, due to a different defect content of 1D nanostructures, ZnO NW has been deconvoluted into three peaks while the latter nanostructures possessing 3D morphology have been fitted into two. The binding energies of the appearing deconvolution peaks and their significances are specified in Table 2.1 and shown in Figures 2.6 (b) – (d).

Table 2.1: Ratios of deconvoluted oxygen peak intensities [28–30]

	eV	O ₁	eV	O ₂	eV	O ₃
ZnO NF	530.9- 531.3	O ₂ ⁻ of ZnO	531. 7- 533. 5	Loosel y bound O ₂ on surface	-	-
ZnO NS	530.9- 531.3	O ₂ ⁻ of ZnO	531. 7- 533. 5	Loosel y bound O ₂ on surface	-	-
ZnO NW	529.4	O ₂ ⁻ of ZnO	530. 9	Zn-OH	531.9	Chemisorbed O ₂

The O₁ peak relating to the oxygen remaining within the ZnO crystal structure appears at lower binding energies for all three structures. On the other hand, both of the 3D morphologies generate an O₂ peak that stands for the oxygen deficiency in the ZnO nanostructure. This deficiency in oxygen has been detected via loosely bound oxygen O₂ on the film surface. In a different scenario of NW, The density of each defect within the nanostructure has been evaluated by contrasting the intensities of O₂ and O₁ peaks. By formulating an O₂/O₁ ratio for each nanostructure, it can be observed that ZnO nanoflowers possess a large number of

oxygen vacancies in their structure generating a ratio of 0.77. This value drops to 0.61 for ZnO nanosheets. The ratios of intensities of deconvoluted O2/O1 peaks can be used as a clue for the determination of defect density in the ZnO crystal structure. The conducted calculations indicate the higher oxygen vacancy density in ZnO NFs with a ratio of 0.77 while for ZnO NS this ratio is around 0.61. A large variety of studies conducted in the field of ZnO defect analyses have resulted in the constitution of a relation between V_o presence and photoelectrochemical performances. It has been established that oxygen vacancies act as inherent donors resulting in the formation of new intermediary energy levels within the material band gap. These intermediate levels have been determined to facilitate the electron transfer and collection and increase the absorption coefficient of the material [31–37].

Photoluminescence (PL) and Raman analyses have been carried out for purpose of verification for the presence of oxygen vacancies and other types of defects. PL spectra of NF, NS, and NW thin-film given in Figure 2.7 reveal significant peaks within 370-450 nm and 450-900 nm ranges. Hydrothermally grown ZnO nanostructures possess a large variety of defects and $Zn(OH)_2$ is the one that causes the main charge entrapment due to the formation of a midgap that generates characteristic photoluminescence peaks [38–40]. Emission at wavelengths higher than 550 nm (yellow-green region) are resulting from trapped e^- -hole recombinations. The excitonic emissions occurring at wavelengths ≥ 380 nm (UV) arise due to Coulomb forces between pairs of electrons and holes. The main source of these emissions has been stated to be the oxygen vacancies, although the main cause of green emissions is still controversial [41,42]. The photoluminescence spectra of all ZnO structures show the existence of excitonic emissions at approximately the same wavelength values within the UV region. However, by analyzing the differences in green-region originated luminescence of NF, NS, and NW individually, it can be seen that the NF structure brings out a sole, intense peak at 550 nm that corresponds to the presence of V_o and a shoulder at relatively low concentrations that can be attributed to zinc vacancies (V_{Zn}).

(a)

(b)

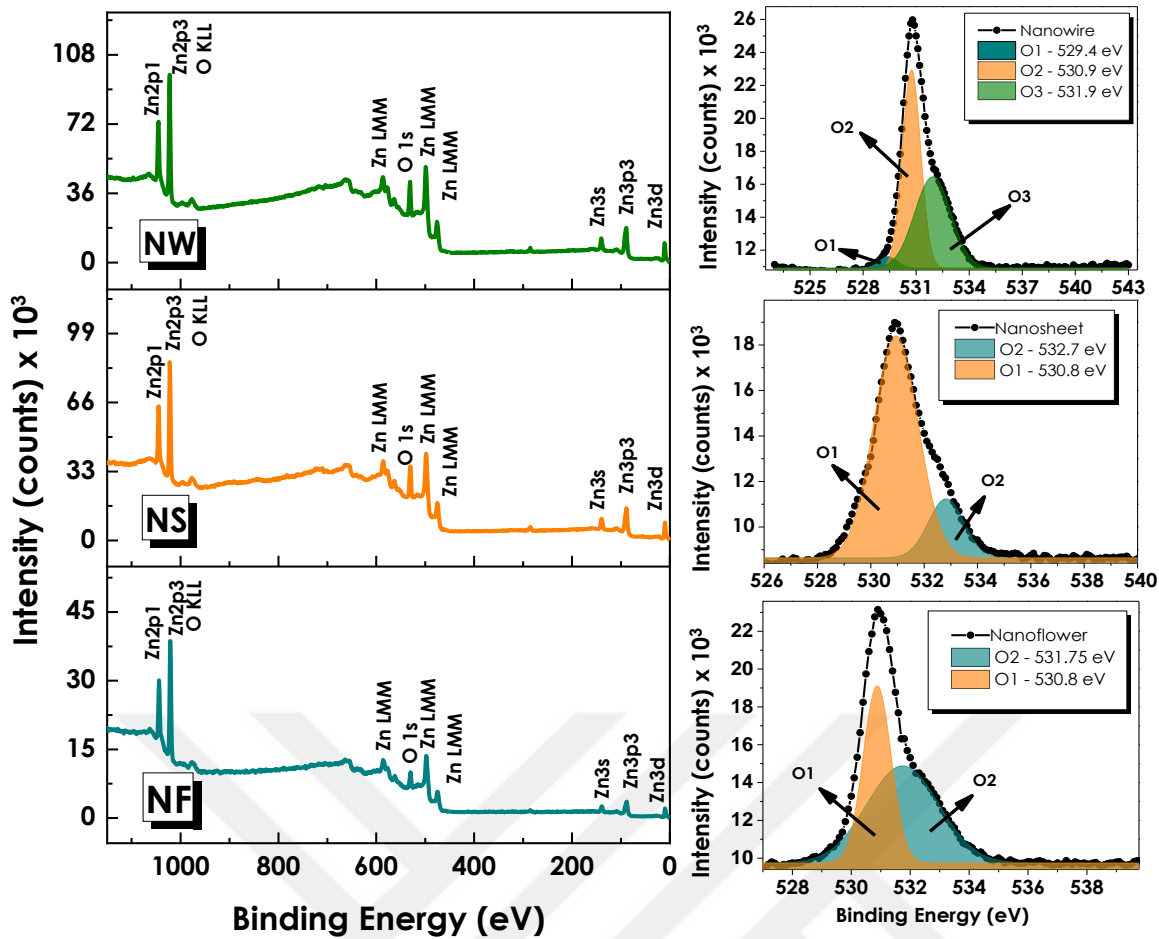


Figure 2.6: XPS analysis revealing the (a) overall elemental composition of ZnO thin films and (b-d) Individual O1s peak deconvolutions for defect identification

Besides, the comparatively high peak sharpness of NF can be related to its higher numbers of defects. For a more in-depth investigation of PL spectra, each spectrum in the defect-based emission region is decomposed into three Gaussian peaks. These bands correspond to (I) 540-580nm (O_I), (II) 580-640nm (O_{II}), and (III) 640-740nm (O_{III}) wavelength ranges, respectively [29]. Several studies report that the Gaussian band in the O_I and O_{II} regions represent the mono-charged (V_o⁺) and double-charged (V_o⁺⁺) oxygen gaps, respectively [37]. It was found that the last Gaussian band in the O_{III} region stands for either zinc vacancies or oxygen interstitials (O_i) [43]. Analyzing the NF deconvolution band individually, it can be clearly seen that O_I peak exceeds O_{III} by intensity which can be interpreted as a more dominating presence of oxygen vacancies. For NS formations, a relatively higher stronger intensity of O_{III} peaks can be observed. Nevertheless, oxygen vacancy originated O_{II} peak still possesses domination over other types of defects. In contrast to NF and NS, O_{III} band is more dominant in pristine NW structures which can be correlated with a more intense presence of zinc vacancy or oxygen

interstitial-like defects. Table 2.2 gives an explicit comparison of Gaussian peak intensity ratios. Moreover, it should be pointed out that PL data has shown a strong agreement with XPS characterization outcomes.

Raman analyses were performed under 532 nm laser excitation and the obtained results were elaborated according to different nanostructures of ZnO (Figure 2.8). All three samples produced nearly similar peaks where 330, 440, and 580 cm^{-1} were the most intense ones. Peaks appearing at 330 and 440 cm^{-1} can be attributed to boundary $E_{2H}E_{2L}$ phonons and E_2 mode of the ZnO, respectively. The latter peak (580 cm^{-1} - E_1 mode) is generated by LO mode which is a nonresonant scattering that occurs due to the defects within the structure [44–46]. Mostly oxygen vacancies and zinc interstitials are known to contribute to this kind of LO mode. It is also important to note that the low peak intensities of ZnO NF are the result of their intense fluorescent emissions.

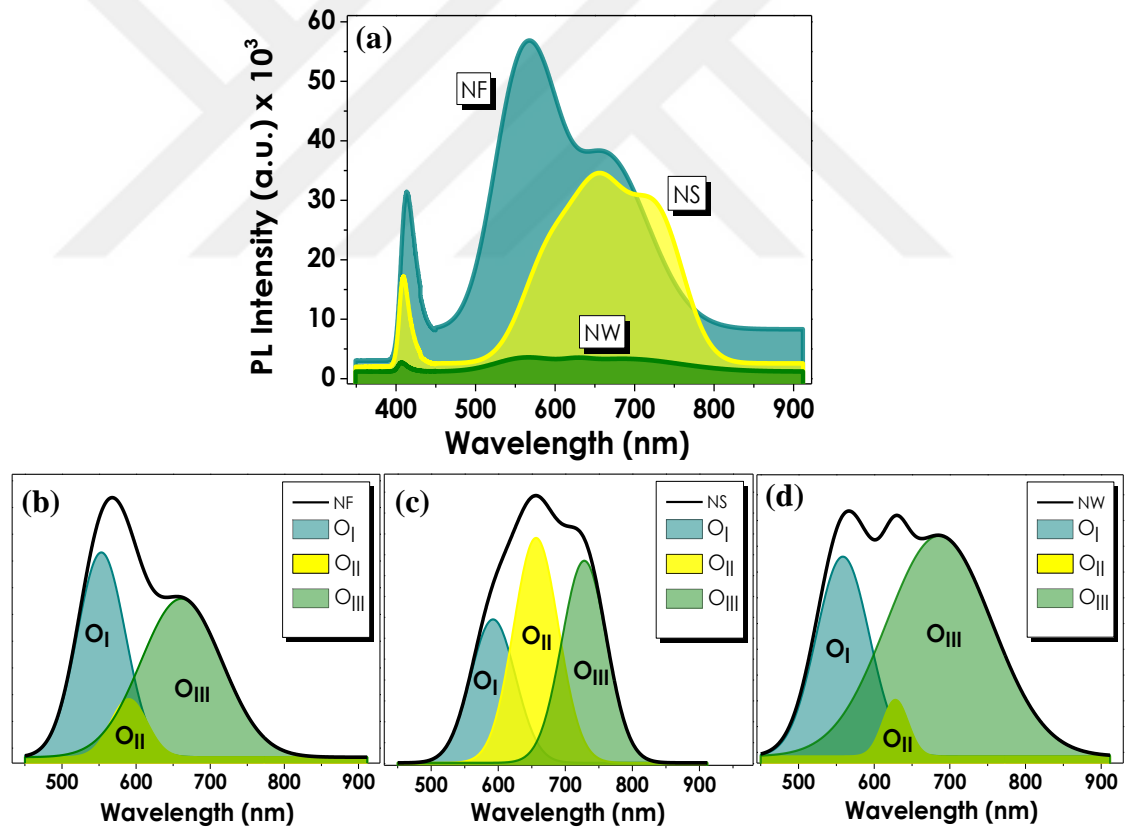


Figure 2.7: (a) Total photoluminescence spectra and PL peak deconvolutions of (b) NF, (c) NS, and (d) NW morphologies, respectively.

Table 2.2: Ratios of deconvoluted oxygen peak intensities obtained from PL spectra.

ZnO Morphologies	O _i /O _{iii}	O _{ii} /O _{iii}
Nanoflower	1.22	0.50
Nanosheet	0.73	1.10
Nanowire	0.94	0.52

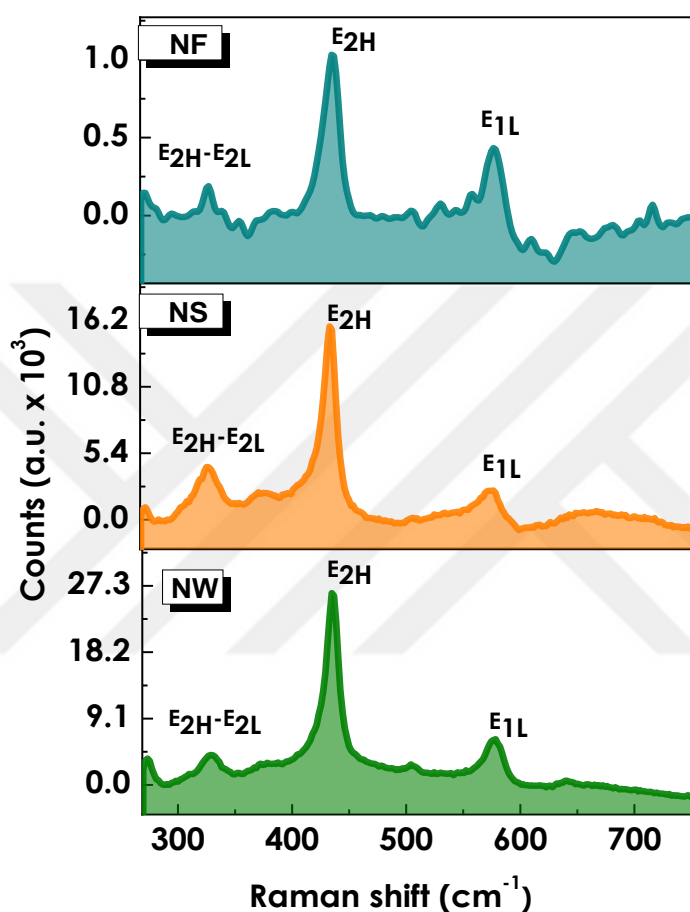


Figure 2.8: Raman spectra for 1D - 3D ZnO nanostructures with identified peaks and defect examinations.

The photoelectrochemical water splitting performances of ZnO thin films have been studied under illuminated (1sun) and dark circumstances (Figures 2.9 (a) and (b)). NF-composed thin films generated the highest current density of 1.54 mA cm^{-2} under zero bias voltage (vs. Ag/AgCl). This superior performance is considered to be the result of higher crystallinity and the dominant presence of V_o within NF formations. The NS and NW films with 1.14 and 0.8 mA cm^{-2} performance data, respectively, have turned out to be in good agreement with energy dispersive X-

ray data that validated the excess presence of oxygen. The durability of thin films throughout consecutive test cycles has been analyzed via stability test. Here, with respect to Ag/AgCl reference electrode, under 0 V_{bias}, thin films have been subjected to repeating illumination and darkening sets (Figure 2.9 (c)). NF-structured thin films produced comparatively better current and fair durability performance through the given test period. NS and NW structures, on the other hand, have generated lower current densities while exhibiting bettermost stability within 7200 sec. test period.

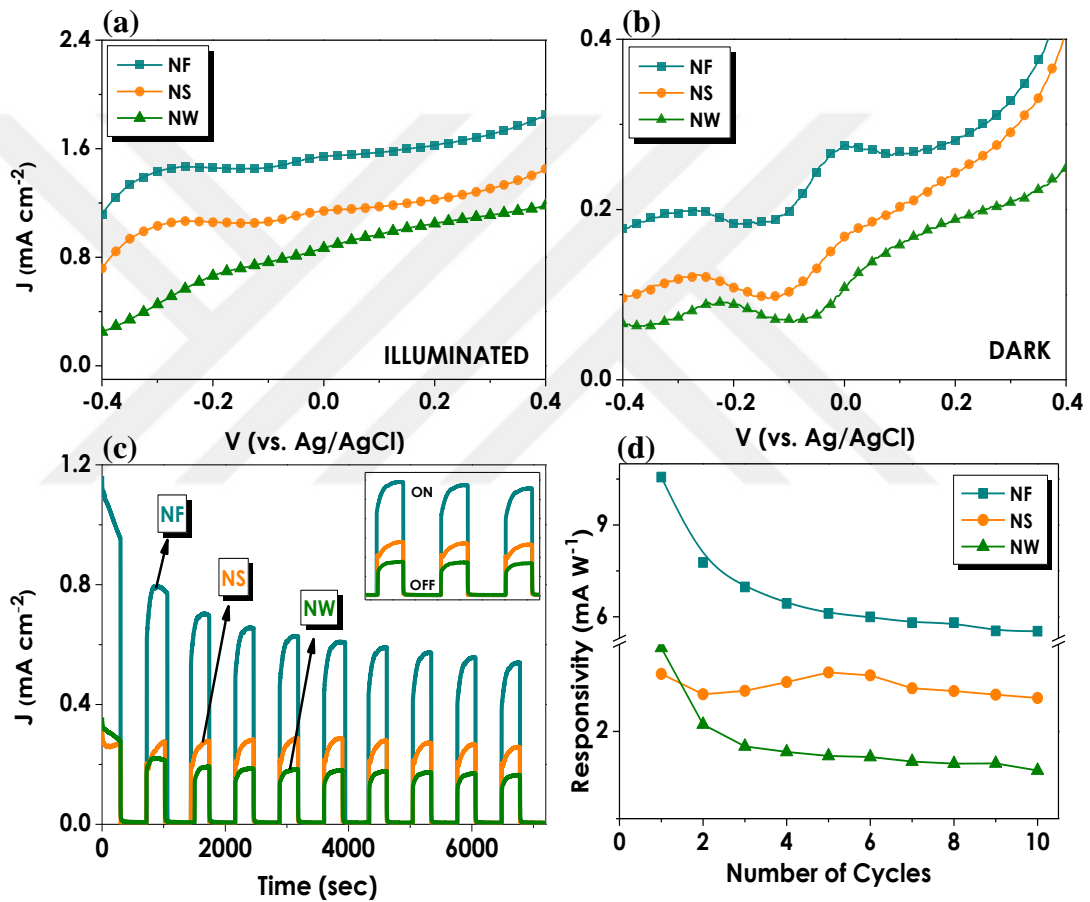


Figure 2.9: Photoelectrochemical characterizations of ZnO thin films in (a) illuminated and (b) dark conditions; (c) Stability analysis at 0 V_{bias} under consecutive light ON/OFF cycles and (d) responsivities evaluated from the obtained stability values.

The following Equation 2.1 has been implemented in order to calculate the responsivities of ZnO thin films.

$$R = (J_{ill} - J_{dark}) / P_{light} \quad (\text{Eq. 2.1})$$

Figure 2.9 (d) clearly demonstrates that NF-structured thin films display a much stronger responsivity to light in the primary cycles while remaining almost constant through the last 6 sets. In a similar manner, NW-structured films also possessed relatively higher responsivities in the initial 4 cycles while further-reaching an approximately constant value of light sensitivity. NS, on the other hand, shows a very steady responsivity through all 10 cycles.


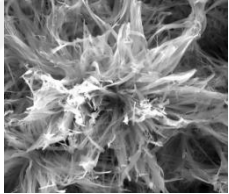
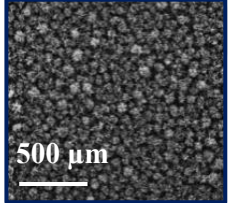
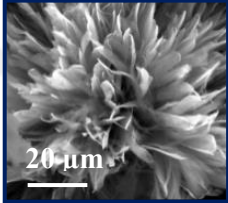

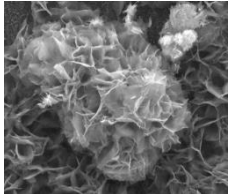
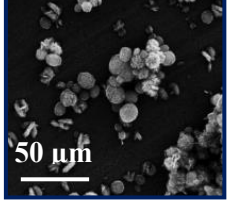
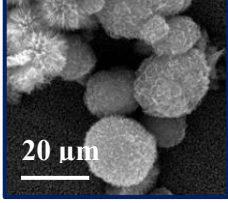

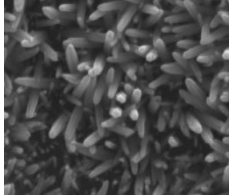
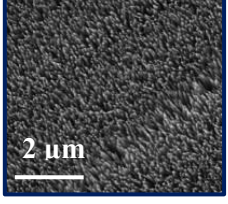
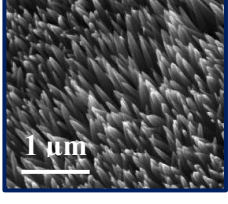
2.3.2 Application of Straining Test on ZnO Photoelectrodes and Their Detailed Characterizations

The scale-down of systems, transition to flexible electronic appliances, and the upcoming trends of shrunk nanotechnological systems have been among the primary motivations that drove us towards the utilization of flexible stainless steel foils as substrates. At this stage, parameters like the degree of electrode straining and durability of ZnO thin films during the act of flexing have been in the center of attraction. In Table 2.3, a clear display of photoelectrode samples during straining is given next to their SEM images. The electron microscopy images within the table explicitly show the contrast between flat and strained nanostructures. It is crucial to underline the fact that all substrates have been subjected to flexing after the thin films have been deposited. Therefore, a direct effect of mechanical strain can be observed on all three nanostructures and on the homogeneities of those films.

Analyzing the primary row of Table 2.3, it can be observed that deformed and misshapen flower-like formations have transformed into blossomed, wide nanoflowers. A significant difference can specifically be seen in the petals constituting the overall structure. Here, in their flat forms, petals have been observed to lie in a manner that receives the incoming radiation only with a small portion of their constitution. On the other hand, after being strained, those petals have revealed their bodies towards incoming light consequently increasing the surface area of absorption. Moreover, as a result of the flexing act, we have been able to observe the actual shapes of petals that resembled thin rectangles.

In the case of NSs, a completely different scenario has been witnessed. In contrast to NF films that remained homogeneous after being strained, NSs showed relatively poor durability to straining. The low degree of adhesion of these 3D formations resulted in the outpouring of nanostructures that generated a much balder thin film. 1D NWs have demonstrated a very idiosyncratic appearance subsequent to straining. In this case, analyzing the difference between SEM images of NWs, a more unidirectional inclination can be monitored for these strained films that appeared much more randomly distributed in their flat forms. This transition from a chaotic arrangement to a neat order is assumed to positively impact the absorption performance of ZnO NWs.

Table 2.3: Morphological comparison of strained ZnO thin film samples from SEM images

ZnO	Sample Image	Flat SEM	Strained SEM	
NF				
NS				
NW				

The light absorption performance of ZnO photoanodes (both flat and strained) has been measured through UV/Vis analysis. NF-structured thin films preserved their homogeneities in both flat and strained forms. Therefore, the variation in optical data of these nanostructures is insignificantly small (Figure 2.10 (a)). However, a tiny

increase in the absorption values within UV range has been attributed to blossomed nanoflower petals. A much more distinguishable decline in absorption values has been detected for NSs which are in good agreement with the previously discussed SEM images (Figure 2.10 (b)). It can be clearly stated that the electron microscopy images of NSs exhibiting the thin film exfoliation have now been validated with optical data. Figure 2.10 (c) demonstrates the absorption performance of NWs which have proven to be the most favorably affected thin-film among all three. Looking at the optical data, the effect of the contribution of NW bodies to the overall absorption performance can be evidently observed.

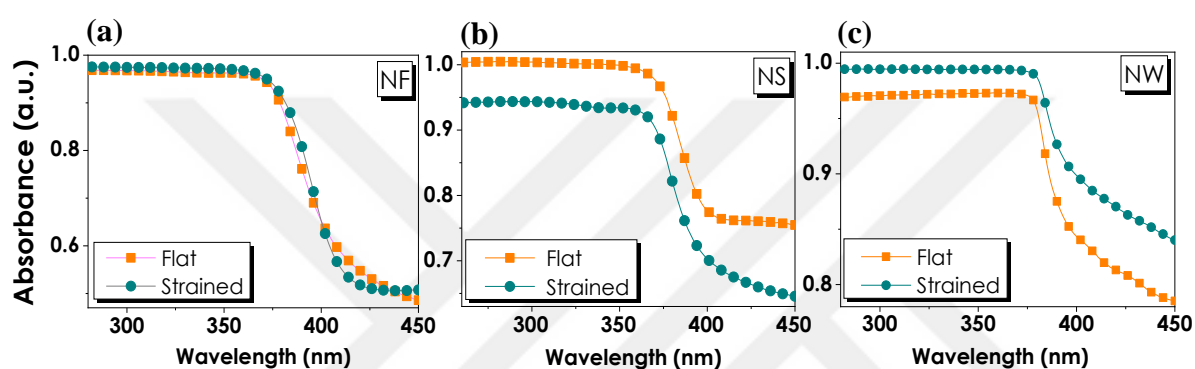


Figure 2.10: Optical characterizations of ZnO nanostructured thin films; (a) NF, (b) NS, and (c) NW via UV/Vis.

The water splitting performance of strained ZnO thin films has been analyzed in the exactly same PEC environment. All data has been collected with respect to Ag/AgCl reference electrode. Figures 2.11 (a) and (b) demonstrate the J-V data obtained under illuminated and dark conditions. The primary difference to be commented on is the significant drop in NS's current generation performance that placed that thin-film below the performance of 1D NW. More specifically, while generating a current density of approximately $1.15 \text{ mA}\cdot\text{cm}^{-2}$ in their flat states, NS has dropped to $\sim 0.75 \text{ mA}\cdot\text{cm}^{-2}$ after the act of straining. NFs have shown an increase of 10% which has been an expected outcome due to the tiny variation in their optical absorption data. Lastly, NWs have demonstrated the most noticeable improvement in their current generation performance resulting in $1.2 \text{ mA}\cdot\text{cm}^{-2}$, which is $\sim 38\%$ higher in contrast to their flat forms.

The same trend has been detected in stability and responsivity tests where NF and NW films sequentially possessed the highest performances in comparison to NSs.

Figure 2.11 (c) demonstrates the stabilities of strained films through 7200 seconds of the test period. In contrary to the flat films, strained ones displayed relatively poor durability to consecutive light-on/light-off cycles. Nevertheless, NF films have demonstrated a less severe decrease in current generation data. Analyzing the responsivity data given in Figure 2.11 (d), it can be concluded the contribution of NWs' bodies to light absorption has positively affected their responsivities to the irradiation through 8 cycles out of 10.

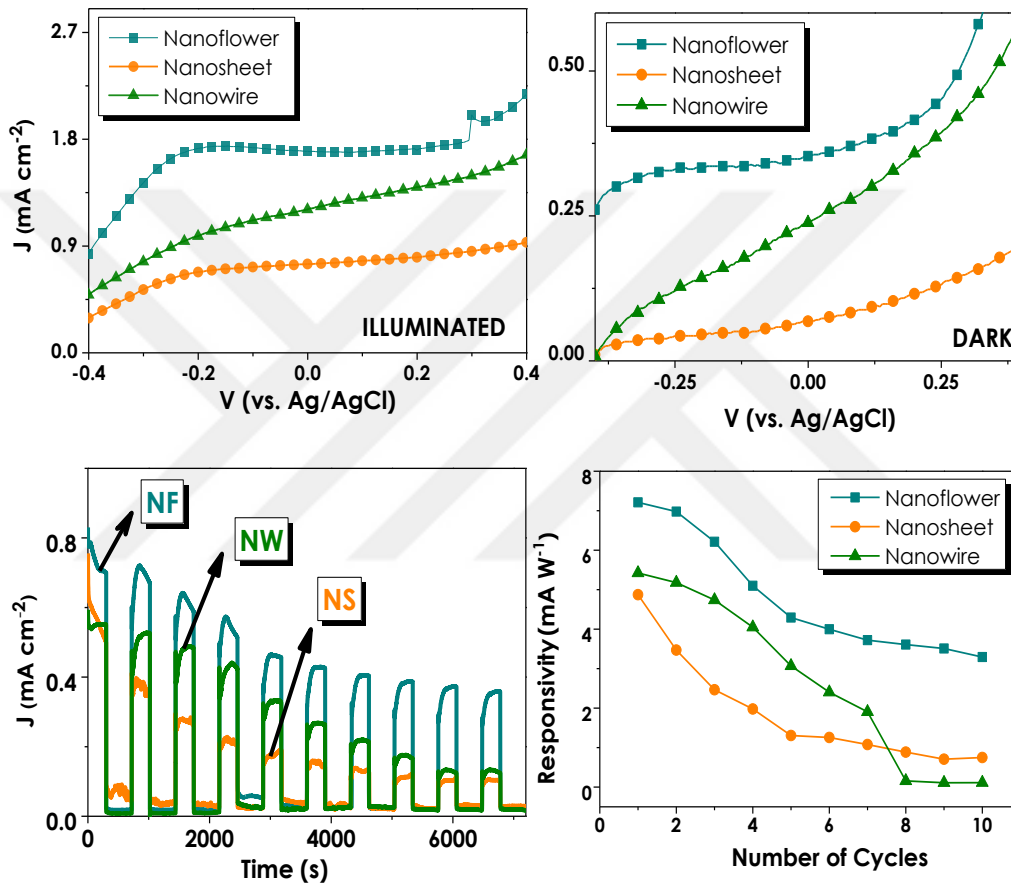


Figure 2.11: Photoelectrochemical characterizations of strained ZnO thin films in (a) illuminated and (b) dark conditions; (c) Stability analysis at 0 V_{bias} under consecutive LIGHT ON/OFF cycles and (d) responsivities evaluated from the obtained stability values.

The amount of photocurrent with respect to the rate of incident incoming photons has been evaluated for a good measure. This quantitative analysis, also known as incident photon-to-current conversion efficiency or IPCE, has been conducted under a monochromatic light generator. Equation 2.2 has been used to convert the photocurrent generated under different incoming wavelengths into efficiency.

$$IPCE (\%) = \frac{I_{ph} (A)}{P(W)} \times \frac{1240}{\lambda(nm)} \times 100 \quad (\text{Eq. 2.2})$$

Here, I_{ph} , λ and P stand for photocurrent density, the wavelength of the incoming monochromatic irradiation, and power density of the light, respectively. The wavelength of the incoming light has been varied between 367 and 540 nm which comprise the UV-visible region. All three nanostructures have displayed a remarkable responsivity at low wavelengths in both flat and strained forms with a near-zero response to dark (Figures 2.12 (a) and (b)). Individual responsivities towards certain wavelength values played a significant role. Nevertheless, interpreting the overall efficiencies through the whole range of applied irradiation has been decided to be more expressive. Figures 2.12 (c) – (e) give individual nanostructure comparisons for flat and strained photoelectrodes. A significant improvement in photon-to-current conversion efficiencies has been observed for NF and NW films, specifically. For strained 3D NFs, the performance within the UV region has been substantially increased from ~13 to 25% and remained almost similar within the visible range. NS structures, despite their drastic exfoliation from the surface after being flexed, have generated a performance quite close to their flat forms. NWs, on the other hand, dominate the IPCE outcomes within the UV range by escalating from 28 to almost 70% as a result of straining.

Mott-Schottky (MS) and electrochemical impedance spectroscopy (EIS) techniques have been implemented in order to measure intrinsic electric material features (flat band potential, charge carrier concentration) and understand the electrode/electrolyte interface dynamics, respectively. In MS measurements, the measurements have been conducted within exactly the same electrolyte solution but without the irradiation under 100 Hz frequency. The flat band potential (V_{fb}) of photoelectrodes, which represents the potential at which the depletion layer at semiconductor-electrolyte interface annuls, is evaluated from the x-intercept of $1/C^2$ vs. V plot [47,48]. The obtained V_{fb} outcomes with respect to Ag/AgCl are -0.56, -0.53 and -0.36V for NF, NW, and NS-structured thin films, respectively. The majority carrier concentration of each thin film is specified as an inset in Figures 2.13 (a) – (c) showing a positive slope which is in accordance with n-type ZnO. The electrode/electrolyte interface dynamics have been represented in form of Nyquist plots given in Figures 2.13 (d) – (f). Standard Randles circuit containing resistors, constant phase element (CPE), and Warburg elements have been used to

fit the NF and NS Nyquist plots. For the aforementioned films, a more diffusion dominant carrier transport nature has been detected. The details of circuit elements are specified in Table 2.4 where R_s and R_{CT} stand for the electrolyte and charge transfer resistances, respectively. Slight linearity that exists in both EIS plots of NF and NS obliged the inclusion of Warburg element signified as “W” into the circuit. NW-structured films, in contrast, demonstrated a more kinetic-controlled behavior and did not require the presence of W for a perfect fit.

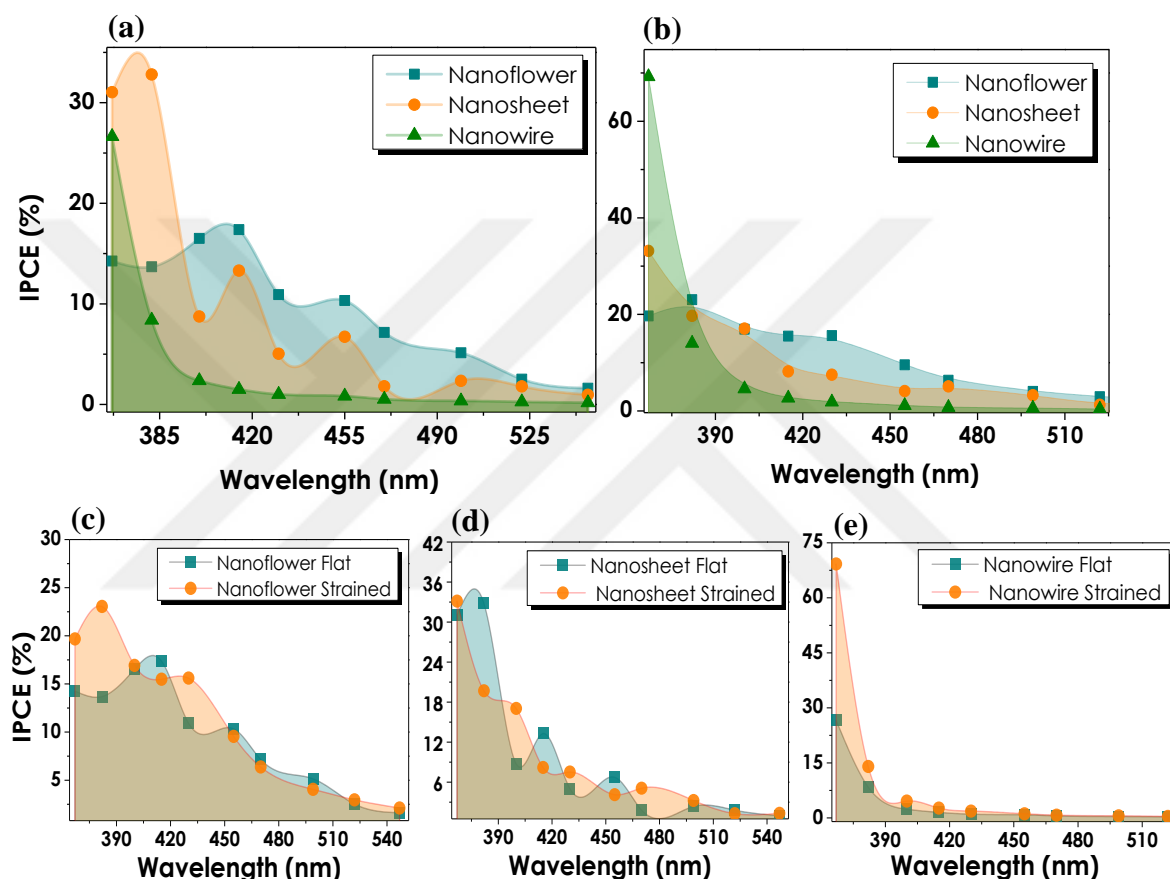


Figure 2.12: %IPCE data obtained for (a) flat and (b) strained ZnO thin films and individual comparison of flat and strained (c) NF, (d) NS, and (e) NW performances.

Interpreting the circuit elements individually, it can be seen that electrolytic resistances are approximate for all three cases. R_{CT} values, however, show substantial differences. Here, NS and NW films have generated resistance in the measure of $k\Omega$, while the charge transfer resistance of 3D NFs was only 40.7Ω . These results rationalize the reason behind the highest photocurrent generation of NF structured thin films.

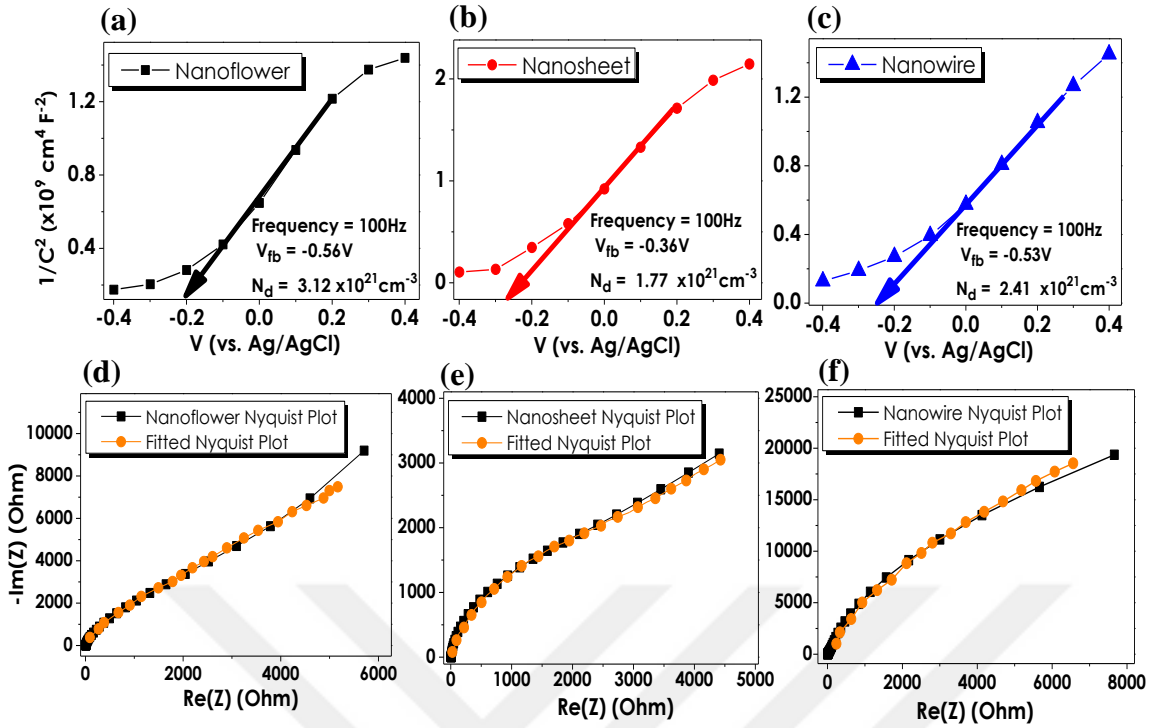


Figure 2.13: Mott-Schottky plots for (a) NF, (b) NS, and (c) NW structures with corresponding evaluated V_{fb} and N_d data. EIS measurements reveal Nyquist plots of (d) NF, (e) NS, and (f) NW.

The repeatability of straining has been measured with consecutive deformations applied on ZnO-deposited SS substrates. These deformations have been implemented manually and each substrate has been flexed to a standard, predetermined radius (Figure 2.2). These deformations have been redone for 10 and 50 cycles and the consequent current density performances have been evaluated. In previous material characterizations, NF and NW films have shown better durability to the act of straining. In a similar manner, during the 10 consecutive straining tests, these aforementioned films have demonstrated an approximate performance. In fact, owing to the better orientation of nanostructures after being strained, a slight increase in J-V performance has been observed. However, a substantial performance fall of ~25% and ~35% in photocurrent generation of NF and NW has been detected under 50 straining cycles, respectively.

Table 2.4: Fitted equivalent circuit models and corresponding values of circuit elements for NF, NS, and NW structured ZnO thin films images.

ZnO Morphologies	Equivalent Circuit	Circuit Elements				
Nanoflower		$R_s (\Omega)$	$R_{ct} (\Omega)$	CPE ($\mu F.s^{(a-1)}$)	a	W ($\Omega.s^{-0.5}$)
		7.2	40.7	45.2	0.9	6500
Nanosheet		$R_s (\Omega)$	$R_{ct} (\Omega)$	CPE ($\mu F.s^{(a-1)}$)	a	W ($\Omega.s^{-0.5}$)
		5.7	3200	79.5	0.8	1900
Nanowire		$R_s (\Omega)$	$R_{ct} (\Omega)$	CPE ($\mu F.s^{(a-1)}$)	a	
		4.1	61×10^3	62.3	0.9	

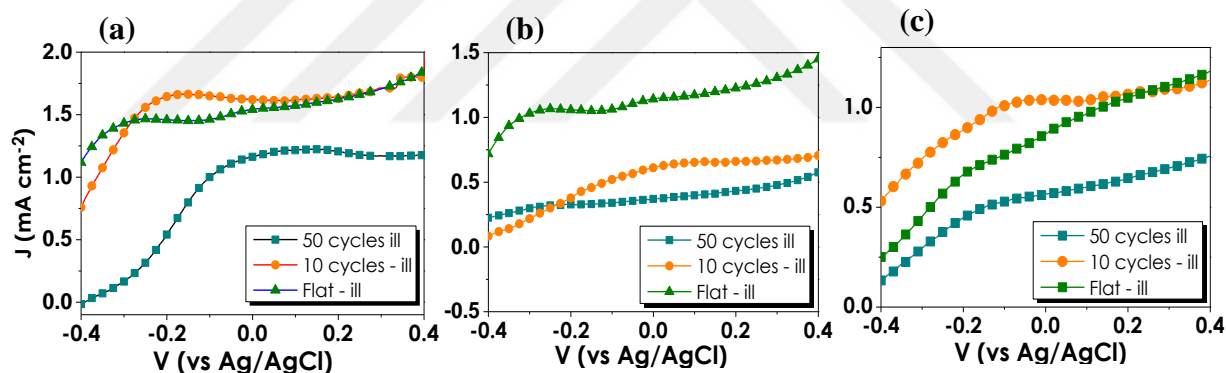


Figure 2.14: Current density performances of intact, 10 and 50-times strained thin films obtained under potential sweep for (a) NF, (b) NS and (c) NW, respectively.

A completely different scenario has been observed for NS-structured thin films, where no durability towards straining has been observed. The durability limits of ZnO thin films have been pushed by increasing the number of straining cycles and are summarized in Table 2.5. As can be seen from the obtained table, NS-structured films completely delaminate from the surface and generate a near-zero current at 100 cycles. NF films endure 100 straining cycles but are not observed to be durable till 500 sets. NWs, on the other hand, have shown the highest endurance and

generated an almost constant performance of $0.41 \text{ mA}\cdot\text{cm}^{-2}$ for 2000 consecutive straining sets.

Table 2.5: Summary of photocurrent densities of ZnO electrodes at $0 \text{ V}_{\text{bias}}$ (vs. Ag/AgCl) after consecutive straining cycles

ZnO thin film Morphologies	J ($\text{mA}\cdot\text{cm}^{-2}$)					
	Flat	10 cycles	50 cycles	100 cycles	500 cycles	2000 cycles
Nanoflower	1.54	1.62	1.16	0.29	-	-
Nanosheet	1.14	0.61	0.37	-	-	-
Nanowire	0.87	1.04	0.57	0.57	0.45	0.41

2.4 Conclusions

In conclusion, this chapter of the dissertation has comprised the deposition of 3D nanoflower, nanosheet, and 1D nanowire structures on flexible SS substrates aiming for their future implementation as curved photoanodes in PEC water splitting systems. Basic material characterizations analyzing the morphology, crystallinity, elemental composition, and defect content of each nanostructure have been individually conducted and the differences between strained and unstrained thin films have been established. Water splitting performance evaluations have culminated in results showing NF superiority among flat photoelectrodes. Moreover, a comparatively higher responsivity obtained for the aforementioned films ($6 \text{ mA}\cdot\text{W}^{-1}$) has been obtained subsequent to 10 cycles of consecutive illumination and darkening sets, validating a more stable and durable nature of NFs. The generation of better photocurrent densities has been attributed to a more oxygen vacant nature of nanoflower-shaped ZnOs that has been validated by expressive spectroscopic techniques like XPS, EDAX, PL, and Raman. In addition to these analyses, EIS measurements have also revealed a much smaller charge transfer resistance at the electrode/electrolyte interface which rationalizes the supremacy of NFs over other nanostructures in their flat forms.

Strained photoelectrodes, on the other hand, have shown major morphological variations. At this stage, NS photoelectrodes displayed a significantly poor surface adhesion and have delaminated from the surface. Conversely, NF and NW-structured thin films have blossomed into more revealed and explicit nanoformations resulting in better light-capturing performance. NW has dominated the UV-range IPCE performances by generating an efficiency of 69%. Based on our thorough literature reviews, we can confidently state that this efficiency is amongst the highest ones reached for a pristine ZnO photoanode.



CHAPTER 3

3. CONTROLLING PHOTOLUMINESCENCE OF MULTI MORPHOLOGICALLY GROWN ZnO NANOSTRUCTURES PATTERNED VIA NANOSECOND LASER ABLATION

3.1 Introduction

Zinc oxide (ZnO) is found as a prominent material due to its numerous idiosyncratic features, thus, playing an important role in a wide range of implementation areas extending from biological sciences to energy applications. As the starring material of this thesis work, ZnO has been primarily incorporated into solar-driven water-splitting systems as the photoanode material in Chapter 2. The suitable band edge positions of ZnO (with respect to H₂O redox potential) provided the necessary potential for the successful water reduction process and have been implemented into PEC systems in form of flexible photoanodes owing to bendable stainless steel foil substrates. Detailed material and performance characterizations have been conducted and broad investigations have been done to better understand the ultimate effect of straining on photoelectrochemical efficiencies. The current section of this dissertation shifts the focus from PEC application and performances of ZnO nanostructured thin films and sets sight on a more distinctive application area – optoelectronics. It was the period of late 1990s when the scope of ZnO applications has been extended into optoelectronic devices for being used as light-emitting diodes (LEDs) and laser diodes due to their highly suitable characteristic material properties such as direct band gap, large exciton binding energy, resistance to radiation and thermal/chemical stability in ambient conditions [49]. Studies investigating the photoluminescence abilities of ZnO report the presence of emissions in blue and UV regions matching the band gap of the given semiconductor. In addition to this, ZnO possesses large numbers of defects and impurities in its structure varying according to the synthesis and growth conditions. These extrinsic and intrinsic defects cause the emission of light in different colors that are generated by inner trap states. Moreover, the band gap engineering availability of this material provides the formation of quantum wells

and barrier layers with the aid of tiny lattice mismatches which induces different emission mechanisms, as well [50]. The given part of this thesis work focuses on the exploration of luminescent properties of nanorod (NR) and nanoflake (NFI) structured ZnO thin films and the variation in their near band edge (NBE) emissions as a result of simultaneous and patterned growth on the same substrate. Moreover, this section uncovers a brand new, straightforward, and rapid technique of patterning via nanosecond (ns) fiber laser ablation process that provides the aforementioned patterned and selective NR/NFI growth.

3.1.1 Photoluminescence phenomenon

Solid materials exhibit luminescent behavior when an external source acts as a driving force for the excitation of electronic states and further gets released in form of light [51]. The phenomenon can be specified as “photoluminescence” (PL) when the released energy lies within the short-wavelength range (i.e. UV-visible). PL, in itself, can be classified into two main categories which are (i) intrinsic and (ii) extrinsic luminescence. Intrinsic photoluminescence, on the other hand, can also be categorized into three kinds denoted as;

- **Band-to-band luminescence:** Luminescence is generated as a result of recombination of electrons in the conduction band with holes in the valence band. This type of luminescence is reported to be mostly encountered in pure materials due to the absence of trap states in the mid-gap energy levels.
- **Excitonic luminescence:** Luminescence originating from excitons, composite particles consisting of an excited electron and a hole, holding on together via Coulombic interactions.
- **Cross-luminescence:** A specific type of luminescence being produced by recombination of an unexcited electron in the valence band with hole in the outer core band that has been primarily encountered in BaF₂ in 1982 as a result of x-ray pulse interaction. At the moment, these types of luminescence can be observed for various kinds of alkali halides, as well.

On the other hand, extrinsic luminescence originates from the intentional incorporation of defects and impurities [51]. These types of impurities act as activators causing non-NBE emissions to occur and are also categorized into (i) unlocalized and (ii) localized types. Unlocalized luminescence is caused by the

charge carriers of the host lattice, where most commonly encountered impurities, donors and acceptors, play the role of luminescence activators. In the contrary, in localized luminescence, the emission takes place in luminescence centers.

3.1.2 Photoluminescence properties of zinc oxide

ZnO crystals having sizes ranging from a few centimeters to nanometers commonly exhibit a similar luminescence behavior with two emission bands of which; (i) short-wavelength emission, denoted as near-band-edge emission (NBE), appears in the UV region and corresponds to typical band gap transition and (ii) broad band long-wavelength emission generating as a result of deep-level trap states caused by impurities and defects within the ZnO structure [11,52,53]. The reason for the long-wavelength emissions appearing broad and covering almost the entire visible spectrum lies behind the fact that different types of deep level emissions gather together and superpose at the same time. The origin of the mentioned deep level emissions is numerous types of defects existing in ZnO crystal lattice with their significant formation energies and different contributions to material properties [11]. It is important to note that these defects are mostly known to be as oxygen vacancies (V_o), oxygen interstitials (O_i), zinc vacancies (V_{Zn}) and interstitials (Zn_i), oxygen and zinc antisites (O_{Zn} and Zn_o) and correspond to intrinsic or native defect types. Although these intrinsic defects are suggested as commonly encountered ones in ZnO structures, the mechanism responsible for visible emissions generated by them is still a matter of debate. Recombination of electrons in the conduction band with holes in deep trapped states or recombination of holes in valence band with deep-trapped electrons are the two possible scenarios suggested for the explanation of the rationale behind visible broad band emissions [52]. Nevertheless, conducted studies prove that the defect-related emissions of ZnO can occur within the entire visible range exposing various colors due to distinct defect configurations which are briefly summarized in Table 3.1. This color divergence proves the white light-emitting potential of ZnO-based diodes under suitable circumstances and varying growth conditions. In other words, constituting a blended system containing ZnO nanostructures with different defect densities can act as a helpful tool in order to obtain a composite photoluminescence response emitting an eventual white light. In this regard, the given part of this thesis work focuses on the simultaneous single step CBD growth of multi-morphological ZnO

thin films containing nanorod (NR) and nanoflake (NFI) structures possessing completely different defect contents and therefore generating disparate PL emissions.

Table 3.1: Deep level defects in ZnO nanostructures causing different color emissions

Emitted color from ZnO	Possible deep level transition	Ref.
Violet	$Zn_i \rightarrow$ Valence Band	[54]
Blue	$Zn_i \rightarrow V_{Zn}$ Conduction Band $\rightarrow V_{Zn}$	[54,55]
Green	Conduction Band $\rightarrow V_o/V_{Zn}$	[56–58]
Yellow	Conduction Band $\rightarrow O_i$	[59]
Orange	Conduction Band $\rightarrow O_i$ $Zn_i \rightarrow O_i$	[53,54]
Red	Lattice mismatch along c-axis (Zn_i)	[60]

3.1.3 Nanoscaled patterning techniques

Patterning is a recognized technique used for the synthesis and growth of arranged hybrid nanostructures in pre-established regions. For decades, patterned nanostructures and nanodevices have found implementation in a broad range of application fields such as electronics, photonics, optoelectronics, and sensors [61–64]. Lithography, known to be the pioneering technology of patterning, works based on the pattern formation principle with precisely arranged feature sizes ranging from nm to mm scales. Being categorized into masked and maskless lithography, both methods are highly prevalent and preferred. The former method uses a large variety of molds and masks in order to apply the predetermined pattern. Photolithography, nano-imprint lithography, and soft lithography are among the most commonly known masked lithographic techniques. In the contrary, maskless lithography such as e-beam or focused ion beam lithography does not require any pre-prepared mask where patterning is actualized via serial writing via a much higher resolution. Although the

lithographic methods are highly common and precise, the limitations in their utilization still exist. For instance, masked lithography requires the preparation of masks prior to deposition which is ineffectual in both temporal and economic aspects. On the other hand, maskless lithography has low throughputs due to the slow nature of serial writings and requires sophisticated equipment which hinders its implementation [65]. At the moment, low-cost, time-saving, rapid and straightforward patterning techniques are in high demand pushing forward the scientific explorations in this field. This situation puts an emphasis on the development of alternative and more innovative methods. Laser ablation, being a revolutionary technique in thin-film processing, evolved as an alternate method of patterning where an optically shaped and homogenized laser beam is directed on a substrate to fulfill the selective etching of the desired layer or material [66,67]. In respect to this, the given part of this thesis work focuses on nanosecond (NS) fiber laser as a simple yet effective patterning tool in order to perform a specific type of ablation providing an eventual multi-morphological ZnO growth.

3.1.4 Nanosecond fiber laser ablation as a successful tool for patterning

Monochromatic beam generation, high beam intensity, availability of small-sized feature formation are some of the numerous unique features of laser processing that have turned it into a highly demanded patterning tool for the last few decades [68]. Especially, considering the thin film production and processing techniques, the ability to scribe the layers in a controlled manner till the required depths and to guide the beam in a pre-determined pattern, are among the reasons for the laser ablation technique being incorporated into nanotechnological applications [69,70]. Fiber laser systems are able to apply a single laser pulse in a time scale ranging from nano to femtoseconds. Nanosecond (ns) fiber lasers being ideally suitable for marking, machining and scribing applications possess several drawbacks in contrast to their counterparts due to longer pulse durations. Considering specifically metal thin films that conduct heat in sub-picosecond rates, ns fiber laser systems cause melting or undesired/uncontrolled scribing outcomes. Nevertheless, finding their place in industrial application fields, ns fiber laser systems are utilized in many research fields some of which are solar cells, display, sensors, thin-film applications and so on. The given part of this thesis work takes into consideration all the pros and cons of ns fiber laser scribing and utilizes it for selective Ti thin-film ablation under low fluence energy

values. In addition, the study also utilizes the over-scribing performance of ns laser system at higher fluences for selective removal of the whole film in order to provide multi-morphological growth of 1-2D ZnO nanostructures.

3.1.5 Role of ZnO in optoelectronic applications

To date, ZnO implementation has been encountered in a large number of optical/electrical areas such as transducers, light-emitting diodes (LEDs), sensors, and so on. UV sensitivity of this material has turned it into a manifesting candidate for short-wavelength range sensor applications [71]. Its transparent nature, band gap engineering ability, and controllable growth conditions that result in various nanostructures are some of the important properties that provide versatility in the developed optoelectronic systems [72]. Among the countless numbers of studies implementing ZnO into optical devices, basic 1D nanostructures such as nanowires and nanorods are the most commonly encountered ones. The cultivation of ZnO nanorods/nanowires on GaN LEDs is a highly common technique used in order to improve the light-harvesting efficiency via surface area enlargement [71]. Moreover, depending on the growth conditions, various ZnO nanostructures generate defect-originated emissions in the visible region turning them into suitable candidates for solo LED fabrications. Homo and heterojunction LEDs, laser diodes, and photodetectors incorporating ZnO mostly as in n-type doped form, can also be listed among highly common optoelectronic devices.

3.2. Experimental Methods

Tin-doped indium oxide (ITO) deposited substrates with an average resistivity $<10 \Omega/\square$ have been procured from Teknoma Technological Materials Industrial and Trading Inc. (Izmir, Turkey). Sputtering has been conducted via ZnO (99.99%) and Ti (99.99%) targets from Plasmaterials, Inc. (California, USA). Zinc chloride (ZnCl_2) as zinc source and Hexamethylene tetramine ($\text{C}_6\text{H}_{12}\text{N}_4$) as reaction precursor have been purchased from Sigma Aldrich (Schnelldorf, Germany). Purchased chemicals have not been subjected to any additional purification procedure.

3.2.1 Preparation of substrates

Multilayered thin films consecutively consisting of ZnO and Ti have been grown on ITO-deposited glass substrates. ZnO and Ti are two seeding layers that possess completely different characteristics in the sense of ZnO nanostructure growth. As a dimensionless seeding layer, ZnO plays the role of growth accelerant for nanostructured ZnO formation via CBD. Ti, on the other hand, inhibits the nucleation and upgrowth stages of ZnO. These two thin films have been combined on a single substrate in order to provide controlled growth of ZnO in a predetermined pattern. This has been maintained via a nanosecond (NS) fiber laser that was used to scribe the upper Ti layer in a delicate manner. At this stage, it is important to point out that both ZnO and Ti thin film layers have been deposited via RF magnetron sputtering technique under ultra-high vacuum (UHV) conditions and pure Ar environment. Deposition of primary ZnO layer has been followed by annealing at 300 °C in RTA furnace under vacuum. This step has been performed in order to ensure a homogeneous deposition of the ensuing Ti layer. At the final stage, the Ti layer has been deposited under 100W sputtering power. This step has been maintained for 16 minutes in a UHV chamber under an Ar atmosphere. The thin film preparation steps have been visualized in Figure 3.1.

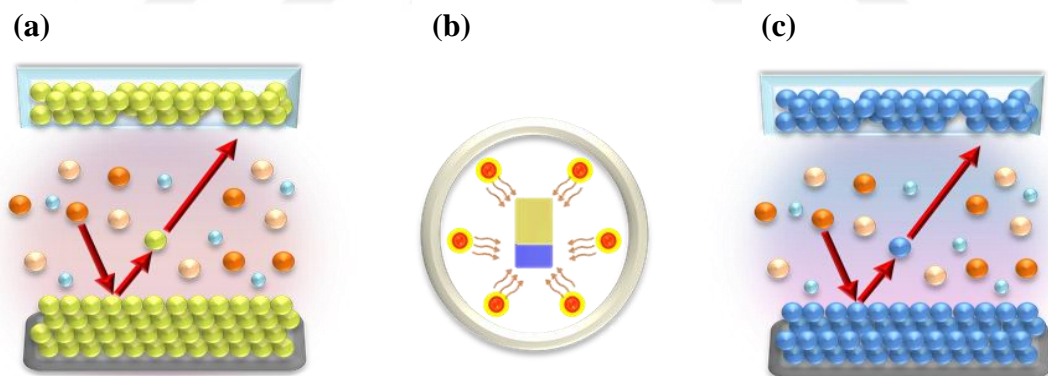


Figure 3.1: Consecutive steps of (a) ZnO deposition, (b) rapid high-temperature annealing and (c) Ti deposition for substrate preparation

3.2.2 ns fiber laser ablation process and parameter determination

Ns fiber laser ablation is the most crucial and characteristic step of the whole experimental procedure as it is exactly this step that provides selective and patterned growth of ZnO nanostructures. Table 3.2 summarizes the default parameters of ns fiber

laser device to provide its detailed explanation and Figure 3.2 incrementally describes the thin film ablation and CBD growth steps. A laser beam of 1064nm wavelength, corresponding to IR region, is directed onto the pre-prepared substrate through varying three basic parameters which are power, frequency, and scan rate. The two former mentioned parameters are the ones that directly affect the energy of the incident beam, while the latter one is used to control the distance between the laser spots which changes the intensity of pulse per ablation area. Detailed equations used in laser parameter calculations are specified in Table 3.3. In literature, fluence energy is the most commonly encountered laser parameter that is used for the specification of applied energy. Another important parameter that strongly affects the spot dimensions, homogeneity of the scribed region and thickness of ablated Ti-layer is the “focus”. Hence, this chapter is going to sequentially investigate the (1) effect of focus and (2) fluence energies in order to render a verdict about the most optimal ablation condition for a homogeneous and selective ZnO film growth. After deciding on the most optimal distance of focus, 2 different fluence energies are going to be discussed; (I) 28.43 J.cm^{-2} obtained under 25W, 70 kHz, 5500 mm.s^{-1} and (II) 3.72 J.cm^{-2} generated via 7W, 150kHz and 4500 mm.s^{-1} . The initial, high fluence energy ablation is going to be used in order to ablate the whole film from the surface according to the applied pattern, while the latter one represents more controlled scribing where the depth of the laser beam is trying to be controlled till the ZnO layer.

3.2.3 Characterization techniques

Electron microscopy images of obtained thin films have been captured with QUANTA 400F Field Emission SEM device. The effect of different fluence energies on ablation performance has been analyzed via Nikon Eclipse LV 150N optical microscope. Horiba Jobin-Yvon Florog-550 device has been used for PL measurements. Here, a He:Cd laser with 50 mW excitation power at 325 nm laser irradiation has been applied on ZnO samples. Transient PL analyses have been conducted with Edinburgh Instruments FLS1000 Spectrometer within Koç University Surface Science and Technology Center (KUYTAM).

Table 3.2: Default parameters of nanosecond fiber laser ablation system

Nanosecond Fiber Laser Parameters	
Laser Source	Nd-YAG (Y3AL5012)
Laser Pulse Type	Nanosecond(ns)
Wavelength	1064 nm
Range of Average Power	0.008-25 Watt
Range of Frequency	70-200 kHz
Focal Length	160 mm
Depth of Focus	181 mm
Diameter of Light From Flat(D)	7.5 mm
Correction Factor	1.4 m ²
Pulse Duration	160 ns

Table 3.3: Necessary equations for calculation of ns laser parameters

Parameter	Corresponding Equation
Pulse Energy	$\frac{\text{Average Power(Watt)}}{\text{Frequency(Hz)}} \quad (\text{Eq. 3.1})$
Fluence Energy	$\frac{\text{Pulse Energy(Joule)}}{\text{Area of the Spot Size(cm}^2\text{)}} \quad (\text{Eq. 3.2})$
Peak Power	$\frac{\text{Pulse Energy}}{\text{Pulse Duration(ns)}} \quad (\text{Eq. 3.3})$
Power Density	$\frac{\text{Peak Power}}{\text{Area of Spot Size (cm}^2\text{)}} \quad (\text{Eq. 3.4})$

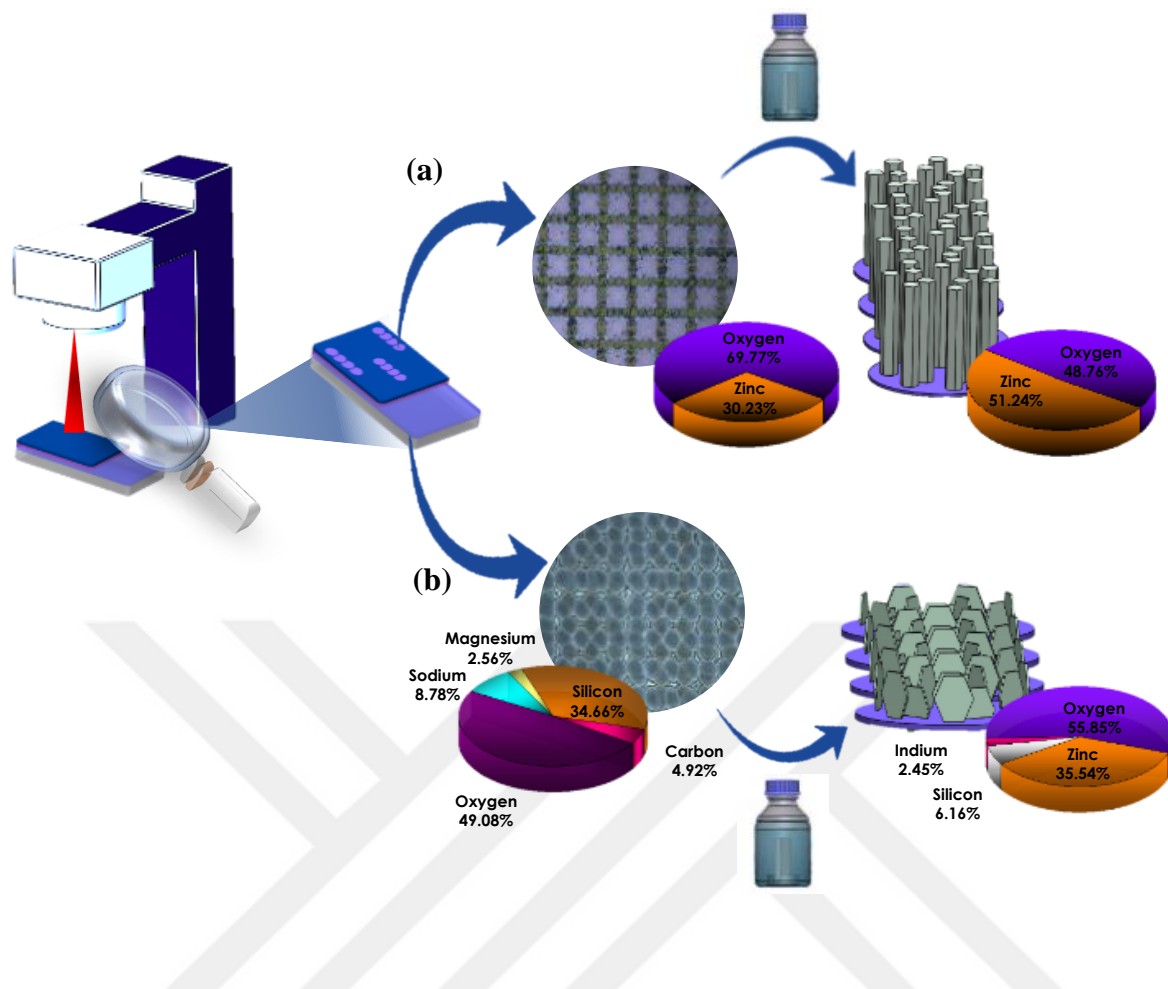


Figure 3.2: Laser ablation steps of Ti/ZnO coated ITO glass substrates under (a) low (3.72 J.cm^{-2}) and (b) high (28.43 J.cm^{-2}) fluence energies with EDAX data collected from laser spots giving a hint about penetration depths of scribing energy followed by exact same CBD steps proceeding each ablation process showing the growth of (a) nanorods (NRs) for and (b) nanoflakes (NFIs)

3.3 Results & Discussion

3.3.1 Growth of two different ZnO nanostructures within the identical CBD solution

Prior to conducting laser-based selective ZnO deposition, the growth of ZnO nanostructures within the same CBD solution on diverse substrates has been tested. Here, the utilization of zinc chloride (ZnCl_2) as Zn source and hexamethylenetetramine (HMTA) as precursor has generated different outcomes on two different substrates. The primary analyzed substrate was ZnO deposited on ITO glass (ITO/ZnO) while the second one was the consecutively deposited and completely scribed ITO/ZnO/Ti films.

Figure 3.3 (a) clearly displays the homogeneous growth of nanorod (NR) formations on the pristine ZnO seeding layer. It is important to note that the ZnO seeding layer has a thickness of 150 nm and NR structures have an average length and diameter of 2.4 μm and 350 nm, respectively. The second substrate at the focus of interest consisted of ZnO/Ti layers deposited on ITO-coated glass via sputtering technique followed with their complete ablation from the surface under 1064 nm ns laser source. The CBD conducted on this check sample resulted in the formation of 2D nanoflake (NFI) formations. As can be seen from Figure 3.3 (b) the distribution of flake structures through the surface is not as dense and homogeneous as 1D NRs. It is important to highlight that Ti layer had a thickness of ~ 110 nm and the ablation conditions for the overall scribing have been set to 25 W and 70 kHz which correspond to $28.4 \text{ J}\cdot\text{cm}^{-2}$.

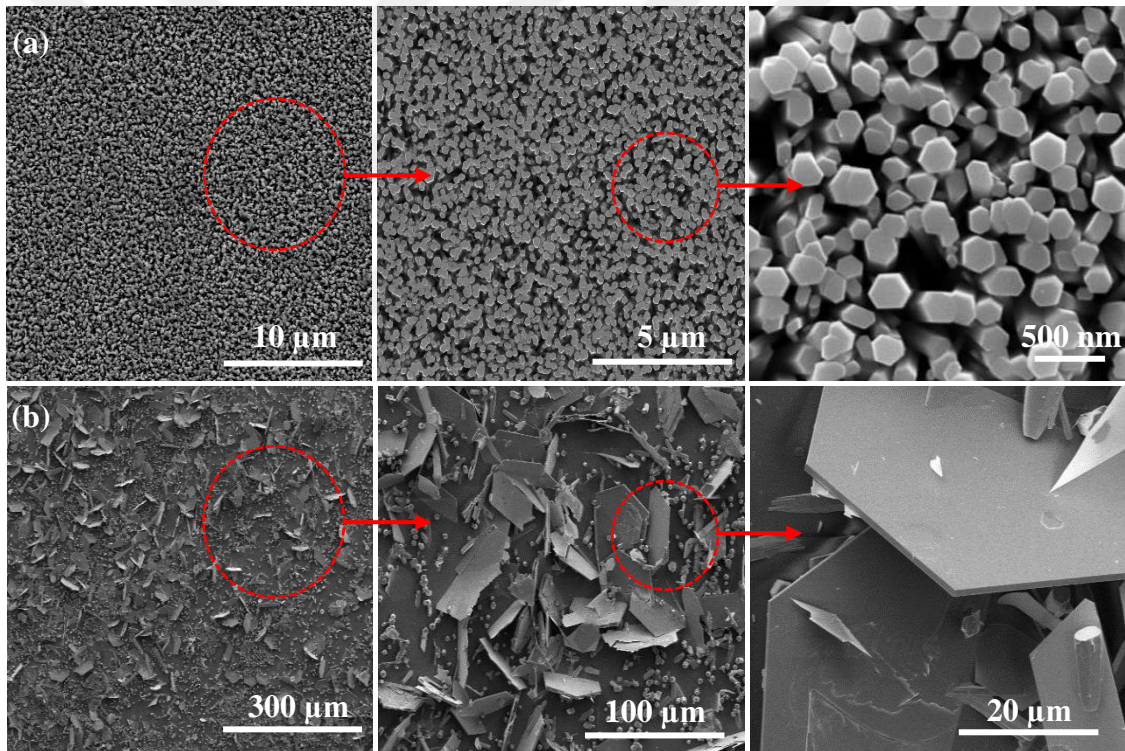


Figure 3.3: Birds eye and zoomed SEM images of (a) unidirectionally oriented ZnO nanorods, demonstrating a uniform film distribution over the substrate surface; (b) nanoflakes, demonstrating a scantly oriented distribution of film on the substrate.

X-ray-based techniques have been applied in order to analyze the crystallinities of obtained nanostructures, investigate their chemical state and coordination environments. Figures 3.4 (a) and (b) demonstrate X-ray diffraction (XRD) data of NR

and NFl structures, individually. Both figures clearly display the wurtzite crystalline structure of ZnO which can be evidenced by the presence of significant [100], [002], and [101] peaks [73]. NRs, which tend to grow in a direction perpendicular to the substrate, generate the sharpest peak in [002] diffraction plane. The comparatively low peak intensities obtained from NFl-structured films can be correlated with their nonhomogeneous and relatively bald dispersion along the surface. It is also important to highlight that a significant bump around smaller 2Θ arises due to the revealing presence of soda-lime glass [74].

X-ray absorption spectroscopy (XAS) served for the electronic structure investigation of both thin films. X-ray Absorption Fine Structure Spectroscopy (XAFS) results that are explicitly given in Figure 3.4 (c) have been divided into two units that separately investigate two different material characteristics. The first unit known as X-ray absorption near edge structure (XANES) informs us about the coordination environment of the element by identifying its charge and bonding state. The second unit, also known as extended XAFS or EXAFS, helps in understanding the local atomic arrangements uncovering information about bond lengths and coordination numbers [75]. Analyzing the inset in the overall XAFS spectra in Figure 3.4 (c), triple labeling can be observed. This labeling signifies the $1s \rightarrow 4p$ electronic excitation [76,77]. Moreover, from the differences in region B, it can be observed that NFls generate a higher normalized electric field under applied energy. A tiny deviation in B regions is considered as a necessary point to be commented on. It is known that NRs absorb irradiation with their (0001) surfaces which have an average radius of 175 nm. NFls, on the other hand, have a random inclination throughout the surface and therefore absorb light with both facets of a few microns. These variations in absorption planes and sizes of susceptible surfaces cause distinguishable shifts in the XAFS spectra.

EXAFS data has been acquired via modification of XAFS spectra by using ATHENA-ARTEMIS programs. In addition, the obtained data has been processed through Fourier transformation for easy interpretation. Both spectra are clearly displayed in Figures 3.4 (d) and (e). Analyzing Figure 3.4 (e), significant peaks at around 1.5 and 2.9 Å radial distances can be observed. These peaks signify the presence of 4 oxygen atoms bounding the central Zn atom and external coordination shells generated among 12 adjacent Zn atoms, respectively [77–79]. The primary Zn-O peak shows a slightly

distinguishable shift demonstrating a $\sim 1.47\text{\AA}$ bond length for NR and $\sim 1.50\text{\AA}$ bond length for NFI. Moreover, an appreciable variation in peak intensity appears to be more intense for NFI formations. The second peak, which has been attributed to Zn-Zn bond length, also shows distinctions between the two structures. Here, the distance between 2 Zn atoms appears to be 0.1\AA longer for NFIs. It is important to note that the main focus is made on outer coordination shells due to the information those bond lengths possess. In other saying, shifts observed in significant Zn-Zn bond lengths can be directly correlated with changes in morphology and therefore, can elucidate the local electronic arrangements.

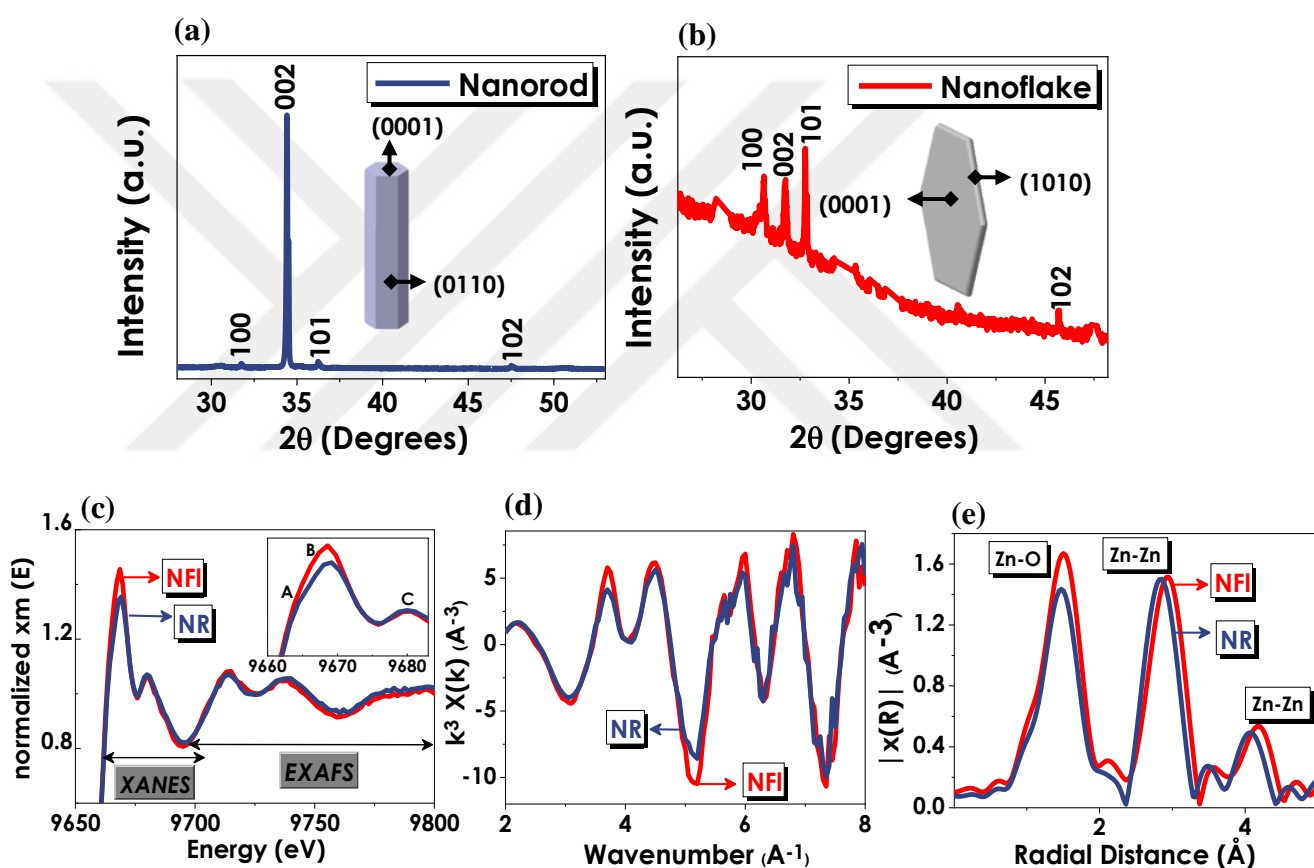


Figure 3.4: XRD responses of wurtzite (a) NR and (b) NFI with insets representing rod-like and hexagonal flake-like structures; XAS responses with their detailed (c) XAFS, (d) XANES and (e) EXAFS elaborations.

The light absorption performance of nanostructured ZnO films has been analyzed through UV/Vis optical characterization technique. It can be clearly seen from Figure 3.5 (a) that the uniform film formation of NRs strongly contributes to their light

absorption performance, especially at $\lambda < 400\text{nm}$ within the overall 350 – 500nm range of observation. NFIs, on the other hand, demonstrate comparatively lower absorption through the aforementioned region but tend to remain almost intact within the measurement range. The obtained absorption data did not only serve for understanding the UV/Vis susceptibility range of nanostructures but also contributed to the evaluation of individual ZnO band gaps (E_g). Figure 3.5 (b) demonstrates the estimated Tauc plots where the x-intercept of the linear section of the graph infers E_g . Here, a significant linearity can be observed below the band gap region which is considered to be originated from transitions at interface state [80]. In other words, presence of various defects cause a linearity shift in Tauc plots and are referred to as “Urbach tail”. Since real materials commonly possess defects and impurities, sub-gap absorptions are considered to be highly effective and therefore, deviate the absorption data. Hence, in Figure 3.5 (b), Urbach energy has been calculated from the absorption spectrum by the following equation 3.5.

$$\alpha = \alpha_0 \exp\left(\frac{E}{E_u}\right) \quad (\text{Eq. 3.5})$$

Here α and α_0 are absorption coefficient and constant, consecutively. E and E_u , on the other hand, represent photon and Urbach energies, respectively. Consequently, from the $\ln\alpha$ vs. E (eV) plot the $1/\text{slope}$ is going to give the Urbach energy which in case of ZnO NFs correspond to 1.28 eV.

Photoluminescent characteristics of NR and NFIs are demonstrated in Figure 3.5 (c). Under 325nm He:Cd laser excitation, two nanostructures have generated completely different emission performances. For NRs, the primary peak appearing at 450nm has been assigned to near band edge emissions or NBEs. These NBEs are known to arise due to recombining excitons that originate due to the presence of Coulombic forces between electrons and holes. In another saying, NBEs demonstrate the directly recombined charge carriers that have come to existence by photoexcitation [81]. Here, it is important to emphasize the fact that the appearance of NBEs at $\lambda > 400\text{nm}$ is unusual and can be attributed to the relatively larger band gap of NRs that induce a red-shifted emission. Several studies have also shown that NR/NW structures generate blue-shifted emissions at small and red-shifted emissions at large radii [82]. The second part of PL spectrum demonstrates a highly intense emission within 500 – 780nm range which incorporates the yellow-orange region within. This region

represents the emission caused by defects present in the structure and is known as defect-related broad emissions or DBEs [83–85]. At nanoscale dimensions, multiple numbers of scatterings significantly decrease the intensities of band-edge emissions. That is why in NRs, which absorb irradiation with their (0001) facets, such a strong difference exists between NBE and DBE intensities [86].

NFI formations generate a completely different emission profile with one NBE and two DBE peaks. For NFIs, a different distribution of intrinsic defects can be considered as a reason for a red-shifted NBE. Studies have reported that the surface-to-volume ratio has an obvious impact on defect densities of nanostructures, especially considering that these defects are mostly accumulated on the surface rather than bulk [39,87]. Therefore, varying morphologies are considered among the major reasons for distinct defect contents and need a more precise investigation and interpretation.

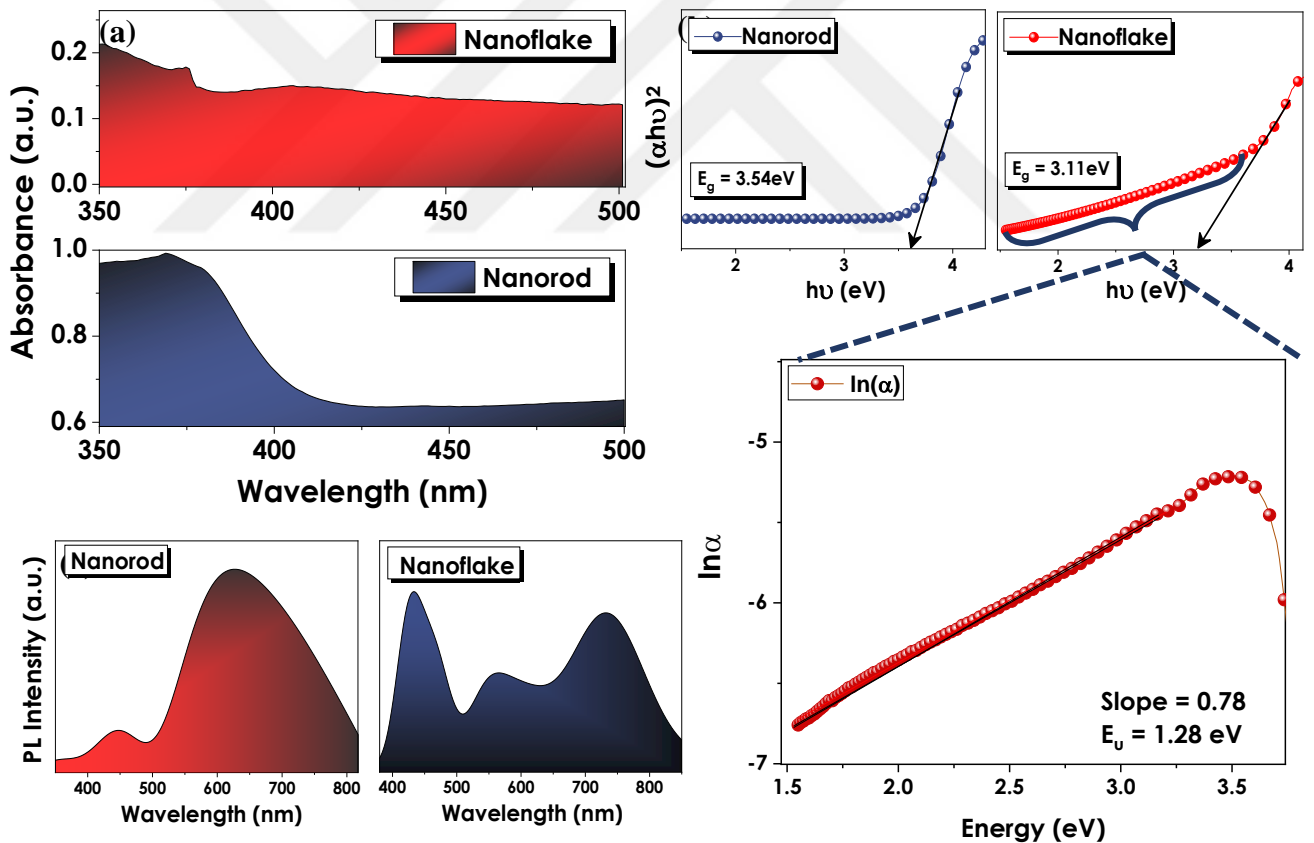


Figure 3.5: (a) Optical absorption data of NFI and NRs together with (b) Tauc plots evaluated by using transmittance data with derived Urbach energy evaluation graph. (c) PL spectra of NR and NFI with a detailed investigation of NBE and DBE regions.

Through deconvolution of the acquired spectra, a more detailed examination of PL emissions has been carried out. As shown in Figures 3.6 (a) and 3.6 (b), emission data of each nanostructure have been fitted into matching Gaussian peaks labeled O₁, O₂, and O₃, respectively. According to these fits, O₁ peaks in both NR and NFl structures occur in the NBE area, which is a form of non-defect associated emission. Nevertheless, the O₂ and O₃ peaks in the visible and near-infrared areas are all separate examples of defect-related emissions in ZnO nanostructures. The O₂ and O₃ deconvolution peaks of NRs exhibit yellow-orange and red emissions, respectively. Luminescence at ~590nm, which signifies the yellow-orange region, is a typical occurrence, particularly encountered in hydrothermally produced ZnO nanostructures with the presence of HMTA as a precursor [39]. Studies report this type of emission being caused by oxygen interstitials (O_i) within the ZnO lattice, thus showing that the origin of yellow luminescence is a bulk rather than a surface defect. Moreover, the large ratio existing between yellow-orange emission and NBE peak bespeaks for the large numbers of defects in as-grown NRs [88,89]. The second emission observed within the red wavelength region is reported to stand for the zinc interstitial (Zn_i) originated lattice disorders throughout the bodies of NRs [39,60].

Gaussian peaks with identical intensities may be seen in the deconvolution spectra of NFls. The increased surface area of NFls is responsible for the higher emission of NBE peak in the UV region [39]. The primal defect-originated peak emerges at 570nm, which is within the yellow emission spectrum in the structure and indicates O_i. The second deconvolution produced at 730nm contains is a rarely encountered situation that is specific to NFl's PL spectra. This emission is in the near-infrared (NIR) region, which has been researched by a number of research teams, although the exact source of luminescence has yet to be determined. Wang et al. offered the most direct approach, in which the creation of NIR emission was linked to the presence of O_i states [90]. The radiative recombination of shallow trapped electrons with deeply trapped holes at O_i is thought to be the source of NIR emission.

Time-resolved PL or TrPL has been implemented as a fortiori technique to clarify charge extraction and recombination processes of ZnOs. This analysis also aimed to associate charge generation and coupling mechanisms with the defect contents of nanostructures. Defect-based transient PL emissions of NR and NFl have been given

in Figures 3.6 (d) – (f). Each data has been acquired under 344 nm picosecond laser source and figures are accompanied with their related fits. For ZnO NRs that possessed a single DBE peak, a double exponential decay fit has been applied. In other words, the luminescence decay data has been disintegrated into two major lifetime components. It can be seen from Figure 3.6 (d) that the intensity of emission reaches its peak point at ~ 6.5 ns period. The decay, on the other hand, must be analyzed from two aspects of two fitted components. The primary decay, which goes by τ_1 in Table 3.4, corresponds to 4.52 ns. Liu et al. have correlated this kind of fast recombination with non-radiative excitonic emissions generated by either surface or deep-buried defects [91]. The relatively much slower decay component denoted as τ_2 has been evaluated as 53.33 ns. This kind of slow recombination is mostly attributed to trap-originated emissions that take place in the bulk of the ZnO crystalline structure.

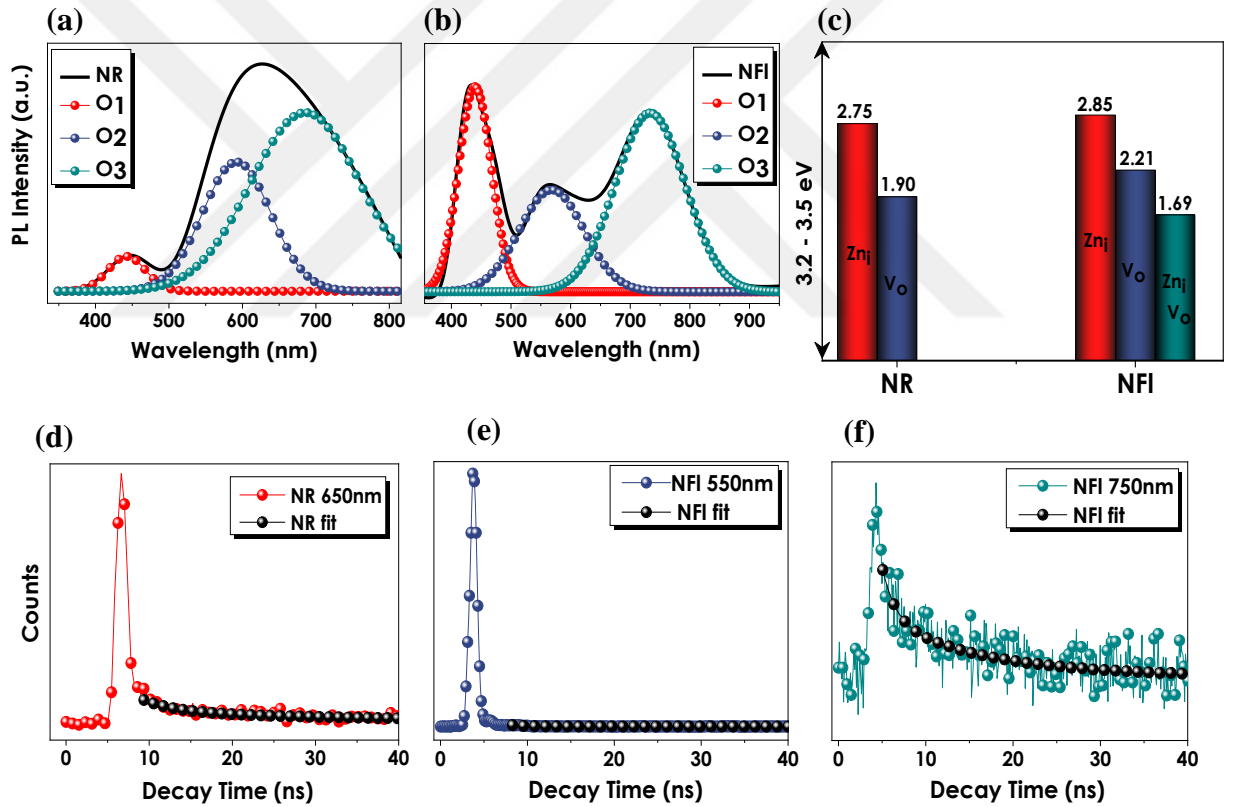


Figure 3.6: Gaussian deconvolutions of the individual (a) NR and (b) NFI luminescence spectra. (c) Schematic representation of defect distribution within both nanostructures. TrPL responses obtained from DBE emissions of (d) NR and (e)-(f) NFI.

Table 3. 4: Minority charge carrier lifetimes of NR and NFl thin films obtained at DBE wavelengths via TrPL analysis.

ZnO	$\lambda_{\text{collection}}$ (nm)	τ_1 (ns)	τ_2 (ns)	τ_{avg} (ns)
NR	650	4.52	53.33	28.92
NFl	550	1.80	N.A.	1.80
NFl	750	1.51	11.90	6.71

TrPL data for NFl-structured thin films have been acquired at two different emission wavelengths. These λ values have been decided based on the PL emission responses and have been selected as 550 and 750nm. Here, both emission wavelengths have reached their maximum intensity within ~ 4 ns. The emission wavelength of 550nm displays a very fast, single-exponential decay within 1.80ns. This emission at 550 nm which corresponds to the yellow region is known to be generated by O_i . The second DBE-related emission that occurs in the near-infrared (NIR) range is generated due to radiatively recombining shallow electrons and deep holes that are originated from the presence O_i defects. The fact that the single-exponential decay of NFl at 550nm and the initial decay component of 750nm have nearly identical recombination lifetimes might pertain to the recombination of electrons with mid-gap energy states created by O_i . In the meantime, the slower recombination component of 750nm emission might also be caused by O_i whilst here indirect recombination of deeply settled defects generating shallow electrons and deep holes are the main cause.

In order to study the absorption process of ZnO NR and NFls, Lumerical FDTD software has been used as a fortiori computer-based simulation approach to conduct a finite-difference time-domain (FDTD) simulation. The goal was to create and mimic the absorption behavior of homogeneous NR and sprinkled and discontinuous NFl films, as well as to associate the experimental results with them. The refractive index employed in the simulations has been imported from prior work [92]. At this stage, physical parameters of NR have been assigned as 2400nm length and 175nm average radius. For NFl simulations, however, an average thickness of 240nm and length ranging from 6000 to 120000nm have been defined as required dimensionalities. Previously demonstrated SEM images have proven that NFls have randomly

distributed inclinations throughout the substrate. That's why simulations have been carried out by changing the angle between NFI and substrate in between 45° and -45° .

It's also worth pointing out that in NR-related simulations, ITO/ZnO thicknesses have been consecutively defined as 100nm and 150nm. For NFIs, on the other hand, as a consequence of laser scribing, the absence of ITO/ZnO has been considered. As a result, for the optical simulation of NFI structure, pristine soda-lime glass has been assigned as the substrate. Simulations have been carried out for three different wavelengths which are; 350, 400, and 450nm. Analyzing Figures 3.7 (a) and (b), it can be concluded that high energetic waves (350nm) are immediately absorbed as soon as they hit nanostructures' surfaces. In NRs, the given figures represent both the propagation of light in the direction perpendicular to the substrate and along the radius (inset). At 400 and 450nm wavelengths, on the other hand, the energy of waves is not high enough to be consumed on the top layer. Therefore, a deeper propagation in the c-axis has been monitored for NR formations. For NFIs, on the other hand, owing to a significantly larger band gap, almost no variation in absorption performance has been observed at 400nm. Simulations generated under applied wavelength of 450nm show that at this energy waves are not strong enough to excite the electrons of NFIs from the valence to conduction band and therefore expand deeper into the structure. The numerical representation of simulation data is summarized in Figures 3.7 (c) and (d). Both nanostructured films show a significantly better optical performance within the UV range and are followed by a decrease towards the visible region. In these aforementioned figures, an obvious comparison is established between experimental and numerical data demonstrating strong compatibility in-between.

Under UHV and 254nm UV irradiance, transient photocurrent spectroscopy (TPS) was used to investigate the photoresponsive properties of ZnO NR and NFI films. Before the experiments, materials were exposed to 10⁻⁶ mbar negative pressure and high energy irradiation to eliminate air adsorbates. Ozdogan et al. previously demonstrated that surface-physisorbed and chemisorbed species have a considerable influence on the TPS outcomes [93]. As a result, it has been established that UHV by itself is insufficient for the complete elimination of adsorbates and that a reliable TPS result can only be achieved when a high energetic source such as UV radiation, is used. To examine the relaxation stage, the UV irradiance was kept at "ON" position for 12ks and then switched to "OFF" position for another 12ks. Figure 3.7 (e) illustrates that

NRs have predominantly displayed an intense current rise under “ON” owing to the formation of electron-hole pairs, followed by a comparatively slower current propagation which is the result of desorption of adsorbed species. During the 12ks “OFF” timeframe, a steady degradation trend can be seen for ZnO NR and NFI. The absence of adsorbates such as oxygen or water under UHV was seen as a consequence that restrained the recovery of the initial current values and resulted in tardy decay.

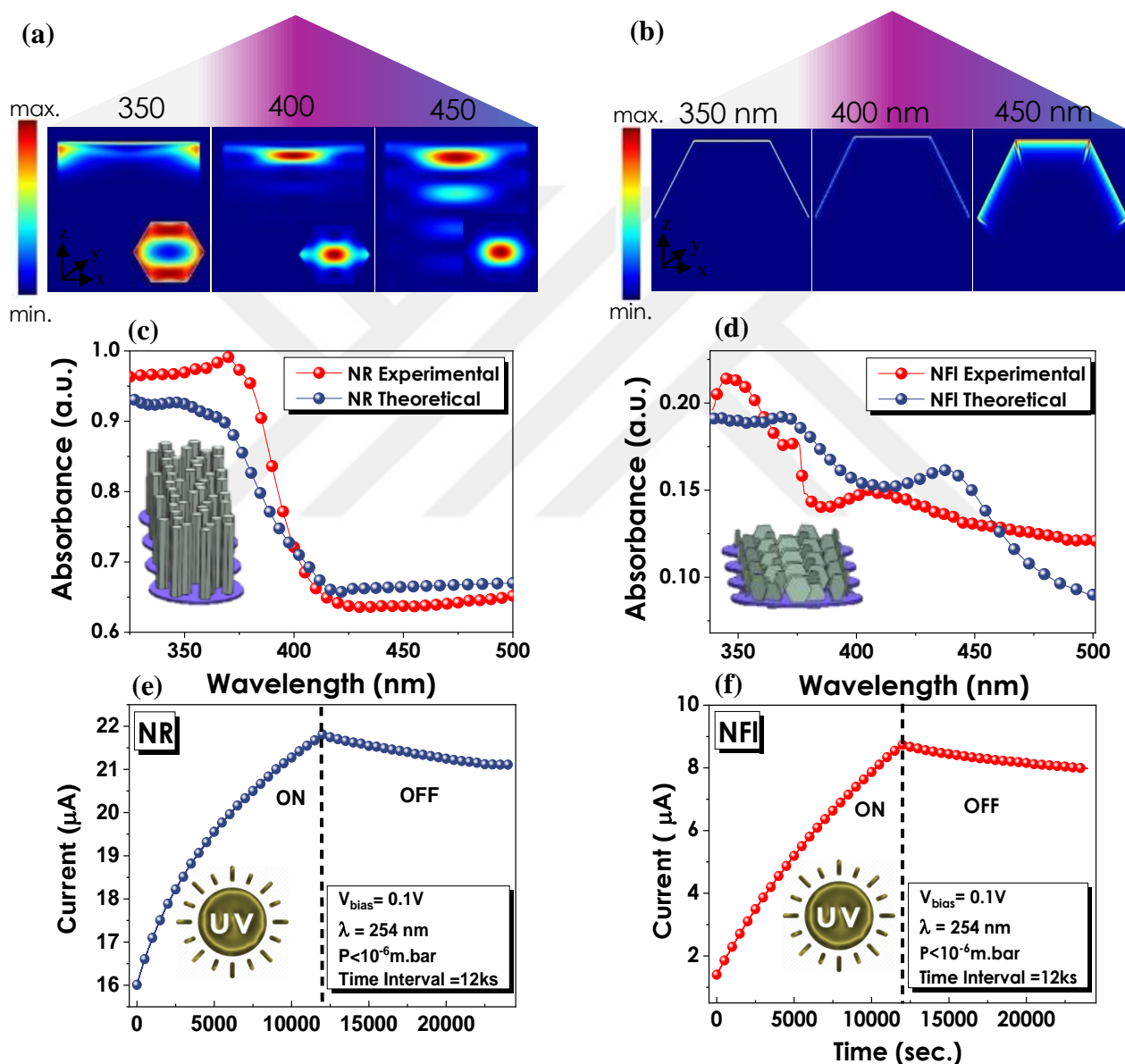


Figure 3.7: Numerical simulation of the distribution of absorbed light within ZnO (a) NR and (b) NFI structures. Comparison between experimental and numerical absorbance responses of (c) NR and (d) NFI-based thin films. TPS data of (e) NR and (f) NFI formations obtained under UHV by consecutively turning UV light on and off.

More specifically, because there are fewer adsorbate species in the analysis environment, dangling surface electrons of ZnO nanostructures remain intact and hence cannot return to their primary current values in 12ks interval. When the TPS responses of NR and NFIs are compared separately, a distinct variation of $\sim 12\mu\text{A}$ can be seen under “ON” conditions. The explanation for this discrepancy may be traced back to the sample's irradiated surface area where in contrast to randomly scattered NFI films, neatly ordered NRs efficiently absorb light, resulting in better current density. Furthermore, NFI structures have demonstrated a relatively better photoresponsivity when focusing on the individual variations between the “ON” and “OFF” performances of both films. Sarkar et al. have reported the variations in TPS responses of ZnO NRs depending on the changing rod diameters [94]. This aforementioned study has shown that finer rods with a larger surface area demonstrate superior photoresponsivity, resulting in quicker reactions to illuminations. The generated photocurrent declines drastically as rod diameter grows from 25-50 to 150 nm, which has been linked to the close pitch structure of NRs restraining the current relaxation. The average diameter of NRs in our study is around 350nm, resulting in an adjacently packed thin film that reduces photoresponsivity. NFIs, on the other hand, have larger spaces in-between providing a faster current relaxation. However, the light absorption capacity is limited by the scattered and inhomogeneous film uniformity.

3.3.2 Laser processing of ZnO thin films

3.3.2.1 Examination of “In-Focus” laser ablated substrates for selective ZnO growth via optical microscopy

Titanium thin film layer plays the role of growth retardant for ZnO nanostructures. Therefore, its patterned presence on a substrate provides the selective growth of ZnO NRs in a predetermined trajectory. For selective removal of Ti layer from the substrate without damaging the ZnO layer beneath it, nanosecond (NS) fiber laser ablation system has been used. 7 W, 4500 mm/s, and 150 kHz has been selected as power, scan rate, and frequency of the ablation step. Under these parameters and based on Eqn. 3.2, the fluence energy of the applied laser beam has been calculated as 3.72 J.cm^{-2} . At the primary stage of the investigation, one additional parameter known as distance-to-focus (DF) has been taken into account. This parameter is expressed as the distance between the stage and the lens of the laser. The approximate distance for an in-focus

ablation of the Ti layer corresponds to 18.2 cm. At this distance, the ns laser applies the necessary fluence energy homogeneously to the substrate selectively scribing only the upper, Ti film. Figure 3.8 (a) shows the progressive photoelectrode preparation steps. The ablation of Ti layer has been conducted in three different predetermined geometric patterns. The first pattern ablates the Ti layer in form of vertical lines which are separated from each other with 0.1 mm (100 μm) only. The other ablation patterns repeat the vertical scribing of Ti layer throughout the film with the only changing parameter being distance between ablated lines. Thus, three different ablation geometries containing vertical lines with 0.1, 0.2, and 0.4 mm separation distances have been prepared via ns fiber laser ablation (Figure 3.8 (b)). Figure 3.8 (c) shows the arranged DF corresponding to the in-focus ablation of the substrate. As a result of correctly adjusted DF value, balanced and homogeneous scribing of Ti has been achieved.

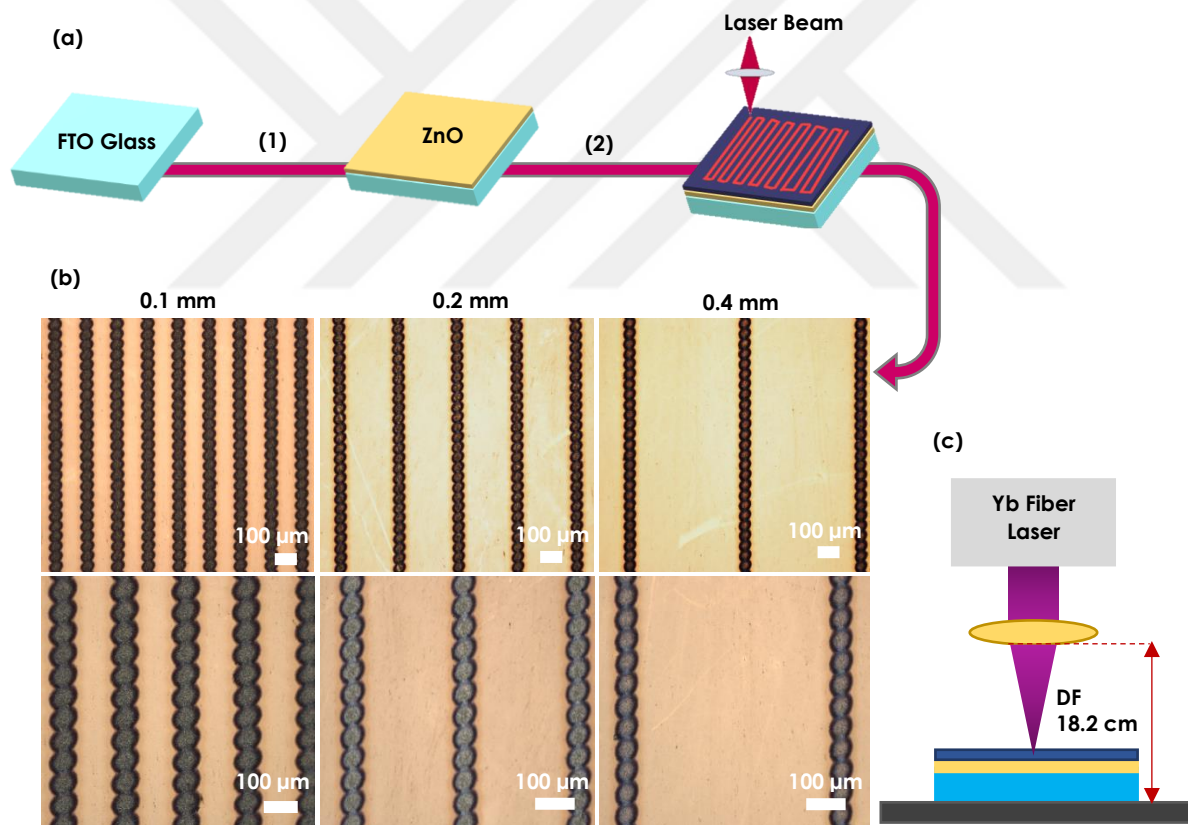


Figure 3.8: (a) Consecutive preparation steps of photoelectrodes. (b) Laser ablation of ZnO/Ti deposited substrates under 3.72 J.cm⁻² fluence energy with three different predetermined patterns. (c) Schematic representation of “in-focus” laser ablation with corresponding DF distance

3.3.2.2. Examination of “Out-of-Focus” laser ablated substrates for selective ZnO growth via optical microscopy

The DF value has been selected as an additional parameter to be modified during laser ablation. Therefore, the effect of slight variation in DF value to the ablation conditions has also been tested (Figure 3.9 (a)). By altering the DF value by only 0.3 cm a significant change in patterns has been observed. Analyzing Figure 3.9 (b), it can be seen that the distances between laser spots have increased generating a different kind of vertical line. Moreover, a slight but significant whitening in the middle of spots gives a clue about a more different distribution of energy throughout the pattern. This distinguishable whitening in the middle of spots has been assigned to the excess ablation which etches the film deeper into the substrate.

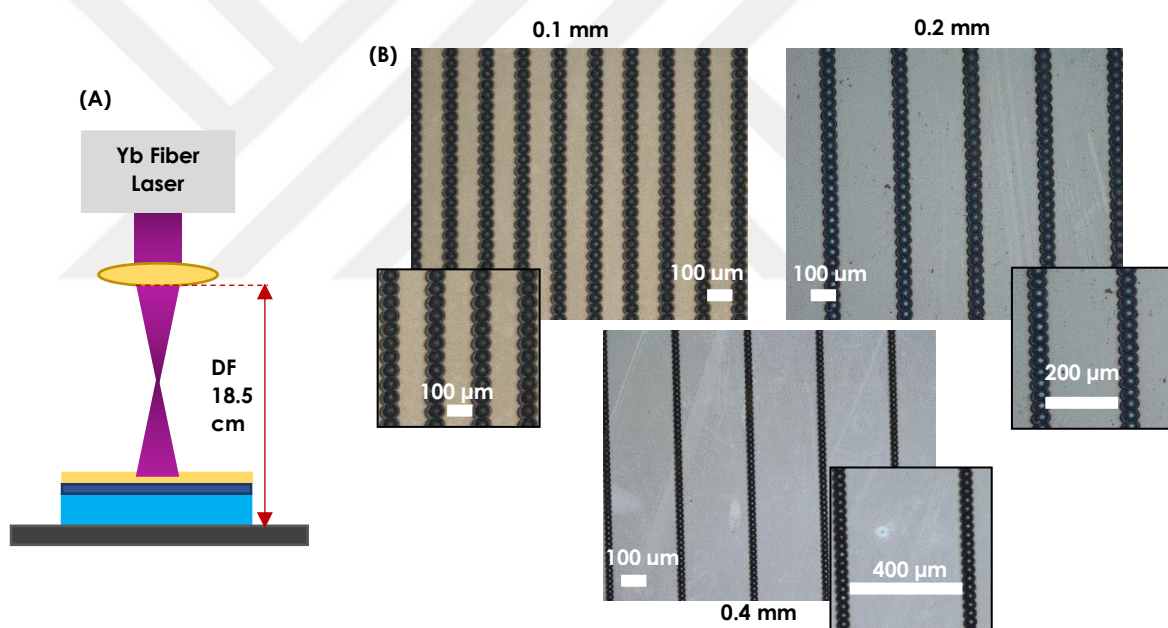


Figure 3.9: (a) “Out-of-focus” ablation conditions with DF adjusted to 18.5 cm. (b) Optical microscopy (OM) images of ablated substrates in “out-of-focus” DF distance showing significant changes in spot distances and spot appearances.

3.3.2.3 Imaging of ZnOs grown on substrates patterned under different DF

The morphological characterizations of pristine and patterned NR grown substrates have been performed via OM analyses. Figure 3.10 represents the “in-focus” patterned NR grown film formations where the distance between vertical laser-ablated patterns seems to have a significant effect on the homogeneity of the 1D structures. The given images clearly show the presence of a different phase on the patterned alleys. From the obtained OM images, it can be concluded that in 0.1 mm distant ablation patterns, NR growth is concentrated specifically on ZnO alleys, while the Ti remaining zones (inter-pattern regions) are relatively bold. The zoomed image of 0.1 mm pattern also proves the existence of densely packed NR formations along the ablation pathway. In zoomed images of 0.2 and 0.4 mm distant patterns, a significant formation of dense NR phase can be distinguished from the rest of the film, as well. However, in these films, the inter-pattern regions are significantly more crowded in terms of NR formations. In other words, in distant vertical patterns, the middle regions have also contributed to NR growth reducing the selectivity effect.

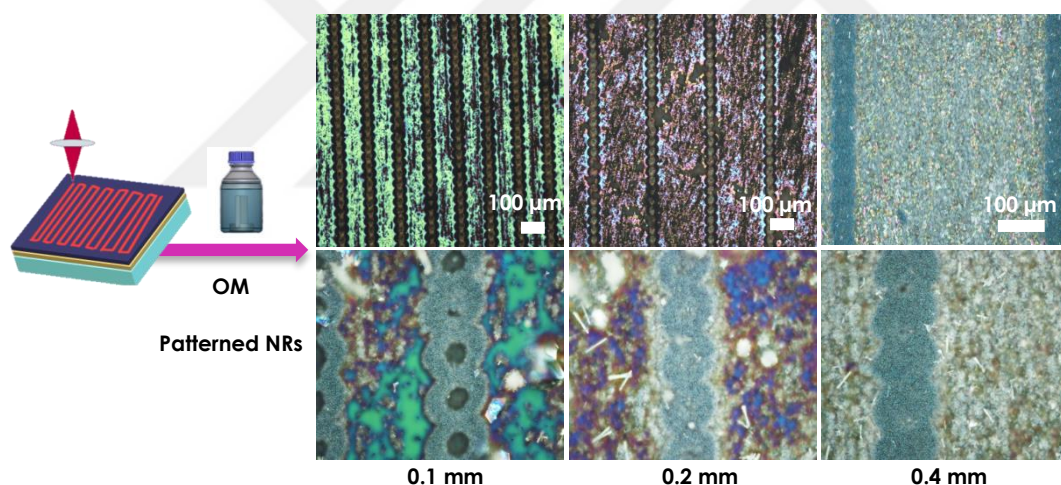


Figure 3.10: NR growth on “in-focus” patterned substrates generating distinct film homogeneities detected via OM analysis.

In the case of “out-of-focus” patterning, the OM images have shown a different thin film formation (Figure 3.11). Analyzing all three distances from the highest magnification, it has been observed that NR film formations have been accumulated on the borders of spots while the middle regions were nearly empty. This kind of thin-film formation has been attributed to the inhomogeneous distribution of energy on spots resulting in their deep ablation in the middle regions, therefore, inhibiting the growth of NR formations. The border regions of spots, on the other hand, as a result

of “out-of-focus” ablation, are accumulated with molten ZnO. At this stage, our aim was to determine the most plausible ablation distance for properly patterned, selective nanostructure growth. Analyzing the given optical microscopy images we have been able to conclude that operating at “In-Focus” conditions is going to generate more homogeneous and neatly patterned thin films formations. The upcoming part of this thesis is going to focus on the effect of changing fluence energy under constant focus distance.

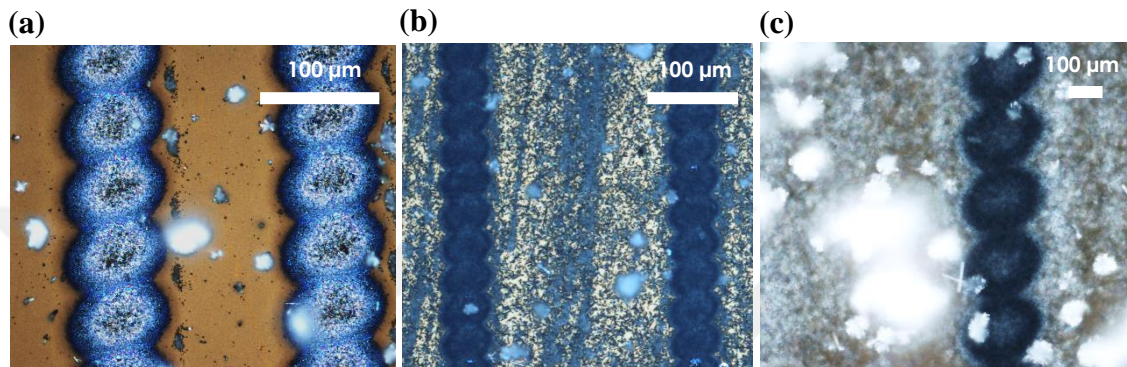


Figure 3.11: OM images of NR grown substrates under “out-of-focus” conditions patterned with (a) 0.1 (b) 0.2 and (c) 0.4 mm alley distances.

3.3.2.4 Examination of the effect of fluence energy on ablation performance

Following the extensive investigations of pure NR and NFI thin films and examination of the DF effect on patterning quality, our research has progressed to a new stage in which the selective growth of ZnO nanostructures, both individually and together, has been accomplished by using ns laser ablation technique. Two distinct laser beam intensities were used to process ITO/ZnO/Ti coated substrates. Table 3.3 details the equations that are utilized in the estimations of fluence energy ($\text{J}\cdot\text{cm}^{-2}$) which describes the energy of a laser beam and is defined as the pulse energy over the spot area. The energy of the applied beam is manipulated by varying three main laser parameters: (i) power (W), (ii) frequency (kHz), and (iii) scan rate (mm/s). The determination of the intensity of applied fluence energy in our work either targets selectively scribing the top Ti layer (120nm) avoiding the endamage of ITO/ZnO layers underneath or totally inscribing the whole three-layered film. Optical microscopy (OM) results obtained from the laser scribing procedure under $3.72 \text{ J}\cdot\text{cm}^{-2}$ fluence energy (7W, 4500mm/s, and 150kHz) system are given in Figures 3.12 (a) and (c). Here, consistently repeating $0.1\times 0.1\text{cm}^2$ and $0.5\times 0.5\text{cm}^2$ patterns have been obtained by

selectively ablating the top Ti layer. The verification of careful scribing of solely Ti layer has been performed via EDAX analysis taken directly from the ablated spot that clearly exhibits the presence of Zn and O elements. The post-hydrothermal output of these scribed films is analyzed via SEM and has shown a patterned NR development throughout the scribed region. The ablation-free area, on the other hand, show dense and sparse NR development for close and distant patterns, respectively. This NR growth has been attributed to the dissipation of heat during laser pulsing which lasts around 150ns. This period is considered to be long enough for metallic thin films which have an average heat transfer duration in the femtosecond range. Moreover, in close-distance patterns, this dissipation of heat takes place in a much smaller area completely deactivating the inhibitor nature of Ti films.

Figures 3.12 (b) and (d) demonstrate the second set of ablated substrates where the 28.43 J.cm^{-2} has been applied by ns fiber laser. This energy has been achieved by designating 25W, 5500mm/s, and 70kHz as ablation parameters. Because the implemented fluence energy is extremely high to provide any kind of selective scribing, the three-layered thin film has been entirely scratched from the surface in the predetermined pattern. In addition to optical and electron microscopy images of samples acquired under high energy scribing, Figure 3.12 (d) also demonstrates the elemental distribution within the ablation spot showing no presence of either Zn or Ti. Instead, peaks evidencing O, Mg, C, Si, and Na atoms validate the deep penetration of laser beam that completely scribes three-layered film till the glass. Here, an important parameter to be discussed is the resultant CBD growth on high-energy ablated substrates. As shown in the SEM images, the nucleation and growth mechanism of ZnO drastically changes under the presence of a different seeding layer within the same CBD environment. For $0.1 \times 0.1 \text{ cm}^2$ patterns (Figure 3.12 (b)), the excess fluence energy and extremely close pattern spots resulted in complete ablation of the whole film from the surface. This ablation has generated a result very similar to the completely scribed ITO/ZnO/Ti that was performed on purpose in order to obtain a pristine NFl growth.

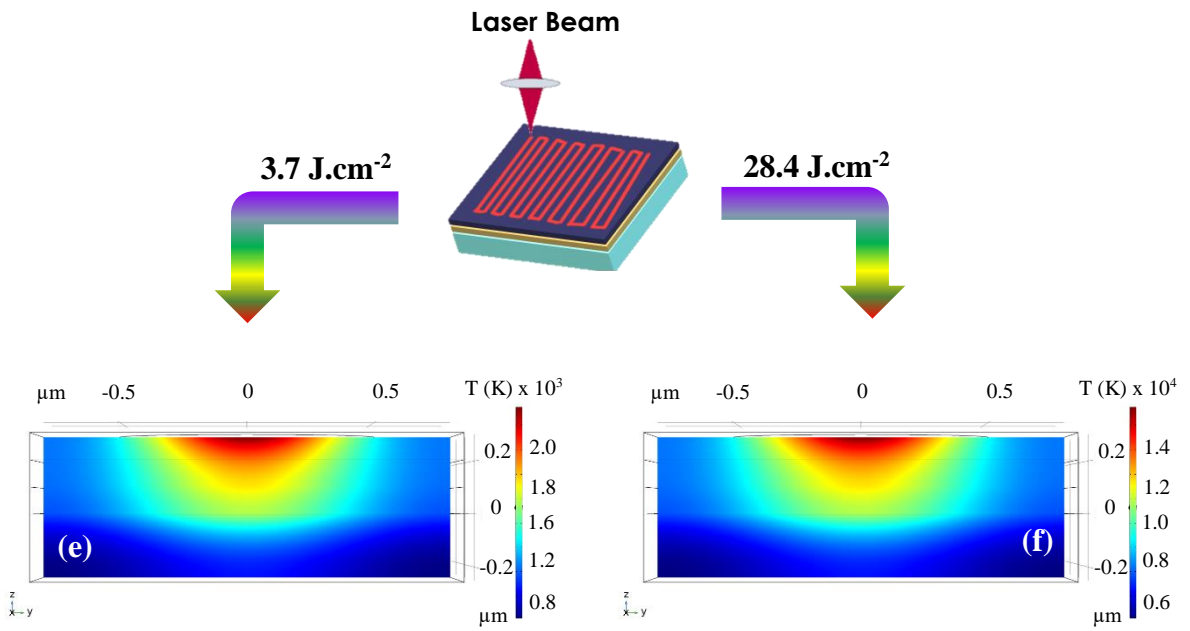
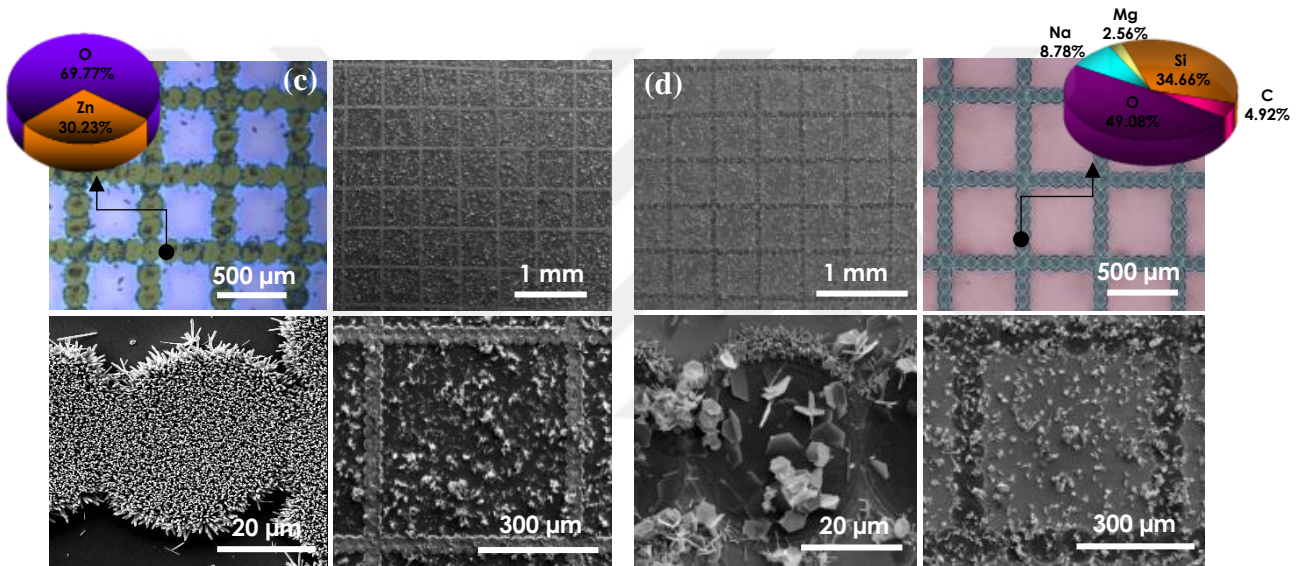
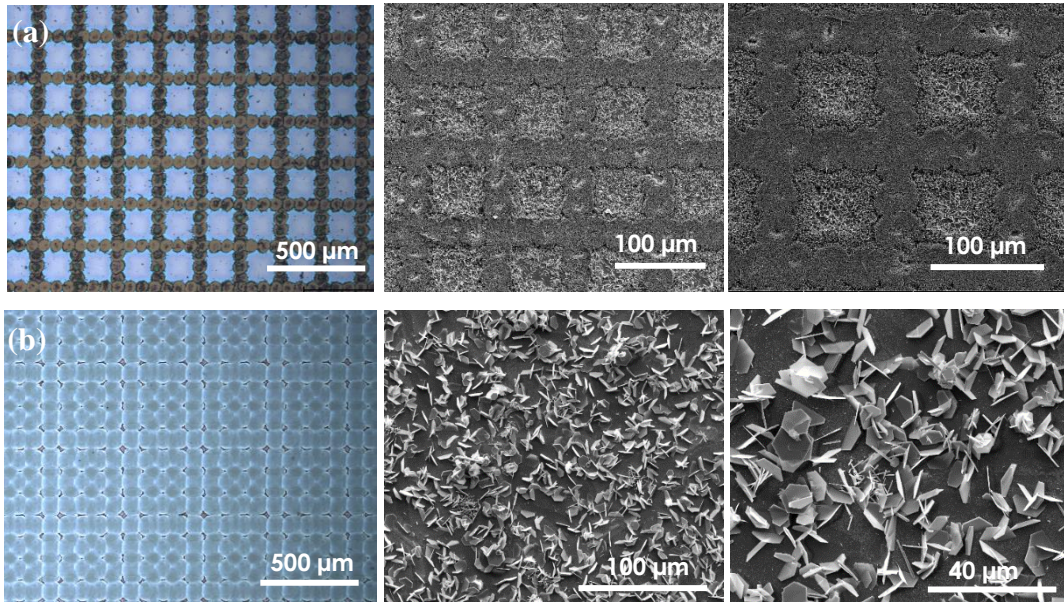


Figure 3.12: OM images of 0.1x0.1cm² laser patterned substrates with their corresponding CBD grown SEM images under (a) 25W, 5500 mm/s, 70 kHz and (b) 7W, 4500 mm/s, 100 kHz application. OM images of 0.5x0.5cm² laser patterned substrates with their corresponding CBD grown SEM images under (c) 25W, 5500 mm/s, 70 kHz and (d) 7W, 4500 mm/s, 100 kHz application. Numerical simulations representing the temperature distribution profiles from cross-section under (e) 3.7 and (f) 28.4 J.cm⁻² fluence energies.

In a similar manner, CBD growth performed on this closely patterned substrate generated a purely NFI-consisting film formation. In 0.5x0.5cm² patterns, mid-regions of spots that are nothing but soda-lime glass, ensure the formation of NFI structures (Figure 3.12 (d)). The border region of spots, on the other hand, are accumulated with molten, non-evaporated ZnO that provides the sporadic growth of nanorods.

The examination of the “laser beam – ITO/ZnO/Ti deposited substrate” interaction has been conducted via numerical techniques by using COMSOL Multiphysics Heat Transfer module. The calculation of the distributed temperature over the three consecutive thin film layers was carried out by using equations 3.6 - 3.8. Details of equation constituents are elaborated in Table 3.5. A more in-depth discussion of numerical simulation assessments may be found elsewhere [95]. As previously stated, fluence energy has been controlled by varying parameters like power, frequency, and scan rate of the applied beam.

$$\left[[c_p + L_m \delta(T - T_m) + L_v(T - T_v)\rho] \right] \frac{\partial T(x,y,t)}{\partial t} + \nabla \cdot [-k \nabla T] = Q \quad (\text{Eq. 3.6})$$

$$\delta(T - T_{m,v}\Delta) = \frac{1}{\sqrt{2\pi\Delta}} \exp \left[-\frac{(T - T_{m,v})^2}{2\Delta^2} \right] \quad (\text{Eq. 3.7})$$

$$Q(r, z, t) = \frac{2\varphi_0\alpha(\lambda)}{\sqrt{\frac{\pi}{\ln 2\tau_p}}} (1 - R(\lambda)) \exp \left[\frac{2r^2}{\omega_0^2} - (4\ln 2)(t/\tau_p)^2 - (\alpha(\lambda)z) \right] \quad (\text{Eq. 3.8})$$

The temperature distribution over ITO/ZnO/Ti layers is represented from the cross-sectional aspect in Figures 3.8 (c) and (d). Here, a single pulse period has been designated as 95ns and applied fluence energies as 3.7 and 28.4 J.cm⁻², respectively. The obtained simulation results show a temperature distribution difference around 7 folds between high and low fluence ablations. These results clearly rationalize the reason for the differences in beam penetration depths. Studies based on laser-ablated thin film scribing that have been published so far verify our modeling results by obtaining extremely high temperatures for a variety of fluence energies [96–98].

Table 3. 5: Parameters used for COMSOL Multiphysics simulation calculations with their significances and units

Parameter	Significance	Unit
k	Thermal conductivity	W.m ⁻¹ .K ⁻¹
ρ	Material density	kg.m ⁻³
T_m	Melting temperature	K
c_p	Heat capacity at constant P	J.kg ⁻¹ .K ⁻¹
L_m and L_v	Latent heat of fusion and vaporisation	J.kg ⁻¹
Q	Laser pulse energy source	W.m ⁻³
φ_0	Peak fluence	J. m ⁻²
$R(\lambda)$	Film reflectivity	-
τ_p	Full width half maximum of pulse duration	s
r	Radial coordinate	m
ω_0	1/e ² of spot radius	m
$a(\lambda)$	Material absorption coefficient	m ⁻¹
z	Depth component	m

PL and UV/Vis spectroscopy investigations were used to study the differences in material characteristics of samples after being patterned (Figure 3.13). It is important to note that at this stage of the study pristine samples have been compared with 0.1x0.1 and 0.5x0.5cm² square patterns. The first apparent difference to be underlined while analyzing the PL outcomes of pristine and patterned NR samples (Figure 3.13 (a)) is their generation of different emission intensities. The PL intensity of pristine NR film

is substantially low, but it dramatically increases in patterned samples. This is due to the growing surface area of the samples, which contributes to stronger luminosities. There is also a discernible difference between two distinct patterns. The rationalization of this distinctness can be performed by concurrently analyzing and correlating PL and SEM data. $0.1 \times 0.1 \text{ cm}^2$ patterned geometries are too close to each other and these tiny distances in-between patterns result in poor heat dissipation that slenderizes the intact thin-film regions. As a result, Ti layers become much thinner and lose their ZnO-inhibiting nature procuring a scanty NR formation in non-ablated regions. For $0.5 \times 0.5 \text{ cm}^2$ patterns, on the other hand, different circumstances are observed to apply. Here a decent distance between patterned regions handles the dissipation of heat better. Therefore, a much more clean and precise NR growth can be observed over the ablated regions resulting in more intense PL emissions.

Application of high fluence energy resulted in dual growth of NR and NFI formations, as stated above. In this situation, it has been expected from the ZnO emissions to generate spectra containing the segments of both nanostructures, individually. As can be seen from Figure 3.13 (b), substrates ablated in $0.1 \times 0.1 \text{ cm}^2$ pattern under high fluence generate an almost similar PL spectrum to the films obtained under complete ablation of ITO/ZnO/Ti layers. In other words, substrates with no pattern (i.e. complete scribing) and $0.1 \times 0.1 \text{ cm}^2$ square scribing result in the growth of similar nanostructured film as a result of the CBD step. In order to understand the rationale behind this situation, PL data has been againward correlated with SEM images. Images given in Figure 3.12 (b) clearly show that high fluence energy on a short-distance pattern generates spots of $\geq 40 \mu\text{m}$ diameter and result in an ablation texture which is very similar to complete ablation. Therefore, SEM images of the aforementioned substrates evidence only NFI formations.

For $0.5 \times 0.5 \text{ cm}^2$, however, completely different PL emission spectra can be observed. Here, the distance between spots is large enough to provide a homogeneous and bordered pattern under high fluence energy. On the other hand, the accumulation of molten ZnO contributes to the formation of NRs which are grown in addition to indigenous NFIs. As a result, a single substrate has been proven to provide the required environment for the simultaneous growth of NR and NFI structures within the same CBD environment.

The correlation between ZnO thin film emissions and their optical material characteristics has been established via UV/Vis analysis. Here, the aim was to prove that the changing absorption characteristic is the main cause of PL performance variation. Figures 3.13 (a) and (b) demonstrate a slight superiority for non-patterned films within the UV region. This superiority in absorbance values sharply decreases while approaching and reaching the visible range. Non-patterned substrates, on the other hand, possess higher light capturing surface area. This increase in the irradiated portion of the film is attributed to the effect of patterning. Hence, by changing the light absorption mechanism of thin films as a result of dual nanostructure growth, within this part of the thesis work we have been able to ensure a much more intense photoluminescence generation.

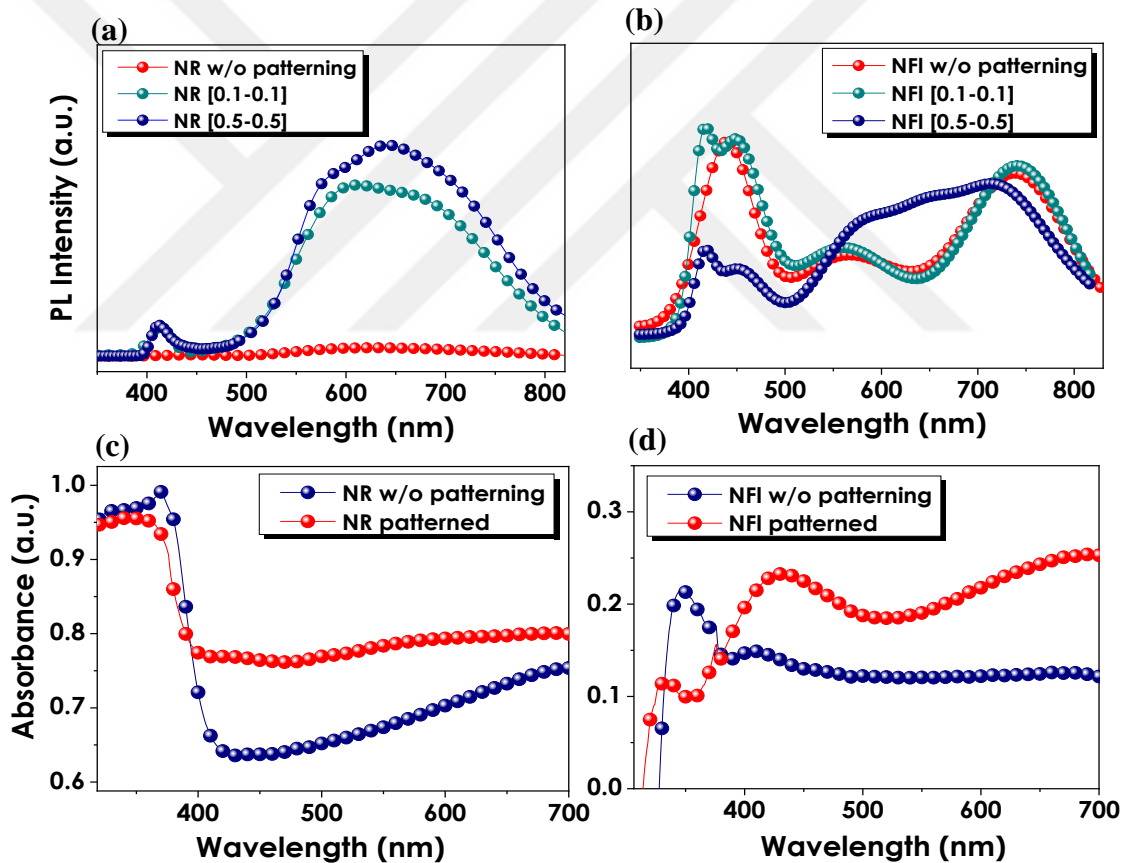


Figure 3.13: Photoluminescence performances of intact (i.e unpatterned), $0.1 \times 0.1 \text{ cm}^2$ and $0.5 \times 0.5 \text{ cm}^2$ patterned (a) NR and (b) NFI films. Optical absorption data of patterned and unpatterned (c) NR and (d) NFI structures.

3.4 Conclusions

Finally, by smartly modifying substrate characteristics with ns fiber laser, the concurrent growth of ZnO NR and NFl formations in the same CBD environment has been achieved. The effect of applied fluence energies on the temperature distribution profiles of three-layered thin films has been evaluated and examined via COMSOL Multiphysics. Under 3.7 and 28.4 J.cm⁻² fluence energies, the evaluated substrate temperatures were determined to be around 2200 and 14000 K, respectively. The obtained temperature profiles have been found to be in good agreement with experimental ablation outcomes explaining the reason behind controlled and uncontrolled laser penetration depths. The simultaneous growth of selective and patterned ZnO nanostructures has been accomplished by compounding these two scribing characteristics on a single substrate. As a result, the individual PL properties of both nanostructures have been integrated on a single substrate, expanding the emission spectrum throughout the visible range and increasing the composite PL intensities by around sevenfold.

CHAPTER 4

4. ENHANCEMENT OF PHOTOLUMINESCENCE PERFORMANCE OF MULTIMORPHOLOGICAL ZnO VIA METAL HALIDE PEROVSKITE SENSITIZATION

4. 1. Introduction

All inorganic cesium halide perovskites, CsPbX_3 (X: Cl, Br, I), by virtue of their superlative optoelectronic properties, such as high carrier mobility, tunable direct band gaps, large absorption coefficients and long diffusion lengths, have been a featured subject to be explored for optoelectronic devices, including light-emitting diodes (LEDs), solar cells and photodetectors [99,100]. Particularly, CsPbBr_3 exhibits much better environmental stability which does not require harsh conditions for the synthesis and applications [101]. Furthermore, the recent studies conducted on all-inorganic perovskite-based LEDs show that nanocrystals of CsPbBr_3 imbedded in a Cs_4PbBr_6 host matrix exhibited much better photoluminescence quantum yield (PLQY) up to 90% [102] in contrast to very low light yield from a bulk single crystal or polycrystalline CsPbBr_3 [103,104]. In fact, the optical properties of Cs_4PbBr_6 crystals could not be entirely investigated in the literature because of the coexistence of CsPbBr_3 hindering the proper characterization. Particularly, the origin of luminescence properties of these mixtures is a contradiction in which some reports attributed the luminescence ability to the presence of CsPbBr_3 , while others build on their explanations on the intrinsic property of Cs_4PbBr_6 [105–107]. Numerous studies combining ZnO and inorganic halide perovskites (IHPs) can be encountered in the literature among which most utilize ZnO as electron transport layers for the improvement of solar cell performances [108–111]. In addition to this, studies sensitizing IHPs with ZnO nanoparticles/thin films for photodetector and LED applications have been recently investigated as one of the most attractive topics [112–114]. However, none of the reported studies so far have focused on the enhancement of ZnO luminescence abilities via the incorporation of perovskites, especially in simultaneously grown multi-morphological patterned nanostructure arrays. In this part of the thesis work, both pristine Cs_4PbBr_6 and CsPbBr_3 imbedded in Cs_4PbBr_6

perovskites have been deposited on multi-morphological patterned ZnO thin films for PL performance improvements and further LED applications. Hence, the study reported herein features numerous novelties for the production of highly efficient ZnO-based LED devices. For the very first time in the literature, easily patterned ZnO thin films embodying 2 different nanostructures have been decorated with polycrystalline IHPs and their combined luminescence performances have been investigated.

4.1.1 Metal Halide Perovskites

Perovskites, a large family of materials that resemble the crystalline structure of calcium titanate (CaTiO_3), are being named after Russian scientist Lev Perovski. The general structural representation of perovskites is ABX_3 , where “A” and “B” represent the cations of different sizes and X stands for the anion within the chemical structure [115]. This family of materials can be divided into three different classes known as (i) organic, (ii) inorganic, and (iii) organic-inorganic hybrid perovskites. For the last few years, inorganic metal halide perovskites have started to attract lots of attention due to their superior material properties such as high thermal stability and better endurance to light exposure. These outstanding properties of metal halide perovskites have been obtained owing to the presence of inorganic cations that have comparably high decomposition temperatures [115]. Moreover, in contrast to the organic-inorganic hybrid perovskites, metal halide perovskites possess a relatively more balanced charge carrier mobility [116]. Analyzing the components of metal halide perovskites in detail, cesium (Cs) or rubidium (Rb) can be used for “A” and bismuth (Bi) or lead (Pb) can replace the component B. On the other hand, chlorine, iodine, or bromine ions can be used as the anions of the chemical structure [115]. Several different morphologies of perovskites such as single crystal, nanocrystal, and polycrystalline perovskites can be encountered in the literature. One common characteristic of all these structures is the ability to synthesize them via wet-chemistry (i.e. solution processing) which is a highly preferred synthesis method due to its time, money, and energy-saving features. Morphology, being one of the key determinant parameters of perovskite structures, is highly dependent on synthesis conditions and directly affects basic materials properties such as optical and electrical characteristics. For instance, a study reported by Song et al. has evaluated $2000 \text{ cm}^2 \cdot \text{V}^{-1} \cdot \text{s}^{-1}$ as charge carrier mobility for perovskite single crystals [117]. On the other hand, another research team has investigated the mobility of perovskite nanosheet thin films and reported them to be around $78 \text{ cm}^2 \cdot \text{V}^{-1} \cdot \text{s}^{-1}$.

$^1\text{s}^{-1}$ [118]. Similarly, the effect of morphology and chemical composition on the photoluminescence abilities of perovskites has also been studied by several research groups [116,119]. This simple ability to alter basic material characteristics of perovskites via changing their synthesis conditions, makes them suitable and preferable candidates for light-emitting, photodetector, and solar cell application.

ABX_3 and its morphological and compositional variations are among the most commonly encountered perovskites in the literature. However, in the last few years, number of various novel crystalline structures of perovskites are being studied and reported. That's why the overall definition of perovskites has turned to be more confusing. One of the recently reported studies by Song et al. has categorized perovskites into three main subgroups which are; (i) standard perovskites, (ii) low-dimensional (Low-D) perovskites and (iii) perovskite-like halides [120]. The standard perovskites, ABX_3 , have cubic structures where A is the large and B is the small cation. Low-D perovskites, on the other hand, have been developed as an alternative to standard perovskites. The main advantageous features of this crystalline structure over the standard one are its improved stability and lower toxicity. CsPb_2Br_5 and Cs_4PbBr_6 are two of the representatives of low-D perovskites, respectively representing two-dimensional (2D) and zero-dimensional (0D) structures. Cs_4PbBr_6 , specifically, is known to be high-performance emitter with excellent luminescence abilities [121]. Moreover, the crystalline structure of 0D Cs_4PbBr_6 is reported to be either orthorhombic or rhombohedral. Within the course of fourth part of this dissertation, we are going to focus on CsPbBr_3 and more specifically on Cs_4PbBr_6 having superior PL performance, enhancing the overall luminescence abilities of previously discussed multi-morphological ZnO.

4.1.2 Photoluminescence Properties of Metal Halide Perovskites

The luminescent abilities of materials are directly related to their electronic structures. The electronic configuration of materials, on the other hand, is dependent on several factors such as elemental composition and crystalline structure. In perovskites, chemical composition directly affects the band structure. In the case of a hybrid perovskite, for instance, the inorganic layer has a more dominant influence on luminescence performance. This superior effect of inorganic elements generates due to the fact that the band gap of perovskite structure is influenced by the electrons

occupying p-orbitals of Pb atoms. The role of organic components only contributes to the adjustment of the band by either stretching or bending it. Therefore, the chemical composition of perovskites is highly dependent on the types of elements constituting their structure. In general, halide perovskites are reported as direct band gap semiconductors with a strong band-edge absorption and luminescence. In perovskite materials, luminescence is generated as a result of radiative processes. This includes electron-hole recombination, the transition between mid-band levels and band-to-band transitions. However, the direct band gap possessing nature of perovskites is a phenomenon that does not apply to all types of perovskite materials and has several exceptions that can be observed for non-centrosymmetric hybrids. BX_6 building blocks of the perovskite crystal structure are playing a defining role in the electronic structure at the band edge. Thus, the crystal structure that directly affects the arrangement of BX_6 units plays an important role in understanding in a variation of luminescent behavior of perovskites [122].

4.1.3 Cs_4PbBr_6 Structure of Perovskites and Their Superior Luminescent Properties

Recent studies have reported that the decrease in the dimensionality of perovskites from 3D to 0D results in a significant increase in the states of localized electrons thus narrowing the gap between valence and conduction bands. This shrinking in band gap causes the self-entrapment of excitons and therefore provides a more severe excitonic emission [123]. Hence, these outstanding emission abilities are the reason why Cs_4PbBr_6 attracts this much attention. Compared to standard $CsPbBr_3$ perovskites that have a crystal structure with $[PbBr_6]^{4-}$ corner-sharing, Cs_4PbBr_6 is composed of arrays where octahedral $[PbBr_6]^{4-}$ is isolated via Cs^+ ions [124]. This isolation of octahedra weakens the orbital coupling between conduction and valence bands generating more flat bands and causing widening in the band gap. Therefore, compared to $CsPbBr_3$ which possesses a bandgap of around 2.3eV, Cs_4PbBr_6 is reported to have a band-gap of around 3.90 eV. However, this severe difference in E_g values does not inhibit the strong green luminescence of 0D perovskites. As it has already been discussed in Section 4.1.2, the luminescence of $CsPbBr_3$ perovskites originates from radiative recombinations. Interestingly, although both 3D and 0D structures of perovskites possess identical PL peaks and comparable quantum yields, the mechanism behind

their emissivity differs vastly. This difference is the result of significant variations in other optical properties of perovskite materials. More specifically, a study conducted by Wang et al. revealed the presence of an extended Urbach tail within the UV-Vis spectrum of Cs₄PbBr₆ nanocrystals ($E_u = 1.7$ eV) which have been one of the strongest evidences showing that the origin of green emissions in 0D perovskites is defect-related [124]. This theory has been further extended by other research groups that have concurrently investigated the absorption spectra and time-resolved PL performances of Cs₄PbBr₆ nanocrystals. Another study conducted by Liu et al. revealed that Cs₄PbBr₆ has gone through different relaxation pathways such as migration of excitons to defect levels (fs), relaxation of excitons within defect states (ps), and recombination of excitons (ns). Thus the detailed investigation of the origins of emissions supported the theory that green emissions of Cs₄PbBr₆ are mostly originated from lattice defects [125].

4.2 Experimental Methods

4.2.1 Preparation of substrates

Metal halide perovskites have been deposited on substrates whose preparation steps have been elaborated in Section 3.2. Briefly, soda-lime glasses deposited with ITO layer have been used as substrates for consecutive coating of ZnO and Ti layers. The double-layered thin film was aimed to provide selective ZnO nanostructure growth after being carefully patterned via ns laser ablation method. Two different fluence energies (3.7 and 28.4 J.cm⁻²) have been administered on the substrate via ns fiber laser. This resulted in the generation of NRs under low and NFIs under high fluence energies. By smartly controlling the fluence energy and determining the ablation pattern, these substrates have provided a suitable environment for the concurrent growth of both nanostructures within the same CBD environment. Please see subsections 3.2.1 and 3.2.2 of Chapter 2 for details.

4.2.3 Metal halide perovskite sensitization of patterned ZnO thin films

CsPbBr₃ have prepared by consecutively spin-coating;

(i) 1M lead bromide (PbBr₂) dissolved in dimethylformamide (DMF) under 2000 rpm-30 seconds pursued by

(ii) 0.07M cesium bromide (CsBr) dissolved in butanol under 2000rpm-30s.

In between the spin coating steps, substrates have been dried at 80 °C for an hour in order to provide complete evaporation of the solvent. The compositions of the obtained perovskites have been altered through the variation of CsBr spin cycles. Here, the application of a single cycle of CsBr resulted in the generation of composite CsPbBr₃-Cs₄PbBr₆ crystalline structure while increasing this number to 5 formed pristine Cs₄PbBr₆ crystallites. It is important to note that, in order to obtain the final form of samples as given in Figure 4.1, all substrates have been subjected to a post-annealing procedure under 280 °C for 10 minutes.

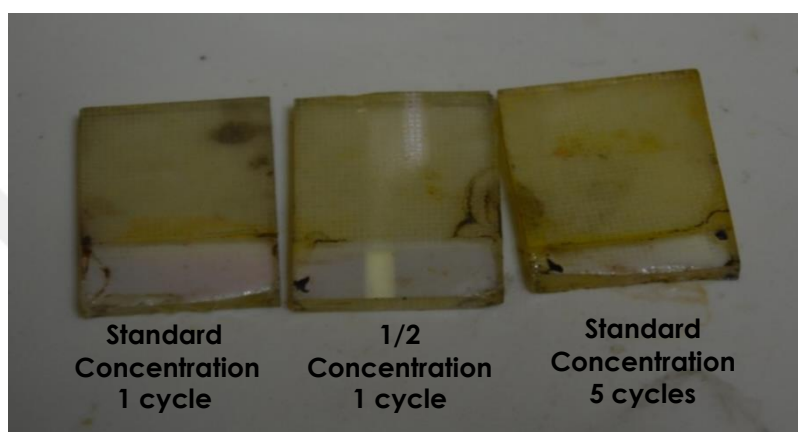


Figure 4.1: Image of perovskite deposited patterned ZnO thin films under different CsBr concentrations and number of spin cycles.

4.3 Results and Discussion

4.3.1 Fluorescence microscopy imaging of pristine and patterned ZnO thin films

The previous part of our thesis work was based on the investigation of multi-morphological ZnO and its simultaneous growth on smartly modified, laser-ablated ITO/ZnO/Ti substrates. The obtained PL performances have demonstrated a substantial enhancement as an effect of patterning. Moreover, compared to their pristine forms, the combined presence of NR and NFIs have resulted in a luminescence performance that emitted light almost throughout the whole visible region. Fluorescence microscopy (FM) imaging has been performed as a fortiori analysis to PL. This techniques, slightly resembling optical microscopy, has been used to excite the given ZnO thin films under different incoming light energies. The images given in Figure 4.2 show the UV excitation of ZnO films under 365nm wavelength resulting in

blue emission at approximately 445-450nm. Due to the limited resolution of the fluorescence microscope, it was difficult to observe discrete nanostructures. Therefore, larger impurities randomly generating as a result of the inhomogeneous energy distribution of laser beams have been used as guides to depict the presence of nanostructures. Elemental composition of the significantly big impurities given in Figures 4.2 (a) and (b) has been investigated via EDAX analyses showing the presence of Zn, O, Mg, Si, and Cl which either play the role of reagents in the formation of NFIs or are the components coming to the surface as a result of ablation. Figure 4.2 (c) shows more distinct nanoflake features which have been observed from the top. In contrast to comparably bold and scattered NF film formation, NRs given in Figure 4.2 (d) have a more dense packing. These films have therefore generated a stronger background luminescence as can be seen from Figure 4.2 (e). A single outgrown rod on the top of NR film has also been depicted in FM and generated a significant blue luminescence. At the final stage of the investigation of pristine ZnO films, NRs grown in square patterns have been given in Figure 4.2 (f). As can be observed from the obtained FM image, the NR containing square borders emit stronger, while the centers of square patterns generate significantly darker emissions. This is directly correlated with the fact that due to $0.5 \times 0.5 \text{ cm}^2$ patterning of squares under low fluence energies, homogeneous and dense ZnO growth has been attained on square borders.

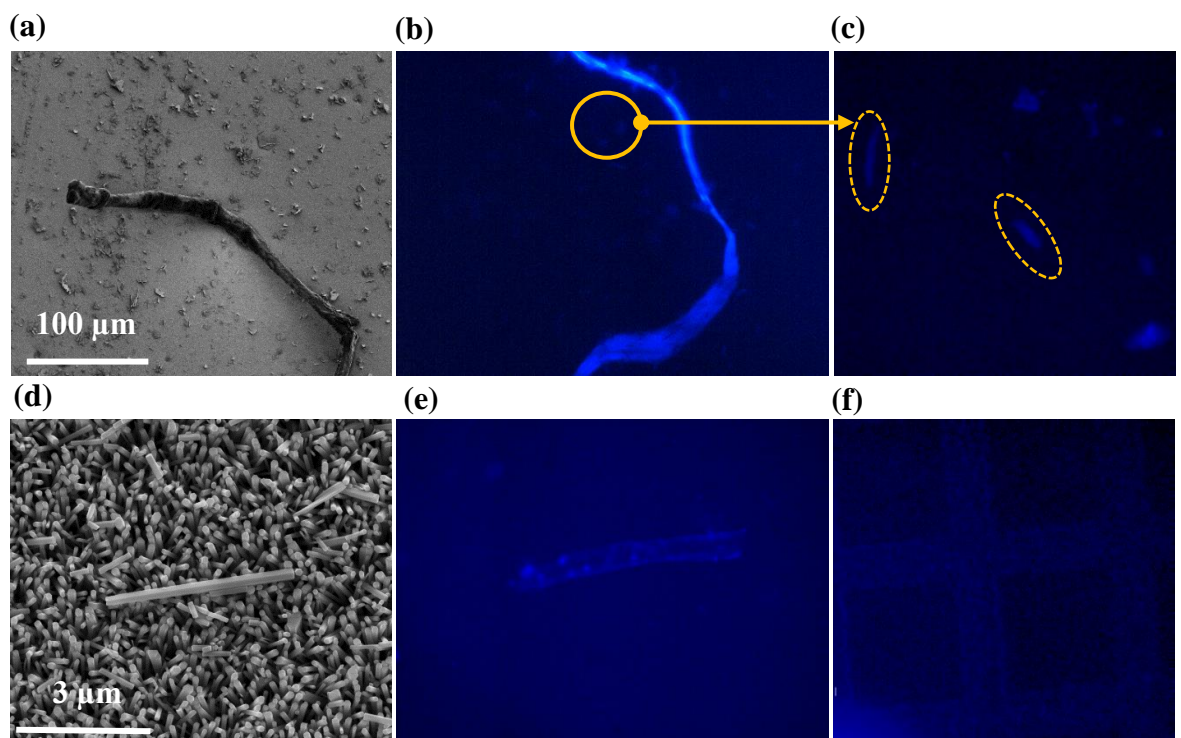


Figure 4.2: (a) SEM image obtained from the large impurity formed on NFl grown thin film surrounded with tiny nanoflakes scattered around. (b) FM image of the impurity containing Zn, Mg, Si, and O atoms emitting the blue light under UV excitation thus enabling the observation of (c) tinier NFl species. (d) SEM image of ZnO NRs with a randomly outgrown single rod lying on the top of the homogeneous film. (e) FM image obtained from approximately same region showing a strong luminescence from the single rod itself in addition to strong blue emission coming from the background of densely packed NR films. (f) FM image obtained from patterned NRs showing a strong blue emission from the corners of square patterns where rod formations are grown and darker emissions from the centers which a comparably bolder.

4.3.2 Effect of Cs₄PbBr₆ on PL performances of patterned multi-morphological ZnO thin films

Inorganic lead halide perovskites have shown a tremendous track record of intense luminosities and have therefore been frequently implemented into LED appliances. Owing to the promising nature, relatively good stability, and high quantum yields of this group of perovskites, it has been decided to incorporate them into patterned NR/NFl samples. As a result, much stronger PL emissions have been expected to be observed in a broader range. As mentioned above, during the IHP synthesis step, the spin number of CsBr layer has been altered and consequently, two different perovskite films with PbBr₂:CsBr ratios of 1:1 and 1:5 have been obtained.

IHP deposited patterned substrates have been characterized via methods comprising morphological, optical, and crystallinity-based techniques. In FM, perovskite deposited samples have been analyzed under the application of UV, blue, and green sources of excitation. For comparison purposes, bare ZnO grid samples, before being deposited with perovskite layers, have been analyzed under FM (Figures 4.3 (a) and (b)). Grid samples emit a strong blue emission in their natural state due to UV illumination (365 nm), which is directly within their bandgap. Perovskite-deposited patterned samples, on the other hand, have been excited with blue source (470 nm) and generated green-emissions as given in Figures 4.3 (c) and (d). The obtained emissions match the bandgap of 0D Cs₄PbBr₆, and do not generate fluorescence either within UV or red sources of excitations. Observing the individual FM outcomes of IHP deposited

patterned substrates, it's clearly seen that for 1:1 ratio of $\text{PbBr}_2:\text{CsBr}$ the green emission comes directly from laser scribed regions.

The fluorescence of 1:5 $\text{PbBr}_2:\text{CsBr}$ deposited substrates, on the other hand, emits from the center of the square patterns (Figures 4.4 (a) and (b)). The reason behind this type of difference in luminescent areas is assumed to be originated from the varying dimension of crystallites. To put it differently, the alteration in $\text{PbBr}_2:\text{CsBr}$ changes the eventual crystalline structure of perovskites, consequently affecting their dimensional parameters, as well. In this case, larger crystals have a tendency to accumulate in areas more plausible for their settlement. Therefore, tinier crystals of composite $\text{CsPbBr}_3\text{-Cs}_4\text{PbBr}_6$ allocate themselves on the borders while pristine 0D Cs_4PbBr_6 settles in the mid-region. The numerical equivalent for the fluorescence intensities acquired from the marked-up region of the FM image is given in Figure 4.4 (c). Analyzing the plots given in Figures 4.3 (e) and 4.4 (c), a substantial decay in the fluorescence intensities can be observed towards the darker regions. Figure 4.3 (f-h) and 4.4 (d-f) exhibit the SEM images obtained from patterned ZnO substrates deposited with 3D and 0D IHPs, respectively. In the zoomed images, the side regions of patterned squares show a crowded presence of ZnO NRs that are accumulated there due to the presence of a molten ZnO seeding layer. The bulky stack surrounding those NR formations, on the other hand, stands for the perovskites that are post-deposited on patterned substrates. Comparing the two samples obtained at different $\text{PbBr}_2:\text{CsBr}$ ratios, it can be seen that for the 1:5 ratio the generated IHP layer possesses much bigger grains (i.e. broader grain boundaries).

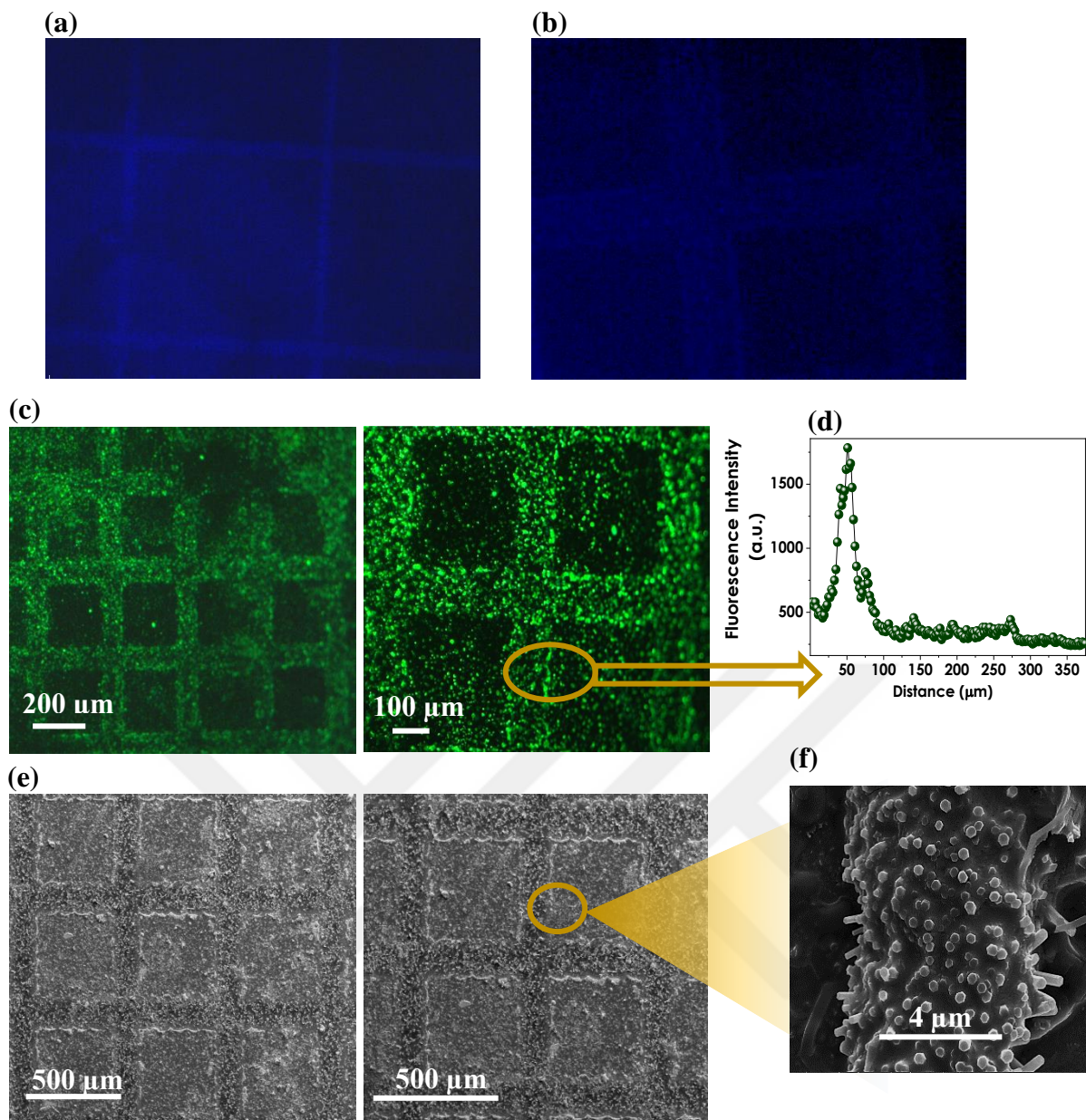


Figure 4.3: FM images of samples patterned under (a) 3.72 and (b) 28.43 J.cm⁻² fluence energies followed by hydrothermal growth of nanostructures obtained under 365 nm source irradiation. Fluorescence emission of samples deposited with (c) 1:1 perovskite layers with the corresponding representation of (d) emission intensity distribution along the punctuated region. (e) SEM images of the same sample set with (f) magnified image obtained from the edges of the pattern.

In order to validate the presence of a difference between grain sizes of IHPs obtained under different $\text{PbBr}_2\text{:CsBr}$ ratios, XRD analysis has been conducted. The XRD spectra of the 1:1 $\text{PbBr}_2\text{:CsBr}$ thin film reveal the presence of two distinct perovskite phases which are; (I) orthorhombic CsPbBr_3 and (II) rhombohedral Cs_4PbBr_6 (Figure 4.5 (a)) [126]. Nevertheless, the presence of Cs^+ at high amounts has been shown to transfer the crystallinity of IHPs from composite 0D-3D to pure rhombohedral [127,128]. This transition in the crystalline phase can also be evidenced within this study as given in Figure 4.5 (b). Because of the tiny crystal size, low concentration, and excellent dispersion of CsPbBr_3 within the Cs_4PbBr_6 , no distinctive diffraction peaks of CsPbBr_3 have been traced in Figure 4.5 (b) [129,130]. It is also important to point out that for composite phase and pristine Cs_4PbBr_6 crystals, a significant intensity difference has been detected. This variation in peak sharpness carries information regarding the differences in crystal sizes of both IHP phases. In order to interpret and rationalize these dimensional differences, crystal sizes of the obtained phases have been evaluated. The calculated outcomes have shown an increase in crystal size by ~ 4 folds while transferring from composite $\text{CsPbBr}_3\text{-Cs}_4\text{PbBr}_6$ to pure Cs_4PbBr_6 phase.

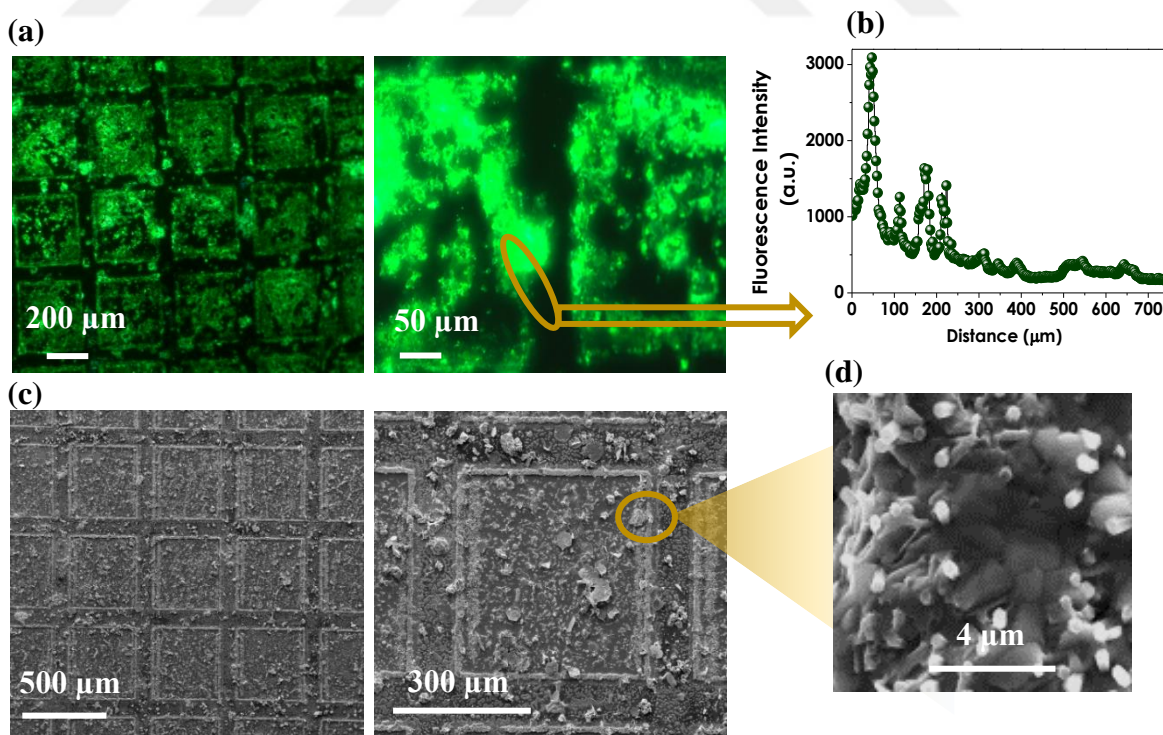


Figure 4.4: Fluorescence emission of samples deposited with (a) 1:5 perovskite layers with the corresponding representation of (b) emission intensity distribution along the punctuated region. (c) SEM images of the same sample set with (d) magnified image obtained from the edges of the pattern.

Figures 4.5 (c) and (d) show the light absorption and emission characteristics of perovskite deposited and patterned ZnO films. The acquired response indicates the presence of two peaks representing excitonic absorption at 382 nm and 517 nm, respectively. These wavelength values fall directly within the band edge positions of ZnO and IHP layers. In addition, as compared to their non-IHP deposited forms, the incorporation of Cs₄PbBr₆ on ZnO thin films exhibit an increased absorption performance within the visible range. The improved light-absorbing and emitting capabilities of IHP deposited ZnO films are in good agreement with a previously reported work that has analyzed CsPbBr₃ sensitized ZnO NR systems [131]. Figure 4.5 (d) shows the PL data acquired from IHP deposited and patterned ZnO thin films. The presence of intense, perovskite-inflicted emissions almost completely blocks the individual ZnO-originated luminescence. Even though defect-based ZnO emissions are completely eliminated after pristine Cs₄PbBr₆ deposition, for composite IHP-coated substrates a faint peak at 420 nm can still be observed. There is also a distinguishable difference in peak broadness and sharpness values in-between composite and pure IHP deposited ZnO thin films [132,133]. This broadening in the characteristic PL peak of composite IHP deposited ZnO substrate can be attributed to ZnO's individual broad emission range. The aforementioned broadening disappears for pristine Cs₄PbBr₆ deposited ZnO films proving the suppressing effect of highly luminescent 0D perovskites. At this stage, it is important to highlight that in order to establish a consistent comparison, each contrasted PL data has been analyzed under a 0.01nm slit number.

The obtained films have been subjected to transient photoluminescence (TrPL) analysis aiming to determine their minority carrier lifetimes in pure and IHP deposited forms. Figure 4.5 (e) shows a paired comparison of emissions generated at 420 nm from pristine and CsPbBr₃-Cs₄PbBr₆ (1:1 ratio) deposited patterned substrates. A bi-exponential fit with two decay periods (τ_1 and τ_2) has been applied on both data sets. Average minority carrier lifetimes (ns) are specified in the insets of Figures 4.5 (e) and

(f). The swift primary decay components of 2.24 and 2.12 ns have been observed for pristine and CsPbBr₃-Cs₄PbBr₆ deposited ZnO grid films, respectively. Based on our previous experience and thorough literature review, it can be concluded that these types of decays are caused by non-radiative recombinations at ZnO NBE. Second decay components, which are 15.90 and 22.49 ns for pristine and 1:1 perovskite deposited samples, respectively, have been attributed to the emissions generated at grain boundaries, consequently originating from the presence of defects. In one of the related studies, Li et al. have reported the changes occurring in minority carrier lifetimes of perovskites prior to and after the incorporation of ZnO into the structure [134]. According to this study, tinier grain dimensions (i.e. more grain boundaries) cause an increase in the densities of traps giving a rise to defect-based recombinations. Given that luminescence at 420 nm is the typical ZnO-originated emission, the increased carrier lifetime can be directly correlated with the changing composition of ZnO subsequent to perovskite deposition.

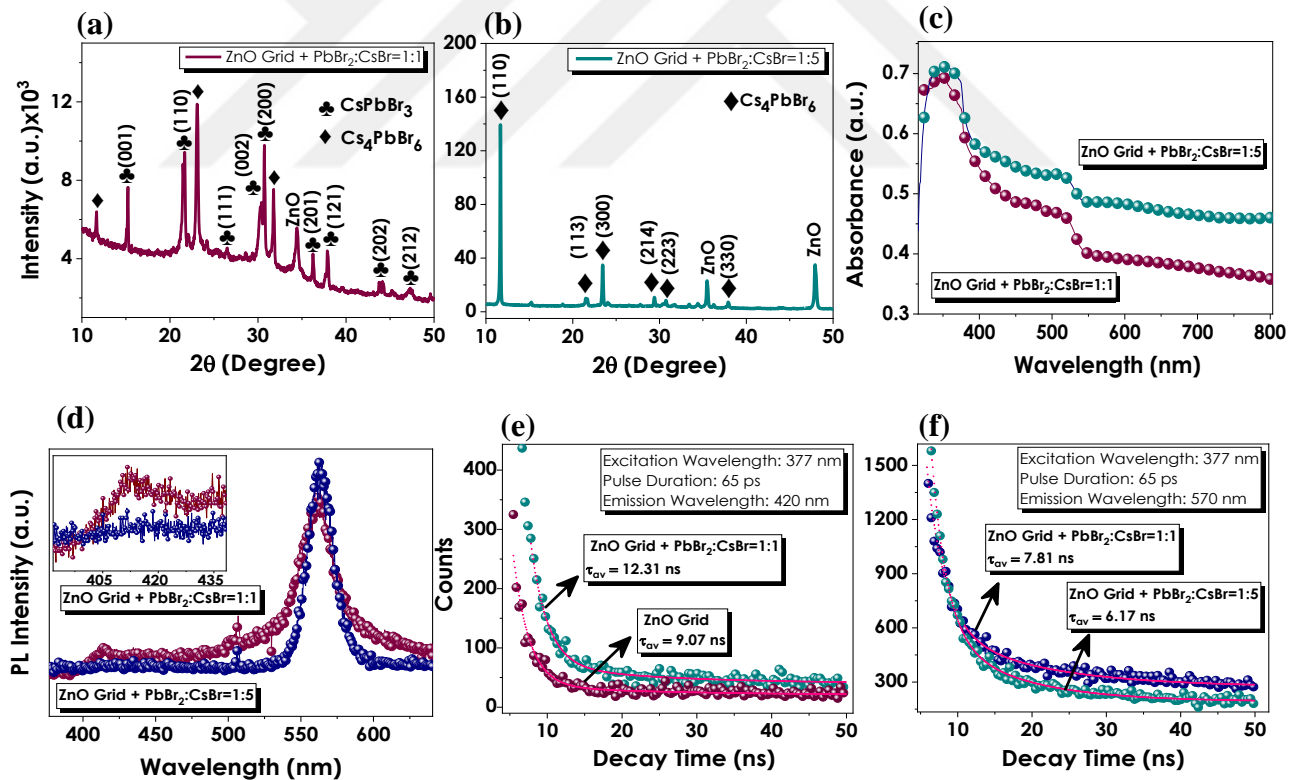


Figure 4.5: XRD responses of (a) 1:1 and (b) 1:5 PbBr₂:CsBr ratio deposited ZnO samples. (c) Optical absorption data of perovskite-deposited patterned ZnO thin films. (d) Photoluminescence spectra of perovskite-deposited patterned ZnO thin films. (e)

TrPL outcomes individually comparing carrier lifetimes at (e) ZnO-originated and (f) perovskite-originated emissions.

The incorporation of the perovskite layer onto patterned ZnO substrates requires numerous heating stages, which is expected to trigger significant changes in the crystallinity of ZnO. For this reason, the crystal size of ZnO prior to and after perovskite deposition has been calculated by taking the 34.2° (2 θ) peak as a basis. The calculations have been performed by using Scherrer's equation. The results obtained from this calculation demonstrate a reduction by ~3 folds in the ZnO crystallinities due to the post-annealing step that has been applied during perovskite deposition (Figure 4.6). Hence, it can be concluded that the prolonged minority carrier lifetime of ZnO can be correlated with their diminished grain sizes, consequently increasing the decay component of defect-based emission.

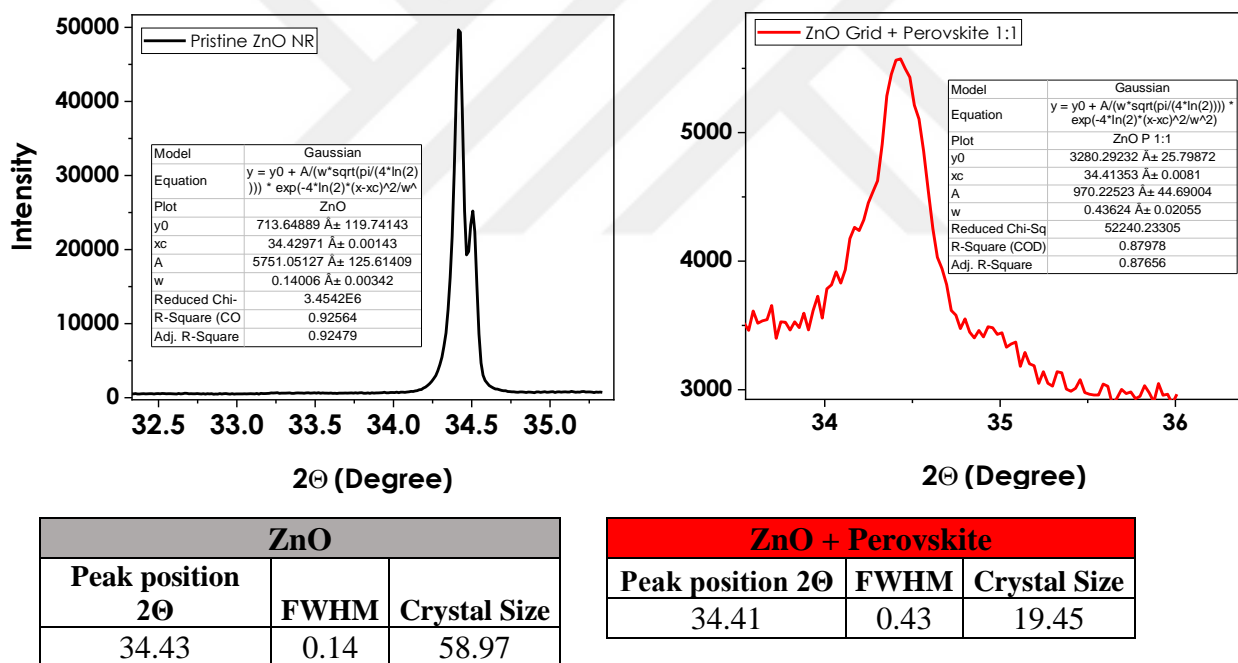


Figure 4.6: Utilization of XRD data for the calculation of pristine and perovskite deposited ZnO's crystal sizes.

By contrasting the characteristic perovskite emissions at 570 nm, the carrier lifetimes of 1:1 and 1:5 perovskite deposited ZnO thin films have also been evaluated (Figure 4.5 (f)). The aforementioned IHP-related carrier lifetimes have been observed to be essentially identical with primary decay components corresponding to 2.4 and 2.03ns for composite and pure rhombohedral IHPs, respectively. However, for both samples,

defect-driven recombinations generate a much slower decay component reaching lifetimes of 13.22ns for CsPbBr₃-Cs₄PbBr₆ and 10.21ns for pure Cs₄PbBr₆, consecutively. This tiny but substantial variation in the lifetime values of perovskite deposited ZnO films is assumed to be caused by the inhibition of ZnO-originated emissions due to the presence of a denser and more luminescent Cs₄PbBr₆ layer. This suppression of ZnO-inflicted emission is clearly emphasized in the inset of Figure 4.5 (d).

At the end of our IHP-deposited, multi-morphologically patterned ZnO investigation, an additional experiment based on the patterning of a more complicated structure (university name and logo) has been performed. After selectively scribing the upper Ti-layer in the predetermined patterns as given in Figure 4.7, their deposition with pure Cs₄PbBr₆ layer (1:5 PbBr₂:CsBr) has been accomplished. SEM images demonstrate the abbreviated name of the university (TOBB ETU) scribed on ITO/ZnO/Ti coated glass substrate, where the selective scribing of the top Ti layer followed by CBD resulted in the formation of NRs throughout the engraved lettering (Figure 4.7 (a)). The design of the university logo was likewise scribed and sequentially deposited with NR and 1:5 ratio IHP layers, in a similar manner. The green fluorescence created as a result of blue excitation is given as the FM image in Figure 4.7 (b). The luminosities arising from inside and outside of the pattern highlight the difference between highly perovskite accumulated and non-accumulated areas. Figures 4.7 (c) and (d) show the OM images of the same sample captured under yellow and red filters, respectively.

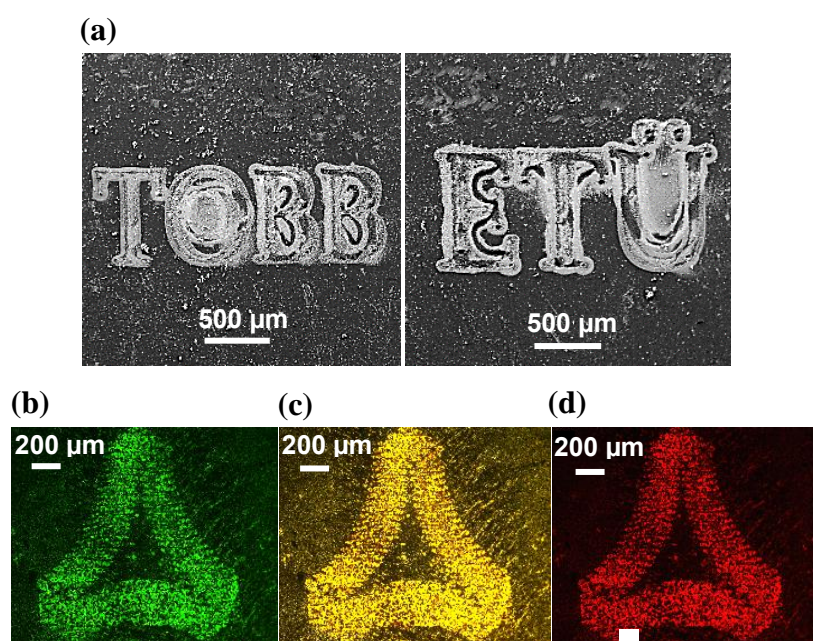


Figure 4.7: (a) SEM image of laser patterned and CBD grown samples containing the abbreviated name of the university. (b) Fluorescence emission image captured from patterned, CBD grown and perovskite-layer deposited sample containing the university logo. OM image of the same sample obtained under (c) yellow and (d) red filters.

4.4 Conclusions

In conclusion, the simultaneous growth of two different ZnO nanostructures grown under the same chemical bath environment has been achieved via the smart, laser-based modification of ITO/ZnO/Ti glass substrates. The resulting composite NR/NFI film formation contributed to the enhanced optical performance of the developed device generating an emission covering the whole visible region. Through the incorporation of the highly luminescent 0D Cs₄PbBr₆ perovskite materials into the structure, both the charge carrier lifetimes and luminescence intensities have been improved. Moreover, completely pure orthorhombic Cs₄PbBr₆ formation has been achieved, showing supreme material properties. In regard to the obtained outcomes, the perovskite layer deposition on the laser patterned multi-morphological ZnO enabled us to control the fluorescence properties, indicating that our novel patterning method possesses a highly promising potential for being implemented into light-emitting, optoelectronic devices in the upcoming studies.

REFERENCES

- [1] **Feynman, R.P.** There's a Plenty of Room At the bottom. (1960). *Engineering and Science*, 23 , 22–36
- [2] **Kannan, N. and Vakeesan, D.** (2016) Solar energy for future world: - A review. *Renew. Sustain. Energy Rev.* 62, 1092–1105
- [3] **Segev, G. et al.** (2018) Hybrid photoelectrochemical and photovoltaic cells for simultaneous production of chemical fuels and electrical power. *Nat. Mater.* 17, 1115–1121
- [4] **Andreani, L.C. et al.** (2019) Silicon solar cells: Toward the efficiency limits. *Adv. Phys. X* 4, 126-148
- [5] **Fujishima, A. and Honda, K.** (1972) Biological sciences: One and two-dimensional structure of alpha-helix and beta-sheet forms of poly(L-Alanine) shown by specific heat measurements at low temperatures (1.5-20 K). *Nature* 238, 37–38
- [6] **Desai, M.A. et al.** (2019) Zinc oxide superstructures: Recent synthesis approaches and application for hydrogen production via photoelectrochemical water splitting. *Int. J. Hydrogen Energy* 44, 2091–2127
- [7] **Choi, H.J. et al.** (2016) Hierarchical ZnO Nanowires-loaded Sb-doped SnO₂-ZnO Micrograting Pattern via Direct Imprinting-assisted Hydrothermal Growth and Its Selective Detection of Acetone Molecules. *Sci. Rep.* 6, 1–10
- [8] **Sahatiya, P. et al.** (2017) Flexible substrate based 2D ZnO (n)/graphene (p) rectifying junction as enhanced broadband photodetector using strain modulation. *2D Mater.* 4, 025053
- [9] **Li, J. et al.** (2019) Enhanced piezoelectric output of the PVDF-TrFE/ZnO flexible piezoelectric nanogenerator by surface modification. *Appl. Surf. Sci.* 463, 626–634

- [10] **Tong, F. et al.** (2012) Flexible organic/inorganic hybrid solar cells based on conjugated polymer and ZnO nanorod array. *Semicond. Sci. Technol.* 27,
- [11] **Rodnyi, P.A. and Khodyuk, I. V** (2011) Optical and Luminescence Properties of Zinc Oxide (Review). 111, 776–785
- [12] **Rahman, M.A.** (2014) A Review on Semiconductors Including Applications and Temperature Effects in Semiconductors. *Am. Sci. Res. J. Eng. Technol. Sci. ISSN 7*, 50–70
- [13] **Desai, M.A. and Sartale, S.D.** (2015) Facile soft solution route to engineer hierarchical morphologies of ZnO nanostructures. *Cryst. Growth Des.* 15, 4813–4820
- [14] **Yolaçan, D. and Demirci Sankir, N.** (2017) Enhanced photoelectrochemical and photocatalytic properties of 3D-hierarchical ZnO nanostructures. *J. Alloys Compd.* 726, 474–483
- [15] **Liu, L. et al.** (2016) Oxygen vacancies: The origin of n-type conductivity in ZnO. *Phys. Rev. B* 93, 1–6
- [16] **Jiang, P. et al.** (2007) Hierarchical shelled ZnO structures made of bunched nanowire arrays. *Adv. Funct. Mater.* 17, 1303–1310
- [17] **Cai, A. et al.** (2013) Fast synthesis of DNA-assisted flower-like ZnO superstructures with improved photocatalytic and antibacterial performances. *Mater. Lett.* 111, 158–160
- [18] **Ahmed, F. et al.** (2014) Morphological evolution of ZnO nanostructures and their aspect ratio-induced enhancement in photocatalytic properties. *RSC Adv.* 4, 29249–29263
- [19] **Poornajar, M. et al.** (2016) Synthesis of ZnO nanorods via chemical bath deposition method: The effects of physicochemical factors. *Ceram. Int.* 42, 173–184
- [20] **Tseng, Y.K. et al.** (2012) Synthesis of 1D, 2D, and 3D ZnO polycrystalline nanostructures using the sol-gel method. *J. Nanotechnol.* 2012,

- [21] **Fan, J. et al.** (2016) Hydrothermal growth of ZnO nanoflowers and their photocatalyst application. *Bull. Mater. Sci.* 39, 19–26
- [22] **Barreto, G. et al.** (2015) Microwave Assisted Synthesis of ZnO Tridimensional Nanostructures. *Procedia Mater. Sci.* 8, 535–540
- [23] **Koodziejczak-Radzimska, A. et al.** (2012) Structural characterisation of ZnO particles obtained by the emulsion precipitation method. *J. Nanomater.* 2012,
- [24] **Bakranov, N. et al.** (2017) The study of photoelectrochemical water splitting by ZnO nanostructures and ZnO/Ag nanocomposites. *Proc. 2017 IEEE 7th Int. Conf. Nanomater. Appl. Prop. N. 2017* 2017-Janua, 1–4
- [25] **Li, Z. et al.** (2013) Photoelectrochemical cells for solar hydrogen production: Current state of promising photoelectrodes, methods to improve their properties, and outlook. *Energy Environ. Sci.* 6, 347–370
- [26] **Weber, M.F. and Dignam, M.J.** (1986) Splitting water with semiconducting photoelectrodes-Efficiency considerations. *Int. J. Hydrogen Energy* 11, 225–232
- [27] **Liu, Z. et al.** (2017) Photoelectrochemical properties and growth mechanism of varied ZnO nanostructures. *New J. Chem.* 41, 7947–7952
- [28] **Al-Gaashani, R. et al.** (2013) XPS and optical studies of different morphologies of ZnO nanostructures prepared by microwave methods. *Ceram. Int.* 39, 2283–2292
- [29] **Prakash, A. and Bahadur, D.** (2014) Chemically derived defects in zinc oxide nanocrystals and their enhanced photo-electrocatalytic activities. *Phys. Chem. Chem. Phys.* 16, 21429–21437
- [30] **Hezam, A. et al.** (2018) The correlation among morphology, oxygen vacancies and properties of ZnO nanoflowers. *J. Mater. Sci. Mater. Electron.* 29, 13551–13560
- [31] **Kaftelen, H. et al.** (2012) EPR and photoluminescence spectroscopy studies on the defect structure of ZnO nanocrystals. *Phys. Rev. B - Condens. Matter Mater. Phys.* 86, 1–9

- [32] **Repp, S. et al.** (2016) Defect evolution of nonstoichiometric ZnO Quantum Dots. *J. Phys. Chem. C* 120, 25124–25130
- [33] **Gan, J. et al.** (2013) Oxygen vacancies promoting photoelectrochemical performance of ZnO nanocubes. *Sci. Rep.* 3,
- [34] **Boonchun, A. and Lambrecht, W.R.L.** (2013) Electronic structure of defects and doping in ZnO: Oxygen vacancy and nitrogen doping. *Phys. Rev. B* 87, 2091–2101
- [35] **Tu, Y. et al.** (2018) Control of oxygen vacancies in ZnO nanorods by annealing and their influence on ZnO/PEDOT:PSS diode behaviour. *J. Mater. Chem. C* 6, 1815–1821
- [36] **Erdem, E.** (2014) Microwave power, temperature, atmospheric and light dependence of intrinsic defects in ZnO nanoparticles: A study of electron paramagnetic resonance (EPR) spectroscopy. *J. Alloys Compd.* 605, 34–44
- [37] **Baek, M. et al.** (2017) Simple but effective way to enhance photoelectrochemical solar-water-splitting performance of ZnO nanorod arrays: Charge-trapping Zn(OH)₂ annihilation and oxygen vacancy generation by vacuum annealing. *ACS Appl. Mater. Interfaces* 9, 2317–2325
- [38] **Tam, K.H. et al.** (2006) Defects in ZnO nanorods prepared by a hydrothermal method. *J. Phys. Chem. B* 110, 20865–20871
- [39] **Djurišić, A.B. and Leung, Y.H.** (2006) Optical properties of ZnO nanostructures. *Small* 2, 944–961
- [40] **Vanheusden, K. et al.** (1995) Correlation between photoluminescence and oxygen vacancies in ZnO phosphors. *Appl. Phys. Lett.* 403, 403
- [41] **Wu, X.L. et al.** (2001) Photoluminescence and cathodoluminescence studies of stoichiometric and oxygen-deficient ZnO films. *Appl. Phys. Lett.* 78, 2285–2287
- [42] **Van Dijken, A. et al.** (2001) The influence of particle size on the luminescence quantum efficiency of nanocrystalline ZnO particles. *J. Lumin.* 92, 323–328

- [43] **Zuo, Y. et al.** (2009) Morphology, optical and magnetic properties of Zn_{1-x}Ni_xO nanorod arrays fabricated by hydrothermal method. *J. Alloys Compd.* 470, 47–50
- [44] **Chen, S.J. et al.** (2006) Photoluminescence and Raman behaviors of ZnO nanostructures with different morphologies. *J. Cryst. Growth* 289, 55–58
- [45] **Gurylev, V. et al.** (2017) Hydrogenated ZnO nanorods with defect-induced visible light-responsive photoelectrochemical performance. *Appl. Surf. Sci.* 411, 279–284
- [46] **Li, L.M. et al.** (2010) Enhanced sensing properties of defect-controlled ZnO nanotetrapods arising from aluminum doping. *Sensors Actuators, B Chem.* 147, 165–169
- [47] **Allagui, A. et al.** (2016) Mott-Schottky analysis of flower-like ZnO microstructures with constant phase element behavior. *Phys. Status Solidi Appl. Mater. Sci.* 213, 139–145
- [48] **Gelderman, K. et al.** (2007) Flat-band potential of a semiconductor: Using the Mott-Schottky equation. *J. Chem. Educ.* 84, 685–688
- [49] **Jin, C. et al.** (2011) Subwavelength Optical Resonant Cavity-Induced Enhancement of the Near-Band-Edge Emission from ZnO-Core / SnO₂-Shell Nanorods. *J. Phys. Chem. C* 115, 8513–8518
- [50] **Fan, J.C. et al.** (2013) InTech-Zno_based_light_emitting_diodes.pdf.
- [51] **Shionaya, S.** Luminescence of Solids. 1st Editio. (Vij, D. R., ed), Plenum Press
- [52] **Zhang, Z. and Xiong, H.** (2015) Photoluminescent ZnO Nanoparticles and Their Biological Applications. DOI: 10.3390/ma8063101
- [53] **Willander, M. et al.** (2010) Luminescence from Zinc Oxide Nanostructures and Polymers and their Hybrid Devices. DOI: 10.3390/ma3042643
- [54] **Ahn, C.H. et al.** (2009) A comparative analysis of deep level emission in ZnO layers deposited by various methods. 105, 01350, 1–6

- [55] **Fang, Z. et al.** (2004) Blue luminescent center in ZnO films deposited on silicon substrates. 26, 239–242
- [56] **Zhao, Q.X. et al.** (2005) Deep-level emissions influenced by O and Zn implantations in ZnO. 211912,
- [57] **Børseth, T.M. et al.** (2006) Identification of oxygen and zinc vacancy optical signals in ZnO Identification of oxygen and zinc vacancy optical signals in ZnO. DOI: 10.1063/1.2424641
- [58] **Klason, P. et al.** (2008) Temperature dependence and decay times of zinc and oxygen vacancy related photoluminescence bands in zinc oxide. 145, 321–326
- [59] **You, A. et al.** (2005) Photoluminescence and cathodoluminescence studies of stoichiometric and oxygen-deficient ZnO films. 2285, 1–4
- [60] **Gomi, M. et al.** (2003) Photoluminescent and structural properties of precipitated ZnO fine particles. *Japanese J. Appl. Physics, Part 1 Regul. Pap. Short Notes Rev. Pap.* 42, 481–485
- [61] **Duan, X. et al.** (2010) Large-area nanoscale patterning of functional materials by nanomolding in capillaries. *Adv. Funct. Mater.* 20, 2519–2526
- [62] **Cavallini, M. et al.** (2008) Micro- and nanopatterning of spin-transition compounds into logical structures. *Angew. Chemie - Int. Ed.* 47, 8596–8600
- [63] **Shankar, S.S. et al.** (2009) Micro/nanoscale patterning of nanostructured metal substrates for plasmonic applications. *ACS Nano* 3, 893–900
- [64] **Menard, E. et al.** (2007) Micro- and nanopatterning techniques for organic electronic and optoelectronic systems. *Chem. Rev.* 107, 1117–1160
- [65] **Pimpin, A. and Srituravanich, W.** (2012) Reviews on micro- and nanolithography techniques and their applications. *Eng. J.* 16, 37–55
- [66] **Zoberbier, R. and Souter, M.** (2012) Laser Ablation – Emerging Patterning Technology for Advanced Packaging Laser Ablation – Emerging Patterning. *SUSS MicroTec*
- [67] **Esakkimuthu, M. et al.** (2017) Laser patterning of thin film copper and ITO

on flexible substrates for terahertz antenna applications. *J. Laser Micro Nanoeng.* 12, 313–320

- [68] **Esakkimuthu, M. et al.** (2019) Microfabrication of Low Cost Frequency Selective Surface for Terahertz Wave by Laser Ablation. *J. Electron. Mater.* 48, 2423–2429
- [69] **Feng, W. et al.** (2019) Patterning of aluminum metallized pet film using high repetition rate fiber laser. *J. Laser Appl.* 31, 022208
- [70] **Shahbazi, A.H. et al.** (2018) Theoretical and experimental investigation of continuous-wave laser scribing on metal thin film: effect of power. *Appl. Opt.* 57, 9988
- [71] **Sood, A.K. et al.** (2011) ZnO Nanostructures for Optoelectronic Applications. DOI: 10.5772/16202
- [72] **Ng, A.M.C. et al.** (2010) ZnO nanostructures for optoelectronics : Material properties and device applications. 34, 191–259
- [73] **Abdullayeva, N. et al.** (2019) Investigation of Strain Effects on Photoelectrochemical Performance of Flexible ZnO Electrodes. *Sci. Rep.* 9, 1–14
- [74] **Liu, Z. et al.** (2010) Effects of substrates and seed layers on solution growing ZnO nanorods. *J. Solid State Electrochem.* 14, 957–963
- [75] **Tanaka, I. and Mizoguchi, T.** (2009) First-principles calculations of x-ray absorption near edge structure and energy loss near edge structure: Present and future. *J. Phys. Condens. Matter* 21, 1–9
- [76] **Liu, H. et al.** (2013) Contributions of magnetic properties in epitaxial copper-doped ZnO. *Phys. Chem. Chem. Phys.* 15, 13153–13161
- [77] **Xin, J. et al.** (2016) X-ray absorption fine structure of ZnO thin film on Si and sapphire grown by MOCVD. *2016 5th Int. Symp. Next-Generation Electron. ISNE 2016* DOI: 10.1109/ISNE.2016.7543313
- [78] **Jeong, E.S. et al.** (2008) Local structural properties of ZnO nanoparticles,

- nanorods and powder studied by extended X-ray absorption fine structure. *J. Korean Phys. Soc.* 53, 461–465
- [79] **Decremps, F. et al.** (2003) Local structure of condensed zinc oxide. *Phys. Rev. B - Condens. Matter Mater. Phys.* 68, 1–10
- [80] **Coulter, J.B. and Birnie, D.P.** (2018) Assessing Tauc Plot Slope Quantification: ZnO Thin Films as a Model System. *Phys. Status Solidi Basic Res.* 255, 1–7
- [81] **Yan, D. et al.** (2017) Near band edge photoluminescence of ZnO nanowires: Optimization via surface engineering. *Appl. Phys. Lett.* 111, 1–4
- [82] **Wang, T. et al.** (2014) Diameter-dependent luminescence properties of ZnO wires by mapping. *J. Phys. D. Appl. Phys.* 47,
- [83] **Ly, Y. et al.** (2017) Growth mechanism and photoluminescence property of hydrothermal oriented ZnO nanostructures evolving from nanorods to nanoplates. *J. Alloys Compd.* 718, 161–169
- [84] **Hassan, A. et al.** (2019) Large photoluminescence enhancement in mechanical-exfoliated one-dimensional ZnO nanorods. *J. Mater. Sci. Mater. Electron.* 30, 5170–5176
- [85] **Ghose, S. et al.** (2015) Role of Zn-interstitial defect states on d0 ferromagnetism of mechanically milled ZnO nanoparticles. *RSC Adv.* 5, 99766–99774
- [86] **Neshchimenko, V. et al.** (2018) Optical radiation stability of ZnO hollow particles. *Nanoscale* 10, 22335–22347
- [87] **Göpel, W. and Lampe, U.** (1980) Influence of defects on the electronic structure of zinc oxide surfaces. *Phys. Rev. B* 22, 6447–6462
- [88] **Greene, L. et al.** (2003) Low-Temperature Wafer-Scale Production of ZnO Nanowire Arrays. *Angew. Chemie* 115, 3139–3142
- [89] **Li, D. et al.** (2004) Different origins of visible luminescence in ZnO nanostructures fabricated by the chemical and evaporation methods. *Appl.*

Phys. Lett. 85, 1601–1603

- [90] **Wang, M. et al.** (2012) Near-infrared photoluminescence from ZnO. *Appl. Phys. Lett.* 100, 1–4
- [91] **Liu, R. et al.** (2020) Efficient electronic coupling and heterogeneous charge transport of zero-dimensional Cs₄PbBr₆ perovskite emitters. *J. Mater. Chem. A* 8, 23803–23811
- [92] **Yoshikawa, H. and Adachi, S.** (1997) Optical Constants of ZnO. *Jpn. J. Appl. Phys.* 36, 6237–6243
- [93] **Özdoğan, M. et al.** (2019) The comparison of transient photocurrent spectroscopy measurements of Pulsed Electron Deposited ZnO thin film for air and vacuum ambient conditions. *Thin Solid Films* 680, 48–54
- [94] **Sarkar, S. and Basak, D.** (2015) Understanding of ultraviolet photoresponse properties of ZnO nanorods : Effect of nanorod ' s size and ambient. *J. Nanosci. Lett.* 5, 1–4
- [95] **McDonnell, C. et al.** (2016) Part 1: Wavelength dependent nanosecond laser patterning of very thin indium tin oxide films on glass substrates. *Opt. Lasers Eng.* 80, 73–82
- [96] **Torrìsi, L. et al.** (2003) Comparison of nanosecond laser ablation at 1064 and 308 nm wavelength. *Appl. Surf. Sci.* 210, 262–273
- [97] **Hamad, A.H. et al.** (2016) Laser Ablation in Different Environments and Generation of Nanoparticles. In *Applications of Laser Ablation - Thin Film Deposition, Nanomaterial Synthesis and Surface Modification* pp. 177–196, IntechOpen
- [98] **McDonnell, C. et al.** (2016) Part 2: Ultra-short pulse laser patterning of very thin indium tin oxide on glass substrates. *Opt. Lasers Eng.* 81, 70–78
- [99] **Protesescu, L. et al.** (2015) Nanocrystals of Cesium Lead Halide Perovskites (CsPbX₃, X = Cl, Br, and I): Novel Optoelectronic Materials Showing Bright Emission with Wide Color Gamut. DOI: 10.1021/nl5048779

- [100] **Song, J. et al.** (2015) Quantum Dot Light-Emitting Diodes Based on Inorganic Perovskite Cesium Lead Halides (CsPbX₃). DOI: 10.1002/adma.201502567
- [101] **Song, J. et al.** (2018) Organic – Inorganic Hybrid Passivation Enables Perovskite QLEDs with an EQE of 16 . 48 %. 1805409, 1–9
- [102] **Quan, L.N. et al.** (2017) Highly Emissive Green Perovskite Nanocrystals in a Solid State Crystalline Matrix. DOI: 10.1002/adma.201605945
- [103] **Akkerman, Q.A. et al.** (2017) Nearly Monodisperse Insulator Cs₄PbX₆ (X = Cl, Br, I) Nanocrystals, Their Mixed Halide Compositions, and Their Transformation into CsPbX₃ Nanocrystals. 6, 1–7
- [104] **Xu, J. et al.** (2017) Imbedded Nanocrystals of CsPbBr₃ in Cs₄PbBr₆ : Kinetics , Enhanced Oscillator Strength , and Application in Light-Emitting Diodes. 1703703, 1–10
- [105] **Andrews, R.H. et al.** (1983) Solid-state Properties of Materials of the Type Cs₄MX_s (where M = Sn or Pb and X = Cl or Br). *J. Chem. Soc. Dalt. Trans.*
- [106] **Nikl, M. et al.** (1999) Photoluminescence of Cs₄PbBr₆ crystals and thin films. 306, 280–284
- [107] **Velazquez, M. et al.** (2008) Growth and characterization of pure and Pr³⁺ - doped Cs₄PbBr₆ crystals. 310, 5458–5463
- [108] **Garcia, V.J. et al.** (2018) Low temperature-processed ZnO nanorods-TiO₂ nanoparticles composite as electron transporting layer for perovskite solar cells. *Thin Solid Films* 662, 70–75
- [109] **Wang, H. et al.** (2019) Enhance the performance of ZnO-based perovskite solar cells under ambient conditions. *Opt. Mater. (Amst)*. 89, 375–381
- [110] **Bu, I.Y.Y.** (2019) Interconnected ZnO branches as an effective electron transfer layer in perovskite solar cells. *Optik (Stuttg)*. 182, 32–36
- [111] **Li, W. et al.** (2018) Inorganic perovskite light emitting diodes with ZnO as the electron transport layer by direct atomic layer deposition. *Org. Electron*. 57,

- [112] **Shan, Q. et al.** (2017) All-inorganic quantum-dot light-emitting diodes based on perovskite emitters with low turn-on voltage and high humidity stability. *J. Mater. Chem. C* 5, 4565–4570
- [113] **Zhang, L. et al.** (2017) Ultra-bright and highly efficient inorganic based perovskite light-emitting diodes. *Nat. Commun.* 8, 1–8
- [114] **Liu, H. et al.** (2017) A high-performance photodetector based on an inorganic perovskite-ZnO heterostructure. *J. Mater. Chem. C* 5, 6115–6122
- [115] **Yang, D. et al.** (2019) All-inorganic cesium lead halide perovskite nanocrystals: Synthesis, surface engineering and applications. *J. Mater. Chem. C* 7, 757–789
- [116] **Deng, J. et al.** (2019) All-inorganic lead halide perovskites: A promising choice for photovoltaics and detectors. *J. Mater. Chem. C* 7, 12415–12440
- [117] **Song, J. et al.** (2017) Ultralarge All-Inorganic Perovskite Bulk Single Crystal for High-Performance Visible–Infrared Dual-Modal Photodetectors. *Adv. Opt. Mater.* 5, 1–8
- [118] **Yang, Z. et al.** (2018) Engineering the Exciton Dissociation in Quantum-Confining 2D CsPbBr₃ Nanosheet Films. *Adv. Funct. Mater.* 28, 1–10
- [119] **Li, X. et al.** (2016) CsPbX₃ Quantum Dots for Lighting and Displays: Room-temperature Synthesis, Photoluminescence Superiorities, Underlying Origins and White Light-Emitting Diodes. *Adv. Funct. Mater.* 26, 2435–2445
- [120] **Song, Z. et al.** (2019) Luminescent perovskites: Recent advances in theory and experiments. *Inorg. Chem. Front.* 6, 2969–3011
- [121] **Zhang, H. et al.** (2017) Pure zero-dimensional Cs₄PbBr₆ single crystal rhombohedral microdisks with high luminescence and stability. *Phys. Chem. Chem. Phys.* 19, 29092–29098
- [122] **Manser, J.S. et al.** (2016) Intriguing Optoelectronic Properties of Metal Halide Perovskites. *Chem. Rev.* 116, 12956–13008

- [123] **Han, D. et al.** (2018) Unraveling luminescence mechanisms in zero-dimensional halide perovskites. *J. Mater. Chem. C* 6, 6398–6405
- [124] **Wang, L. et al.** (2020) Photoluminescence Origin of Zero-Dimensional Cs₄PbBr₆ Perovskite. *ACS Energy Lett.* 5, 87–99
- [125] **Liu, R.T. et al.** (2019) Disentangling the Luminescent Mechanism of Cs₄PbBr₆ Single Crystals from an Ultrafast Dynamics Perspective. *J. Phys. Chem. Lett.* 10, 6572–6577
- [126] **Xu, L. et al.** (2019) Synthesis of stable and phase-adjustable CsPbBr₃@Cs₄PbBr₆ nanocrystals: Via novel anion-cation reactions. *Nanoscale Adv.* 1, 980–988
- [127] **Weerd, C. De et al.** (2017) Hybridization of Single Nanocrystals of Cs₄PbBr₆ and CsPbBr₃. *J. Phys. Chem. C* 121, 19490–19496
- [128] **Wu, L. et al.** (2017) From Nonluminescent Cs₄PbX₆ (X = Cl, Br, I) Nanocrystals to Highly Luminescent CsPbX₃ Nanocrystals: Water-Triggered Transformation through a CsX-Stripping Mechanism. *Nano Lett.* 17, 5799–5804
- [129] **Chen, Y.M. et al.** (2018) Cs₄PbBr₆ /CsPbBr₃ Perovskite Composites with Near-Unity Luminescence Quantum Yield: Large-Scale Synthesis, Luminescence and Formation Mechanism, and White Light-Emitting Diode Application. *ACS Appl. Mater. Interfaces* 10, 15905–15912
- [130] **Chen, X. et al.** (2018) Centimeter-Sized Cs₄PbBr₆ Crystals with Embedded CsPbBr₃ Nanocrystals Showing Superior Photoluminescence: Nonstoichiometry Induced Transformation and Light-Emitting Applications. *Adv. Funct. Mater.* 28, 1–7
- [131] **Zhang, H. et al.** (2019) P-GaN/n-ZnO Nanorod/CsPbBr₃ Quantum Dots Decorated with ZnO Nanoseeds for Light-Emitting Diodes. *ACS Appl. Nano Mater.* 2, 7661–7668
- [132] **Qin, Z. et al.** (2019) Revealing the Origin of Luminescence Center in 0D Cs₄PbBr₆ Perovskite. *Chem. Mater.* DOI: 10.1021/acs.chemmater.9b03426

- [133] **Yang, L. *et al.*** (2017) Room-temperature synthesis of pure perovskite-related Cs₄PbBr₆ nanocrystals and their ligand-mediated evolution into highly luminescent CsPbBr₃ nanosheets. *J. Nanoparticle Res.* 19,
- [134] **Li, C. *et al.*** (2017) Enhanced random lasing emission from highly compact CsPbBr₃ perovskite thin films decorated by ZnO nanoparticles. *Nano Energy* 40, 195–202



